UCLA
Computational and Applied Mathematics

Mathematics an physics based models of metal and composite materials' properties and fracture and their applications

Koffi Enakoutsa

Department of Mathematics
University of California, Los Angeles
Los Angeles, CA, 90095-1555

Contents

List of Figures

Chapter 1

Introduction

My reasearch works focus on the development of mathematics and physics based models for the computer simulations of defects and crack propagation in materials, flexo-electricity phenomena at nano-scale, and the coupled thermo-mechanical behaviors of composite and metallic materials. I emphasize the development of experimentally validated state-of-the art analytic tools and computational methods based on generalized continuum mechanics and multidisciplinary approaches to predict the behaviors of materials in normal and extreme environments. I am interested in the constitutive modeling of failure in metals, flexo-electricity phenomena in nanomaterials, the effects of dislocations and disclinations defects in polycrystals, and the phase transformations in metals. This report is a synthesis of my recent current and future research activities. The report is subdivided as follows.

1.1 Scope of the report

- Next, **Chapter 2** presents the most successful results among my research activities, which I got alone or in collaboration with Jean-Baptiste Leblond and Douglas J. Bammann and his Ph.D. student Ahad Fazle concerning the solution of the problem of infinite localization of deformation and damage in ductile materials. More precisely, with the aforementioned collaborators, I critically examined two non-local models for ductile failure in metals. The first is a non-local variant of the Gurson model, which consists in delocalizing the damage evolution equation in the Gurson's model and the second is a 'micromorphic' type model. The study of these two models allowed establishing the independence of their numerical predictions vis--vis of the mesh size discretization and their capacities to reproduce the results of typical ductile rupture experiments. Therefore, these two models are viable solutions to the problem of the infinite localization of damage and deformation in porous ductile solids.

  Because of its generic nature, I applied the method of the delocalization of the damage to a dynamic ductile failure model developed by Douglas Bammann at Sandia National Laboratories and which takes into account the coupling of the damage with the effects of dislocations. Here also, the damage delocalization method made it possible to get independent results regarding the mesh and to reproduce typical experiments of dynamic ductile failure

of metals, which was not possible with the standard models. The chapter also includes my future works in this area of research. They concern the extensions of the results got on generalized continuum modeling of failure to include inertial effects based homogenization methods with dynamic effects. I plan to develop numerical schemes for the computer implementation of the new formulation to enable its coupling with an existing meshfree software to simulate of problems involving a high rate fracture, such as fragmentation of metals.

- Next, **Chapter 3** presents a model of flexo-electricity in metals which I developed with Ivan Giorgio at the Sapienza University of Rome. The model is based on a variational formulation inspired by that of Toupin to get the constitutive relations, equilibrium equations and boundary conditions. This model includes three different electro-mechanical forces. I applied this model to solve the problems of the polarization induced by a hydrostatic loading on a thin hollow sphere and a cylindrical tube and got very satisfactory results. The research project plan which immediately follows the description of the key element of the model concerns the extension of the flexo-electricity model to account for nonlinearities that many experimental works have evidenced and develop numerical algorithms for the numerical implementation of the newly developed models into FE codes. I also plan to use atomistic and quantum simulations to determine some model parameters and for a better understanding of flexo-electricity in metallic and non-metallic materials.

- **Chapter 4** concerns my research work on modeling dislocation and disclination at finite strain. In this topic, Along with D. Bammann and A. Adedoyin I developed a model for dislocation and disclination defects in metals using the framework of the theory of large transformations with multiplicative decomposition of the deformation gradient. These two defects lead to complex expressions in the constitutive equations of the model, sometimes including the bi-rotational operator whose implementation in a finite element code is heavy. To overcome this difficulty, we proposed to model the geometrically necessary dislocations by the *curl* of the inelastic part of the velocity gradient and the disclinations by the *curl* of the latter, extending heuristically deWitt's modeling of disclocation and disclination in small strain to finite strain. We performed micromechanical simulations of classical analytic problems based on this formulation to get results in accordance with dislocations theory. I plan to model these two defects using some geometric arguments, the framework of which has already been suggested by Douglas J. Bammann. A proposal describing this modeling strategy and its practical applications is described in the form a research project at the end of the chapter.

- In **Chapter 5**, I present a recent extension of a model for ceramic matrix composite (CMC) materials to account for coupled thermo-mechanical effects. Namely, I have extended a model for the damage and mechanical behaviors previously proposed by Ladeveze for CMCs by including thermo-mechanical coupling effects that is got by assuming that the internal heat comes from the effects of residual deformations. I performed a numerical implementation of the new model in a finite element (FE) code and calibrated its parameters on a typical CMC. This model reproduces well the thermo-mechanical behavior of typical specimens under cyclic or simple loadings.

A plan to extend the model to include fatigue and chemistry behaviors inevitable in high temperature applications of CMC is presented at the end the work summary on CMC materials as a research project.

- In **Chapter 6**, I present and extension a model of plasticity and evolution of microstructures for single-phase steels developed by Bammann to multiple phases by supposing that the interactions between phases are taken into account through interface constraints. This model is described in the context of the thermodynamics of irreversible processes and takes into account the partition of the deformation associated with each of the phases based on a self-consistent model for polycrystalline materials. The predictions of this model are in a good agreement with the experiments. A proposal to improve some features of the model is also presented at the end of the chapter as a research project on this specific topic.

Chapter 2

Nonlocal Modeling in Ductile Failure of Metals

Constitutive models involving softening all predict unlimited strain localization. This generates undesired consequences, such as bifurcations with an infinite number of bifurcated branches and mesh dependence in finite element computations. Gursons [17] model of ductile rupture, which was derived from approximate limit-analysis of some representative cell in a porous plastic material, is no exception. Softening arises in this model from the gradual increase of the porosity, and this induces unlimited localization.

Two proposals of modification of the Gurson model have been made by Leblond et al. (1994) and Gologanu et al. [15] to solve the problem. The aim of my PhD dissertation work was to assess the practical applicability of these proposals. The essential criteria used are mesh independence and satisfactory reproduction of the results of some ductile fracture experiments.

The first, purely heuristic proposal comprised adopting a nonlocal evolution equation for the porosity which involves a convolution integral of the local porosity rate. Numerical experiences show that this does not allow matching experimental load-displacement curves of pre-cracked specimens, because of excessive smoothing of the porosity in the ligament ahead of the crack tip. A theoretical analysis of this phenomenon suggested a simple remedy comprising adopting a nonlocal evolution equation for the logarithm of the porosity instead of the porosity itself. No excessive smoothing of the porosity is then predicted, and experimental load-displacement curves are then satisfactorily reproduced by the model.

The second, more theoretically based proposal was derived from some refinement of Gursons original homogenization procedure. The homogenized model got in this way was complex and involved both the second gradient of the macroscopic velocity and generalized macroscopic stresses of "moment" type. Its numerical implementation is also involved because of the clear need for C^1 elements, which must be obviated through introduction of some new nodal variable representing the strain rate. Application of this second model to simulation of pre-cracked specimens also yields a satisfactory match of experimental and numerical load-displacement curves. The conclusion is that both proposals represent viable solutions to the problem of unlimited strain localization in porous ductile solids undergoing monotonic loading conditions.

The first proposal of modification of Gurson model is generic and can be extended to any local constitutive model involving damage evolution equation. Therefore, I used this proposal in an internal state variable damage model to predict dynamic ductile failure in metals. The aim here also is to circumvent numerical instabilities arising from an ill-posed modeling of the post-bifurcation regime of metals. The characteristic length scale in the non-local damage is of a mathematical nature and is calibrated using a series of notch tensile tests. Then the same length scale from the notch tests is used in solving the more complex problem of a high-velocity (between 89 and 107m/s) rigid projectile colliding against a 6061-T6 aluminum-disk. The utilization of non-local formulation to solve the latter problem is opportune since high-velocity impact problems exhibit softening because of the increase of damage. The results show that incorporating a characteristic length scale into the constitutive model does eliminate the pathological mesh-dependency associated with material instabilities. The numerical calculations mirror well experimental results.

In the research project on ductile fracture in porous metals, I mainly present how I plan to extend the knowledge gained on modeling ductile failure to include inertial effects to simulate problems involving dynamic ductile failure. The mains theoretical foundations of the proposal are the homogenization and limit analysis of a representative volume element for porous metals in a dynamic failure of metals. The proposal also considered other modeling framework that are rather phenomenological based.

2.1 Nonlocal Gurson Model

2.1.1 Introduction

A common feature of all constitutive models involving softening is the prediction of unlimited strain localization. This phenomenon has several consequences undesired from both the physical and mathematical points of view. Such consequences include bifurcations with an infinite number of bifurcated branches, absence of energy dissipation during crack propagation, and dependence of finite element results upon mesh size. These phenomena are clear symptoms of the same basic shortcoming of such models: their use is limited to some minimum scale, but when strain localizes, as they predict it must, they are in fact abusively applied at finer and finer scales. The prediction of localization is contradictory with the macroscopic character of the models.

Gurson's [57] famous model of ductile rupture, which was derived from approximate homogenization of some representative elementary cell in a plastic porous material, is no exception. In this model, unlimited localization arises from the softening because of the gradual increase of the porosity. Localization implies applying the model to elementary volumes too small to contain at least one void, for which it becomes meaningless.

We assessed the practical applicability of a proposal made by Leblond it et al. [58] to solve these problems. This heuristic proposal was inspired from a similar one made by Pijaudier-Cabot and Bazant [59] in damage of concrete. It comprised adopting a *nonlocal evolution equation for the porosity* (softening parameter) within an otherwise unmodified Gurson model. Nonlocality was introduced in the form of a convolution integral of some "local porosity rate". This proposal has been adopted by several authors, notably Tvergaard and Needleman (see [60] and subsequent works). Although Leblond *et al.*'s [58] nonlocal evolution equation for the porosity eliminates mesh size effects, it unfortunately also results in considerable degradation of the agreement between the experimental load-displacement curve and that got numerically using Gurson's original model. Detailed inspection of the numerical results shows that this is because of excessive smoothing of the porosity in the ligament ahead of the crack tip.

A theoretical analysis of this phenomenon is presented. Although this analysis is based on crude simplifying hypotheses such as unboundedness of the body and homogeneity of the mechanical fields, it suffices to explain the failure of the nonlocal model considered and to suggest a very simple remedy suggested based on the previous analysis. This remedy comprises adopting a nonlocal evolution equation for the *logarithm* of the porosity instead of the porosity itself. The mathematical character of the equation then changes and no excessive smoothing is to be expected. This is confirmed by repeating the same numerical simulation as before but with the new evolution equation for the porosity. The new simulation now reveals satisfactory agreement of numerical and experimental results.

2.1.2 Nonlocal Gurson Model I

There are four main elements in Gurson's model. The first one is a "homogenized" yield criterion for porous plastic media which reads

$$\Phi(\boldsymbol{\sigma}, f) \equiv \frac{\sigma_{eq}^2}{\bar{\sigma}^2} + 2p \cosh\left(\frac{3}{2}\frac{\sigma_m}{\bar{\sigma}}\right) - 1 - p^2 = 0. \tag{2.1}$$

In this expression,

- $\sigma_{eq} \equiv \left(\frac{3}{2}\sigma'_{ij}\sigma'_{ij}\right)^{1/2}$ ($\boldsymbol{\sigma}' \equiv$ deviator of $\boldsymbol{\sigma}$) is the von Mises equivalent stress;
- $\sigma_m \equiv \frac{1}{3}$ tr $\boldsymbol{\sigma}$ is the mean stress;
- $\bar{\sigma}$ represents a kind of average value of the yield stress in the heterogeneous metallic matrix, the evolution equation of which is given below;
- p is a parameter connected to the porosity (void volume fraction) f through the relation (Tvergaard [61], Tvergaard and Needleman [62]):

$$p \equiv qf^* \quad , \quad f^* \equiv \begin{cases} f & \text{if} \quad f \leq f_c \\ f_c + \delta(f - f_c) & \text{if} \quad f > f_c \end{cases} \tag{2.2}$$

  where q is "Tvergaard's parameter", f_c the "critical" porosity at the onset of coalescence of voids, and δ (> 1) a factor describing the accelerated degradation of the material during coalescence.

The second element of Gurson's model is a plastic flow rule associated to the yield criterion (2.33) through normality[1]:

$$\mathbf{D}^p = \eta \frac{\partial \Phi}{\partial \boldsymbol{\sigma}}(\boldsymbol{\sigma}, f) \quad , \quad \eta \begin{cases} = 0 & \text{if} \quad \Phi(\boldsymbol{\sigma}, f) < 0 \\ \geq 0 & \text{if} \quad \Phi(\boldsymbol{\sigma}, f) = 0 \end{cases} \tag{2.3}$$

where $\mathbf{D}^p$ is the (Eulerian) plastic strain rate.

The third element is an evolution equation for the porosity which derives from approximate incompressibility of the metallic matrix and reads

$$\dot{f} = (1 - f) \text{ tr } \mathbf{D}^p. \tag{2.4}$$

The fourth element is an evolution equation for the parameter $\bar{\sigma}$. This parameter is given by

$$\bar{\sigma} \equiv \sigma(\bar{\epsilon}) \tag{2.5}$$

[1] It has been shown by Gurson [57] that the normality property is preserved in the homogenization process.

where $\sigma(\epsilon)$ is the function providing the yield stress of the matrix material as a function of the equivalent cumulated plastic strain ϵ, and $\bar{\epsilon}$ is the average value of this equivalent strain in the heterogeneous matrix. The evolution of $\bar{\epsilon}$ is governed by the following equation:

$$(1-f)\bar{\sigma}\dot{\bar{\epsilon}} = \boldsymbol{\sigma} : \mathbf{D}^p. \tag{2.6}$$

Leblond *et al.*'s [58] proposal consists of replacing the evolution equation (2.4) of the porosity by

$$\dot{f}(\mathbf{x}) = \frac{1}{A(\mathbf{x})}\int_\Omega \phi(\mathbf{x}-\mathbf{y})\dot{f}^{loc}(\mathbf{y})\, dV_y \tag{2.7}$$

where Ω denotes the body considered, ϕ is some "smoothing function", and the factor $A(\mathbf{x})$ and the "local porosity rate" $\dot{f}^{loc}$ are given by

$$A(\mathbf{x}) \equiv \int_\Omega \phi(\mathbf{x}-\mathbf{y})\, dV_y \tag{2.8}$$

and

$$\dot{f}^{loc}(\mathbf{x}) \equiv (1-f(\mathbf{x}))\ \mathrm{tr}\ [\mathbf{D}^p(\mathbf{x})]. \tag{2.9}$$

The term $1/A(\mathbf{x})$ is introduced in equation (2.7) in order to avoid spurious boundary effects. Indeed it is obviously necessary that $\dot{f}$ be identical to $\dot{f}^{loc}$ if the latter quantity is spatially uniform. This would not be the case in the vicinity of the external boundary in the absence of the term $1/A(\mathbf{x})$.

The underlying physical idea in equation (2.7) is that the porosity is in essence a nonlocal parameter, since it makes sense only for "elementary volumes" sufficiently large to contain at least one void. However, it must be frankly acknowledged that equation (2.7) is purely heuristic and lacks any serious theoretical justification.

The convolution integral in equation (2.7) can be performed on either the initial configuration or the present one according to whether the vectors $\mathbf{x}$ and $\mathbf{y}$ are interpreted as initial or present positions. The choice of the initial configuration is made in the present work. Also, the smoothing function is taken in the form of a Gaussian:

$$\phi(\mathbf{x}) \equiv \exp(-\|\mathbf{x}\|^2/b^2) \tag{2.10}$$

where b is a "characteristic microstructural length" of the order of the mean void spacing.

2.1.3 Numerical implementation of the model

The key point of the numerical implementation of any plasticity model lies in the necessary operation of "projection" onto the yield locus. The projection problem comprises deriving, at a given Gauss point and for a time-interval $[t, t+\Delta t]$, the values of all unknowns $\boldsymbol{\sigma}$, f, $\bar{\sigma}$, etc., at $t+\Delta t$ from their values at t and that of the increment of total strain. The ingredients to be used are the yield criterion at time $t+\Delta t$ and discretized forms of the flow rule and the evolution equations of internal parameters between instants t and $t+\Delta t$.

It has been shown by Nguyen [63] that provided that the constitutive equations define a "standard generalized material" (Halphen and Nguyen [64]) and the flow rule and the evolution equations of internal parameters are discretized in time with an implicit (backward Euler) scheme, the projection problem is equivalent to minimizing some strictly convex function. Existence and uniqueness of the solution follow from there.

It can be shown that for the Gurson criterion (2.33) considered here, the equations of the projection problem fit into the framework of standard generalized materials *provided that the porosity may not vary*. This is one good reason for discretizing the evolution equation (2.4) or (2.7) of f with an *explicit* scheme; f is then fixed during the whole procedure of solution between instants t and $t+\Delta t$ and updated only at the end, for the next time step. Another argument in favor of an explicit scheme for the porosity is that numerical experience reveals that it allows for easier convergence of the global elastoplastic iterations. Use of an *implicit* scheme for the flow rule (2.37) and the evolution equation (2.41) of the parameter $\bar{\epsilon}$ then warrants, by Nguyen's work [63], existence and uniqueness of the solution of the projection problem.

Replacing the local evolution equation (2.4) by the nonlocal one (2.7) raises none particular problem as long as, again, it is discretized with an explicit scheme. Once the convergence of the global elastoplastic iterations are obtained, the values of the local porosity rate $\dot{f}^{loc}$ are tested at all Gauss points of the structure. A double loop on Gauss points then allows to compute the convolution integrals of equation (2.7).

The projection algorithm uses the following parametrization of the yield criterion (2.33):

$$\left\{ \begin{array}{rcl} \sigma_{eq} & \equiv & (1-p)\,\bar{\sigma}\cos\phi \\ \sigma_m & \equiv & \dfrac{2}{3}\,\bar{\sigma}\,\mathrm{sgn}(\phi)\,\mathrm{arg\ cosh}\left[1+\dfrac{(1-p)^2\sin^2\phi}{2p}\right] \end{array} \right. \tag{2.11}$$

where ϕ is a parameter in the interval $\left[-\frac{\pi}{2},\frac{\pi}{2}\right]$. Elimination of the other unknowns then allows to reduce the problem to the search for the values of two scalar unknowns only, the angle ϕ and the increment of equivalent strain $\Delta\bar{\epsilon}$.

For fixed $\Delta\bar{\epsilon}$, ϕ is found to obey a complex nonlinear equation which is solved by Newton's method. This makes ϕ a function of $\Delta\bar{\epsilon}$. The value of $\Delta\bar{\epsilon}$ is itself derived from a fixed point algorithm using a discretized form of the evolution equation (2.41). The core of the procedure of solution thus consists of two coupled iterative loops, an "external" one on $\Delta\bar{\epsilon}$ and an "internal" one on ϕ. The numerical algorithm just sketched has been implemented into the SYSTUS® finite element code developed by ESI Group.

2.1.4 Comparison experimental and numerical results

Numerical experience reveals that use of the nonlocal evolution equation (2.7) of the porosity instead of the local one (2.4) allows to greatly reduce, if not completely eliminate, mesh size effects in finite element computations. This confirms

Tvergaard and Needleman's [60] earlier findings.

We consider a pre-cracked axisymmetric tensile specimen made of A508 Cl.3 steel, for which experimental results of fracture tests are available [67]. A mesh of this specimen is shown in Figure 2.1. Advantage is taken of symmetry about the horizontal mid-plane to mesh only the upper half of the structure. The semi-height and radius are 45 mm and 15 mm, respectively. The half-opening angle and depth of the central V-shaped notch are 30° and 5 mm, respectively. A fatigue pre-crack of length 1.7 mm (invisible in the figure) originates from the notch root. Calculations are performed with both the local and nonlocal versions of Gurson's model, a value of 400 μm being used for the characteristic microstructural length b in the nonlocal computation.

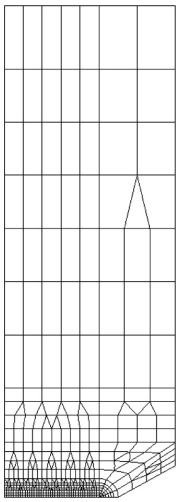

Figure 2.1: Finite element mesh of axisymmetric pre-cracked specimen

Figure 2.2 compares the experimental load-displacement curve to those got numerically. The local model can be seen to yield fantastic (although mesh-dependent) results. The results of the nonlocal model are mediocre (although mesh-independent): the predicted force remains quasi stationary for too long a period and decreases too abruptly afterwards.

A detailed analysis (not shown here) of the distribution of porosity in the ligament ahead of the crack tip reveals the origin of the problem. Whereas the porosity distribution predicted by the local model becomes highly heterogeneous in time, that predicted by the nonlocal model remains almost homogeneous at all instants. The result is that whereas the failure of the ligament is gradual with the local model; it is abrupt with the nonlocal one, the critical porosity f_c marking the onset of coalescence of voids being reached almost simultaneously at all points.

2.1.5 Anslysis of smoothing of porosity

The aim of this Section is to theoretically explain the phenomenon of excessive smoothing of the porosity resulting from the nonlocal evolution equation (2.7). Although crude and qualitative, this explanation will prove sufficient to suggest

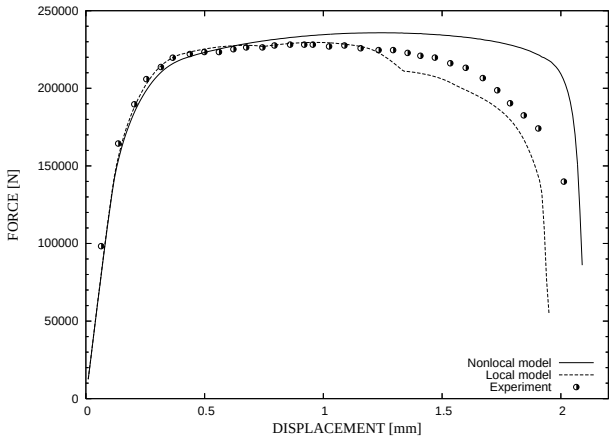

Figure 2.2: Comparison of experimental and numerical load-displacement curves - Local Gurson model and nonlocal one, first version

an efficient remedy.

Considering the "mean" and deviatoric parts of the flow rule $(2.37)_1$ and eliminating the plastic multiplier η, one gets

$$\frac{D^p_m}{D^p_{eq}} = \frac{p}{2}\frac{\bar{\sigma}}{\sigma_{eq}} \sinh\left(\frac{3}{2}\frac{\sigma_m}{\bar{\sigma}}\right) \tag{2.12}$$

where $D^p_m \equiv \frac{1}{3}\,\mathrm{tr}\,\mathbf{D}^p$ and $D^p_{eq} \equiv \left(\frac{2}{3}D^{p\,\prime}_{ij}D^{p\,\prime}_{ij}\right)^{1/2}$ ($\mathbf{D}^{p\,\prime} \equiv$ deviator of $\mathbf{D}^p$) are the mean and equivalent plastic strain rate, respectively. If the local evolution equation (2.4) is used for the porosity, combination of this equation and relation (2.12) yields (considering for simplicity only the pre-coalescence phase, during which $f^* = f$ and $p = qf$):

$$\dot{f} = kfD^p_{eq} \quad , \quad k \equiv \frac{3q}{2}\,(1-f)\frac{\bar{\sigma}}{\sigma_{eq}} \sinh\left(\frac{3}{2}\frac{\sigma_m}{\bar{\sigma}}\right). \tag{2.13}$$

Replacing the local equation (2.4) by the nonlocal one (2.7) means replacing equation $(2.13)_1$ by

$$\dot{f}(\mathbf{x},t) = \frac{1}{A(\mathbf{x})}\left[\phi * (kfD^p_{eq})\right](\mathbf{x},t) \tag{2.14}$$

where the symbol $*$ denotes the convolution product and indications of dependence upon position and time have been introduced for clarity.

We now idealize the body considered as an infinite medium and introduce the crude approximation that the quantities k and D^p_{eq} in equation (2.14) are spatially uniform. The factor $A(\mathbf{x})$ is then uniform and may be incorporated into the smoothing function ϕ, and the quantities k and D^p_{eq} may be extracted from the convolution product. Taking the spatial Fourier transform of equation (2.14), we then get

$$\frac{\partial \hat{f}}{\partial t}(\mathbf{p},t) = k(t)D^p_{eq}(t)\hat{\phi}(\mathbf{p})\hat{f}(\mathbf{p},t) \tag{2.15}$$

or equivalently

$$\frac{\partial \hat{f}}{\partial \epsilon^p_{eq}}(\mathbf{p}, \epsilon^p_{eq}) = k(\epsilon^p_{eq})\hat{\phi}(\mathbf{p})\hat{f}(\mathbf{p}, \epsilon^p_{eq}) \tag{2.16}$$

where ϵ^p_{eq} denotes the cumulated equivalent plastic strain (time-integral of D^p_{eq}).

Equation (2.16) makes it clear that the growth rate of $\hat{f}(\mathbf{p}, \epsilon^p_{eq})$ is governed by the factor $k(\epsilon^p_{eq})\hat{\phi}(\mathbf{p})$. Now the Fourier transform $\hat{\phi}(\mathbf{p})$ of a typical smoothing function (for instance a Gaussian) is positive and maximum for $\mathbf{p} = \mathbf{0}$. Thus, the growth rate of $\hat{f}(\mathbf{p}, \epsilon^p_{eq})$ is maximum for $\mathbf{p} = \mathbf{0}$, that is, when the wavelength $\lambda \equiv 2\pi/\|\mathbf{p}\|$ is infinite. This means that Fourier components of f with large wavelengths grow more quickly than Fourier components with small wavelengths, that is, spatial variations of the porosity are gradually smoothed out.

To be more specific, introduce the (again very crude) assumption that the quantity k is not only uniform in space but constant in time. Integration of equation (2.16) then yields

$$\hat{f}(\mathbf{p}, \epsilon^p_{eq}) = \hat{f}(\mathbf{p}, 0)\, \exp\left[k\hat{\phi}(\mathbf{p})\epsilon^p_{eq}\right]. \tag{2.17}$$

Thus the development of $\hat{f}(\mathbf{p}, \epsilon^p_{eq})$ in time is governed by the "growth factor" $\exp\left[k\hat{\phi}(\mathbf{p})\epsilon^p_{eq}\right]$. The ratio of the growth factors corresponding to $\mathbf{p} = \mathbf{0}$ and $\mathbf{p} \neq \mathbf{0}$ is given by

$$\frac{\hat{f}(\mathbf{0}, \epsilon^p_{eq})/\hat{f}(\mathbf{0}, 0)}{\hat{f}(\mathbf{p}, \epsilon^p_{eq})/\hat{f}(\mathbf{p}, 0)} = \exp\left\{k\left[\hat{\phi}(\mathbf{0}) - \hat{\phi}(\mathbf{p})\right]\epsilon^p_{eq}\right\}. \tag{2.18}$$

The function $\hat{\phi}(\mathbf{p})$ being maximum for $\mathbf{p} = \mathbf{0}$, the term $\{...\}$ here is positive. Thus the ratio considered is greater than unity, and can become very large in the limit of long times (large values of ϵ^p_{eq}), because of the extremely quick growth of the exponential function. This confirms that the development of Fourier components of f with large wavelengths is greatly favored with respect to that of Fourier components with small wavelengths.

The evolution equation (2.16) is *not* a diffusion equation, but does exhibit features rather similar to such an equation. Indeed, consider some imaginary diffusion equation for the porosity (the role of time being played by the cumulated equivalent plastic strain ϵ^p_{eq}),

$$\frac{\partial f}{\partial \epsilon^p_{eq}}(\mathbf{x}, \epsilon^p_{eq}) = D\,\Delta f(\mathbf{x}, \epsilon^p_{eq}), \tag{2.19}$$

where D is a constant and the symbol Δ denotes the Laplace operator. Taking the Fourier transform of such an equation, one gets

$$\frac{\partial \hat{f}}{\partial \epsilon^p_{eq}}(\mathbf{p}, \epsilon^p_{eq}) = -D\,\|\mathbf{p}\|^2 \hat{f}(\mathbf{p}, \epsilon^p_{eq}), \tag{2.20}$$

which yields upon integration

$$\hat{f}(\mathbf{p}, \epsilon^p_{eq}) = \hat{f}(\mathbf{p}, 0)\, \exp(-D\,\|\mathbf{p}\|^2 \epsilon^p_{eq}). \tag{2.21}$$

The ratio of the growth factors corresponding to $\mathbf{p} = \mathbf{0}$ and $\mathbf{p} \neq \mathbf{0}$ is then given by

$$\frac{\hat{f}(\mathbf{0}, \epsilon^p_{eq})/\hat{f}(\mathbf{0}, 0)}{\hat{f}(\mathbf{p}, \epsilon^p_{eq})/\hat{f}(\mathbf{p}, 0)} = \exp(D\,\|\mathbf{p}\|^2 \epsilon^p_{eq}). \tag{2.22}$$

This is exactly the result that one would get by expanding the term $\{...\}$ in the right-hand side of equation (2.18) to second order in $\mathbf{p}$.

2.1.6 Nonlocal Gurson Model II

The analogy between equation (2.16) and a diffusion equation such as (2.19) is helpful in the search for a remedy to the problem of excessive smoothing of the porosity. Indeed, the smoothing character of equation (2.19) clearly arises from the presence of f in the right-hand side in the form of its Laplacian: if Δf were not present, (2.19) would not be a diffusion equation and no smoothing would occur. This suggests eliminating the porosity from the right-hand side of the local evolution equation (2.4) through division of both sides by f, that is, considering this equation in the form

$$\frac{d(\ln f)}{dt} = (1 - f)\frac{\text{tr}\ \mathbf{D}^p}{f}. \tag{2.23}$$

(The presence of f in the denominator of the right-hand side here is only apparent since $\text{tr}\ \mathbf{D}^p = 3D^p_m$ is proportional to f, see equations (2.12) and (2.34)). This local equation can then be transformed into a nonlocal one in the same way as equation (2.4) was transformed into equation (2.7); that is, one may postulate that

$$\frac{d(\ln f)}{dt}(\mathbf{x}) = \frac{1}{A(\mathbf{x})}\int_\Omega \phi(\mathbf{x} - \mathbf{y}) \left[\frac{d(\ln f)}{dt}\right]^{loc}(\mathbf{y})\, dV_y \tag{2.24}$$

where

$$\left[\frac{d(\ln f)}{dt}\right]^{loc}(\mathbf{x}) \equiv (1 - f(\mathbf{x}))\frac{\text{tr}\ [\mathbf{D}^p(\mathbf{x})]}{f(\mathbf{x})}. \tag{2.25}$$

The calculations of Section 2.1.4 have been repeated using the new form (2.24) of the nonlocal evolution equation of f. Figure 2.3 shows the results obtained with this second version of the nonlocal model, together with those corresponding to the first version (equation (2.7)) and the experimental ones. One can see that replacing equation (2.7) by equation (2.24) results in considerable improvement of the agreement between experimental and numerical results. The model now correctly captures the gradual decrease of the force beyond its maximum. Also, detailed inspection of the porosity distribution in the ligament ahead of the crack tip (not shown here) no longer reveals excessive smoothing of the porosity.

2.1.7 Conclusion

With the modification proposed, Leblond *et al.*'s [58] proposal of use of some nonlocal evolution equation for the porosity within an otherwise unmodified Gurson model, appears as a solution to the problem of unlimited localization of strain and damage in this model. There are several drawbacks to the new model. The most conspicuous one is its purely heuristic character. Boundary effects also entail some

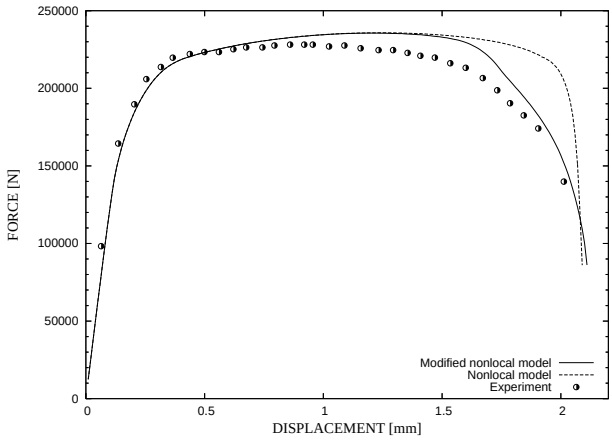

Figure 2.3: Comparison of experimental and numerical load-displacement curves - Nonlocal Gurson models, first and second versions

shortcomings.

These are good reasons to consider less directly applicable, but more theoretically satisfactory solutions to the problem of unlimited localization. An example is Gologanu *et al.*'s [68] *micromorphic* model of ductile rupture, which was derived from some extension of Gurson's [57] original homogenization procedure, based on conditions of homogeneous boundary strain rate, to conditions of *inhomogeneous boundary strain rate*.

2.2 The GLPD model of ductile rupture

2.2.1 Introduction

Constitutive models involving softening all predict unlimited localization of strain and damage. This feature generates such undesired phenomena as absence of energy dissipation during crack propagation and mesh size sensitivity in finite element computations. Gurson [17]'s famous model for porous ductile materials, which was derived from approximate limit-analysis of some elementary voided cell in a plastic solid, is no exception. In this model, unlimited localization arises from the softening because of the gradual increase of the porosity.

Several proposals have been made to solve this problem. One of these, due to Leblond *et al.* [43] but based on a previous suggestion made by Pijaudier *et al.* [50] in damage of concrete, comprises adopting a nonlocal evolution equation for the porosity involving some spatial convolution of some "local porosity rate" within an otherwise unmodified Gurson model. This simple proposal has attracted the attention of several authors (Tvergaard and Needleman [54], Tvergaard and Needleman [55], Tvergaard and Needleman [48], Enakoutsa *et al.* [11]). It was notably checked by Tvergaard and Needleman [54] that it allows to eliminate mesh size effects. Also, Enakoutsa *et al.* [11] showed that with a minor modification, it leads to great numerical reproduction of the results of typical experiments of ductile rupture.

One shortcoming of Leblond *et al.* [43]'s proposal, however, is that it is purely heuristic and lacks any serious theoretical justification. This was the motivation for a later, more elaborate and physically based proposal of Gologanu *et al.* [15]. These authors derived an improved variant of Gurson's model (the *GLPD model*[2]) through some refinement of this author's original homogenization procedure based on Mandel [21]'s and Hill [19]'s classical conditions of homogeneous boundary strain rate. In the approach of Gologanu *et al.* [15], the boundary velocity is assumed to be a quadratic, rather than linear, a function of the coordinates. The physical idea is to account in this way for the possibility of quick variations of the macroscopic strain rate, such as encountered during strain localization, over short distances of the order of the size of the elementary cell considered. The output of the homogenization procedure is a model of "micromorphic" nature involving the second gradient of the macroscopic velocity and generalized macroscopic stresses of "moment" type (homogeneous to the product of a stress and a distance), together with some "microstructural distance" connected to the mean spacing between neighboring voids.

The aim of this work was to assess the practical relevance of the GLPD model through implementation into some FE code and to study of its numerical predictions. The assessment is based on two criteria. First, numerical computations using the new model must no longer exhibit any pathological dependence upon the mesh size. Second, it must be able to reproduce the results of typical experiments of ductile rupture.

[2] GLPD: Gologanu-Leblond-Perrin-Devaux.

2.2.2 The GLPD micromorphic model for porous ductile solids

Since the original reference Gologanu *et al.* ([15]) for the GLPD model is not easily accessible, a summary of the equations of this model is given here.

Generalities In the GLPD model, internal forces are represented through some ordinary second-rank symmetric Cauchy stress tensor $\boldsymbol{\Sigma}$ plus some additional third-rank "moment tensor" $\mathbf{M}$ symmetric in its first two indices only[3]. The components of $\mathbf{M}$ are related through the three conditions

$$M_{ijj} = 0. \tag{2.26}$$

(These conditions may be compared to the condition of plane stress in the theory of thin plates or shells).

The virtual power of internal forces is given by the expression

$$\mathcal{P}^{(i)} \equiv -\int_\Omega (\boldsymbol{\Sigma} : \mathbf{D} + \mathbf{M} \vdots \nabla\mathbf{D})\, d\Omega \tag{2.27}$$

where Ω denotes the domain considered, $\mathbf{D} \equiv \frac{1}{2}\left[\nabla\mathbf{V} + (\nabla\mathbf{V})^T\right]$ ($\mathbf{V}$: material velocity) the Eulerian strain rate, $\nabla\mathbf{D}$ its gradient, $\boldsymbol{\Sigma} : \mathbf{D}$ the double inner product $\Sigma_{ij}D_{ij}$ and $\mathbf{M} \vdots \nabla\mathbf{D}$ the triple inner product $M_{ijk}D_{ij,k}$.

The virtual power of external forces is given by

$$\mathcal{P}^{(e)} \equiv \int_{\partial\Omega} \mathbf{T}.\mathbf{V}\, dS \tag{2.28}$$

where $\mathbf{T}$ represents some surface traction[4].

The hypothesis of additivity of elastic and plastic strain rates reads

$$\begin{cases} \mathbf{D} & \equiv & \mathbf{D}^e + \mathbf{D}^p \\ \nabla\mathbf{D} & \equiv & (\nabla\mathbf{D})^e + (\nabla\mathbf{D})^p. \end{cases} \tag{2.29}$$

The elastic and plastic parts $(\nabla\mathbf{D})^e$, $(\nabla\mathbf{D})^p$ of the gradient of the strain rate here do *not* coincide in general with the gradients $\nabla(\mathbf{D}^e)$, $\nabla(\mathbf{D}^p)$ of the elastic and plastic parts of the strain rate.

Hypoelasticity law The elastic parts of the strain rate and its gradient are related to the rates of the stress and moment tensors through the following hypoelasticity

[3] The component M_{ijk} is noted $M_{k|ij}$ in Gologanu *et al.* [15]'s original paper. The present notation leads to more natural-looking expressions.

[4] The general equilibrium equations and boundary conditions corresponding to the expressions (2.27) and (2.28) of the virtual powers of internal and external forces need not be given since they are not necessary for the numerical implementation.

law:

$$\left\{\begin{array}{lcl} \dfrac{D\Sigma_{ij}}{Dt} & = & \lambda\,\delta_{ij}D^e_{kk} + 2\mu D^e_{ij} \\ \dfrac{DM_{ijk}}{Dt} & = & \dfrac{b^2}{5}\left[\lambda\,\delta_{ij}(\nabla D)^e_{hhk} + 2\mu(\nabla D)^e_{ijk} - 2\lambda\,\delta_{ij}U^e_k - 2\mu\left(\delta_{ik}U^e_j + \delta_{jk}U^e_i\right)\right]. \end{array}\right. \tag{2.30}$$

In these expressions λ and μ denote the Lamé coefficients and b the mean half-spacing between neighboring voids. (In the homogenization procedure, b is the radius of the spherical elementary cell considered). Also, $\frac{D\Sigma_{ij}}{Dt}$ and $\frac{DM_{ijk}}{Dt}$ are the Jaumann (objective) time-derivatives of Σ_{ij} and M_{ijk}, given by

$$\left\{\begin{array}{lcl} \dfrac{D\Sigma_{ij}}{Dt} & \equiv & \dot{\Sigma}_{ij} + \Omega_{ki}\Sigma_{kj} + \Omega_{kj}\Sigma_{ik} \\ \dfrac{DM_{ijk}}{Dt} & \equiv & \dot{M}_{ijk} + \Omega_{hi}M_{hjk} + \Omega_{hj}M_{ihk} + \Omega_{hk}M_{ijh} \end{array}\right. \tag{2.31}$$

where $\mathbf{\Omega} \equiv \frac{1}{2}\left[\nabla\mathbf{V} - (\nabla\mathbf{V})^T\right]$ is the antisymmetric part of the velocity gradient. Finally $\mathbf{U}^e$ is a vector the value of which is fixed by equations (2.26) (written in rate form, $\frac{DM_{ijj}}{Dt} = 0$):

$$U^e_i = \frac{\lambda(\nabla D)^e_{hhi} + 2\mu(\nabla D)^e_{ihh}}{2\lambda + 8\mu}. \tag{2.32}$$

Yield criterion The plastic behavior is governed by the following Gurson-like criterion:

$$\Phi(\mathbf{\Sigma}, \mathbf{M}, \Sigma, f) \equiv \frac{1}{\Sigma^2}\left(\Sigma^2_{eq} + \frac{Q^2}{b^2}\right) + 2p\,\cosh\left(\frac{3}{2}\frac{\Sigma_m}{\Sigma}\right) - 1 - p^2 \leq 0. \tag{2.33}$$

In this expression:

- $\Sigma_{eq} \equiv \left(\frac{3}{2}\mathbf{\Sigma}' : \mathbf{\Sigma}'\right)^{1/2}$ ($\mathbf{\Sigma}'$: deviator of $\mathbf{\Sigma}$) is the von Mises equivalent stress.
- $\Sigma_m \equiv \frac{1}{3}\,\mathrm{tr}\,\mathbf{\Sigma}$ is the mean stress.
- Σ represents a kind of average value of the yield stress in the heterogeneous metallic matrix, the evolution equation of which is given below.
- p is a parameter connected to the porosity (void volume fraction) f through the relation:

$$p \equiv qf^* \quad , \quad f^* \equiv \left\{\begin{array}{ll} f & \text{if} \quad f \leq f_c \\ f_c + \delta(f - f_c) & \text{if} \quad f > f_c \end{array}\right. \tag{2.34}$$

  where q is *Tvergaard's parameter*, f_c the *critical porosity at the onset of coalescence of voids*, and δ (> 1) a factor describing the accelerated degradation of the material during coalescence (Tvergaard [52], Tvergaard and Needleman [53]).

- Q^2 is a quadratic form of the components of the moment tensor given by

$$Q^2 \equiv A_1\mathcal{M}_1 + A_2\mathcal{M}_2 \quad , \quad \left\{ \begin{array}{rcl} A_1 & = & 0.194 \\ A_2 & = & 6.108 \end{array} \right. \tag{2.35}$$

  where $\mathcal{M}_1$ and $\mathcal{M}_2$ are the quadratic invariants of $\mathbf{M}$ defined by:

$$\left\{ \begin{array}{rcl} \mathcal{M}_1 & \equiv & M_{mi}M_{mi} \\ \mathcal{M}_2 & \equiv & \frac{3}{2}M'_{ijk}M'_{ijk}, \end{array} \right. \tag{2.36}$$

  $M_{mi} \equiv \frac{1}{3}M_{hhi}$ and $\mathbf{M}'$ denoting the mean and deviatoric parts of $\mathbf{M}$, taken over its first two indices.

- Again, b is the mean half-spacing between neighboring voids.

Flow rule The plastic parts of the strain rate and its gradient are given by the flow rule associated to the criterion (2.33) through normality:

$$\left\{ \begin{array}{rcl} D^p_{ij} & = & H\dfrac{\partial\Phi}{\partial\Sigma_{ij}}(\boldsymbol{\Sigma}, \mathbf{M}, \Sigma, f) \\ (\nabla D)^p_{ijk} & = & H\dfrac{\partial\Phi}{\partial M_{ijk}}(\boldsymbol{\Sigma}, \mathbf{M}, \Sigma, f) + \delta_{ik}U^p_j + \delta_{jk}U^p_i \end{array} \right. , \; H \left\{ \begin{array}{lll} = 0 & \text{if} & \Phi(\boldsymbol{\Sigma}, \mathbf{M}, \Sigma, f) < 0 \\ \geq 0 & \text{if} & \Phi(\boldsymbol{\Sigma}, \mathbf{M}, \Sigma, f) = 0. \end{array} \right. \tag{2.37}$$

The term $\delta_{ik}U^p_j + \delta_{jk}U^p_i$ in equation $(2.37)_2$ represents a rigid-body motion of the elementary cell, which is left unspecified by the flow rule but fixed in practice by conditions (2.26).
The values of the derivatives of the yield function $\Phi(\boldsymbol{\Sigma}, \mathbf{M}, \Sigma, f)$ in equations (2.37) are readily calculated to be

$$\left\{ \begin{array}{rcl} \dfrac{\partial\Phi}{\partial\Sigma_{ij}}(\boldsymbol{\Sigma}, \mathbf{M}, \Sigma, f) & = & 3\dfrac{\Sigma'_{ij}}{\Sigma^2} + \dfrac{p}{\Sigma}\,\delta_{ij}\sinh\left(\dfrac{3}{2}\dfrac{\Sigma_m}{\Sigma}\right) \\ \dfrac{\partial\Phi}{\partial M_{ijk}}(\boldsymbol{\Sigma}, \mathbf{M}, \Sigma, f) & = & \dfrac{1}{\Sigma^2 b^2}\left(\dfrac{2}{3}A_1\delta_{ij}M_{mk} + 3A_2M'_{ijk}\right). \end{array} \right. \tag{2.38}$$

Evolution of internal parameters The evolution of the porosity is governed by the classical equation resulting from approximate incompressibility of the metallic matrix:

$$\dot{f} = (1 - f)\,\mathrm{tr}\,\mathbf{D}^p. \tag{2.39}$$

The parameter Σ is given by

$$\Sigma \equiv \sigma(E) \tag{2.40}$$

where $\sigma(\epsilon)$ is the function which provides the yield stress of the matrix material in terms of the local equivalent cumulated plastic strain ϵ, and E represents some average value of this equivalent strain in the heterogeneous matrix. The evolution of E is governed by the following equation:

$$(1 - f)\Sigma\dot{E} = \boldsymbol{\Sigma} : \mathbf{D}^p + \mathbf{M} \vdots (\nabla\mathbf{D})^p. \tag{2.41}$$

2.2.3 Numerical implementation

The GLPD model described in Section 2.2.2 has been incorporated into the SYSTUS® FE code developed by ESI Group, in the 2D case. The trickiest features of the numerical implementation, which stands as an extension of those proposed by Aravas [40] and Enakoutsa *et al.* [11] for the original Gurson model, are presented here. Emphasis is mainly placed on the complex problem of projection of the (supposedly known) elastic stress predictor onto the yield locus defined by the yield function (2.33). (This problem will be called the *projection problem* for shortness in the sequel).

The GLPD model and the class of generalized standard materials The class of *generalized standard materials*, as defined by Halphen and Nguyen [18], consists of elastic-plastic materials for which the plastic strain *plus* the internal parameters collectively obey some "extended normality rule". This class is remarkable in that as shown by Nguyen [49], for such materials, provided that the flow rule is discretized in time with an *implicit* (backward Euler) scheme, the projection problem is equivalent to minimizing some strictly convex function, which warrants existence and uniqueness of its solution.

It so happens that the GLPD model fits into the framework of generalized standard materials *for a fixed porosity*. This property is tied to the special evolution equation (2.41) obeyed by the hardening parameter E. The proof is provided in Enakoutsa's[10] thesis and is in fact a straightforward extension of that given by Enakoutsa *et al.* [11] for the original Gurson model.

This property strongly suggests adopting an *implicit* algorithm to solve the projection problem, to take advantage of the guaranteed existence and uniqueness of the solution. However, since the porosity f must not be allowed to vary for the GLPD model to be "generalized standard", it appears necessary, to benefit from this property, to use an *explicit* scheme regarding this specific parameter. Then f will be fixed during the whole calculation of the values of field quantities at time $t + \Delta t$ from their values at time t, and updated (using a discretized version of equation (2.39)) only at the end upon the convergence; the projection algorithm will then be exactly the same *as if* the porosity were a constant.

We shall therefore use the explicit estimate of the porosity at time $t + \Delta t$ given by

$$f(t + \Delta t) \simeq f(t) + \dot{f}(t)\Delta t, \tag{2.42}$$

and the explicit estimate of the parameter $p(t + \Delta t)$ resulting from there, during the whole "transition from time t to time $t + \Delta t$", but the projection algorithm developed will otherwise be fully implicit with respect to all other parameters, that is the components of the plastic strain and the plastic strain gradient and the hardening parameter E. From now on, all quantities will implicitly be considered at time $t + \Delta t$.

Parametrization of the yield locus One key point of the procedure of solution of the projection problem, aimed at reducing the number of unknowns, lies in a suitable partial parametrization of the yield locus defined by the yield function

(2.33). This parametrization is inspired from the classical one for an ellipse and obtained by looking for the maximum possible value of the quantity $\Sigma_{eq}^2 + Q^2/b^2$, namely $(1-p)^2\Sigma^2$, and then writing this quantity in the form $(1-p)^2\,\Sigma^2\cos^2\phi$ for some angle ϕ and solving the equation $\Phi(\boldsymbol{\Sigma}, \mathbf{M}, \Sigma, f) = 0$ with respect to Σ_m. One thus gets

$$\left\{\begin{array}{lcl} \Sigma_{eq}^2 + \dfrac{Q^2}{b^2} & \equiv & (1-p)^2\,\Sigma^2\cos^2\phi \\ \Sigma_m & \equiv & \dfrac{2}{3}\,\Sigma\ \mathrm{sgn}(\phi)\ \mathrm{arg\,cosh}\left[1 + \dfrac{(1-p)^2\sin^2\phi}{2p}\right] \end{array}\right. \quad , \quad \phi \in \left[-\frac{\pi}{2}, \frac{\pi}{2}\right]. \tag{2.43}$$

The sign of the parameter ϕ is introduced into equation $(2.43)_2$ in order to allow for negative as well as positive values of Σ_m.

2.2.4 Solution of the projection problem for a fixed hardening parameter

Momentarily assuming the value of the current yield stress Σ to be known, we shall now show how the projection problem can be solved through combination of the yield criterion and the flow rule. This problem will be reduced to a system of two coupled equations on the unknowns ϕ and Σ_{eq}, which are solved numerically to get

$$\boxed{\left[\frac{6\mu}{3\lambda+2\mu}(\Sigma_m{}^* - \Sigma_m) + p\,\Sigma\,\sinh\left(\frac{3}{2}\frac{\Sigma_m}{\Sigma}\right)\right]\Sigma_{eq} = p\,\Sigma\,\Sigma_{eq}{}^*\,\sinh\left(\frac{3}{2}\frac{\Sigma_m}{\Sigma}\right).} \tag{2.44}$$

and

$$\boxed{\Sigma_{eq}^2\left\{1 + \frac{A_1\mathcal{M}_1{}^{**}}{b^2\left[\Sigma_{eq} + \frac{3\lambda+2\mu}{45\mu}A_1\,(\Sigma_{eq}{}^* - \Sigma_{eq})\right]^2} + \frac{A_2\mathcal{M}_2{}^{**}}{b^2\left[\Sigma_{eq} + \frac{A_2}{5}\,(\Sigma_{eq}{}^* - \Sigma_{eq})\right]^2}\right\} = (1-p)^2\,\Sigma^2\cos^2\phi.} \tag{2.45}$$

This is the second equation of the system looked for on the unknowns ϕ and Σ_{eq}. The left-hand side depends only on Σ_{eq} and the right-hand side only on ϕ.

The simplest way to solve the system of equations (2.44, 2.45) on ϕ and Σ_{eq} may comprise using equation (2.44) to express Σ_{eq} as a function of ϕ, and inserting its expression into equation (2.45) to get an equation on the single unknown ϕ, to be solved by Newton's method. But numerical experience reveal that the convergence of the Newton iterations is then often problematic. An alternative method comprises solving equation (2.44) on ϕ through Newton iterations, Σ_{eq} being calculated as a function of ϕ at each step by solving equation (2.45) through Newton sub-iterations.

Iterations on the hardening parameter The value of the current yield stress Σ has been assumed to be known up to now. In reality, it is not and must be determined iteratively. This is done using a fixed point algorithm, starting from the value at

time t, solving the projection problem with this value, updating it using a discretized form of the evolution equation (2.41), re-solving the projection problem with the new value, etc. up to convergence.

The discretized form of equation (2.41) leads to the following expression of the increment of the hardening parameter E:

$$\begin{aligned}\Delta E &= \frac{1}{(1-f)\Sigma}\left[\frac{\Sigma'_{ij}(\Sigma'^{*}_{ij}-\Sigma'_{ij})}{2\mu}+\frac{3\Sigma_m(\Sigma_m{}^{*}-\Sigma_m)}{3\lambda+2\mu}\right.\\ &\left.+\frac{M'_{ijk}(M'^{*}_{ijk}-M'_{ijk})}{2\mu b^2/5}+\frac{3M_{mk}(M_{mk}{}^{*}-M_{mk})}{(3\lambda+2\mu)b^2/5}\right].\end{aligned} \tag{2.46}$$

Other features of the numerical implementation The numerical implementation of the GLPD model, just like that of all second-gradient models, raises a difficulty tied to the clear necessary use of the second derivatives of the shape functions. This seems to require elements of class C^1 which are never available in standard FE codes. This difficulty is circumvented through some trick suggested by Gologanu *et al.* [15] themselves and used since in several works (see, for instance, Shu *et al.* [51], Forest *et al.* [42], Matsushima *et al.* [47]) for the numerical implementation of various second-gradient models. This trick comprises introducing a new nodal variable in the form of a symmetric second-rank tensor $\mathbf{W}$, replacing the gradient of the strain rate $\mathbf{D}$ by the gradient of $\mathbf{W}$ in all equations and imposing the approximate coincidence of $\mathbf{W}$ and $\mathbf{D}$ at the Gauss points through some penalty method.

The advantage is that the components of $\nabla\mathbf{D}$ are then got from the nodal values of the new variable $\mathbf{W}$ and the sole first derivatives of the shape functions; thus, classical elements of class C^0 are sufficient. The price to pay is an increased number of nodal degrees of freedom: six $(V_1, V_2, W_{11}, W_{22}, W_{12}, W_{33})$ instead of two (V_1, V_2) in 2D. Also, Imposing the internal constraints $W_{ij} - D_{ij} = 0$ by a penalty method may give rise to locking phenomena, for which sub integration is there natural remedy. In practice, 8-node quadratic elements are used with 4-Gauss points integration. Numerical experience reveals that this suffices to prevent locking.

2.2.5 Numerical applications

Verification of absence of mesh size effects The first task is to check that use of the GLPD model allows to eliminate mesh size effects observed in numerical computations based on Gurson's standard model. No comparison with experimental results is needed for this purpose. A simple imaginary pre-notched axisymmetric tensile specimen made of A508 Cl.3 steel is therefore considered. A fine mesh of this specimen consisting of quadratic triangles and quadratic subintegrated quadrangles is shown in Figure 2.4; a cruder mesh with twice as big elements in the central region of the notch is also used. Advantage is taken of symmetry about the horizontal mid-plane to mesh only the upper half of the structure. The semi-height and radius are 5 mm and 4 mm respectively. The shape of the central notch is rectangular in a meridian plane, with semi-width 0.3 mm and depth 1 mm. The values of the material parameters are $E = 203,000$ MPa, $\nu = 0.3$, σ_0 (initial yield stress) $= 450$ MPa, $q = 1.47$, f_0 (initial porosity) $= 0.00016$, $f_c = 0.0005$ and $\delta = 2.8$.

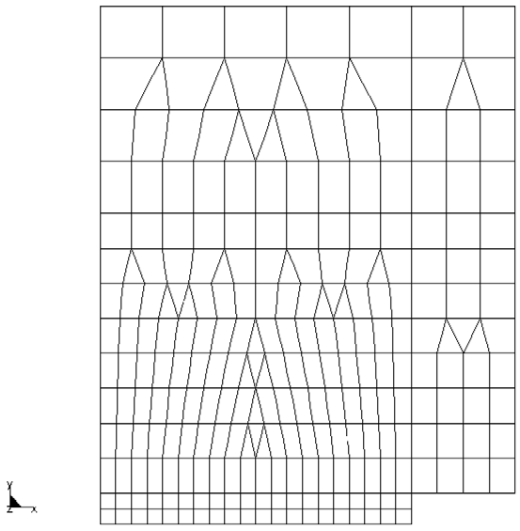

Figure 2.4: Fine mesh of a pre-notched specimen

Figure 2.5 shows the load-displacement curve obtained with both meshes, using the standard Gurson model and the GLPD model. The numbers in the upper right corner refer to the size of the square elements used in the region ahead of the notch root. There is a notable effect of mesh size in the softening region of the curves with the results with the standard Gurson model.

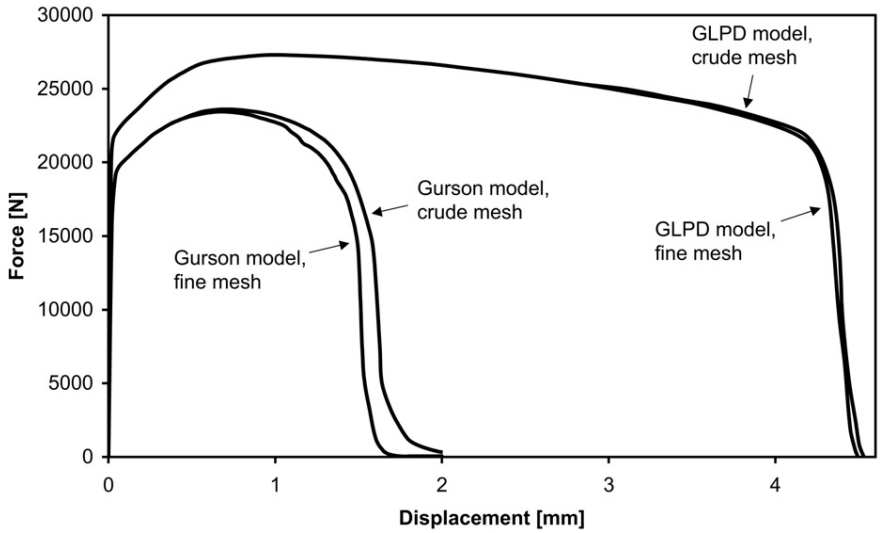

Figure 2.5: Effect of mesh size upon the load-displacement curve of a pre-notched specimen - with Gurson and GLPD models

Figure ?? also shows the results obtained with the GLPD model in a similar way. The value of the microstructural distance used is b = 2 mm. This is admittedly a very large value for a "microstructural" length, but this is of little importance here since no experimental results are available for comparison. The discrepancy between the two curves is greatly reduced, as desired, if not completely eliminated.

Numerical simulation of typical ductile fracture tests The question of agreement of the model predictions with experiments is investigated here. To do so we consider a pre-cracked axisymmetric tensile specimens TA30, where the number refers to the diameter), again made of A508 Cl.3 steel, for which experimental results of fracture tests have been provided by Rousselier and Murdhy [56]. The mesh is shown in Figure ??. Again, advantage is taken of symmetry about the horizontal mid-plane to mesh only the upper half of the specimens. Their semi-height and radius are 45 mm and 15 mm. The shape of the central notch is triangular in a meridian plane; its half-opening angle is 30° and its depth is 5 mm (TA30). A fatigue pre-crack (invisible in the figure) of length 1.7 mm originates from the notch root. The material parameters are the same as in Section 2.2.5, except that a more realistic value of 0.55 mm is used for the microstructural distance b.

Figure 2.6 shows the experimental load-displacement curves (in the form of discrete points) together with the numerical predictions (in the form of full lines) for a single pre-cracked specimens. The agreement is quite acceptable in view of the experimental errors. It is worth mentioning that in such simulations of cracked

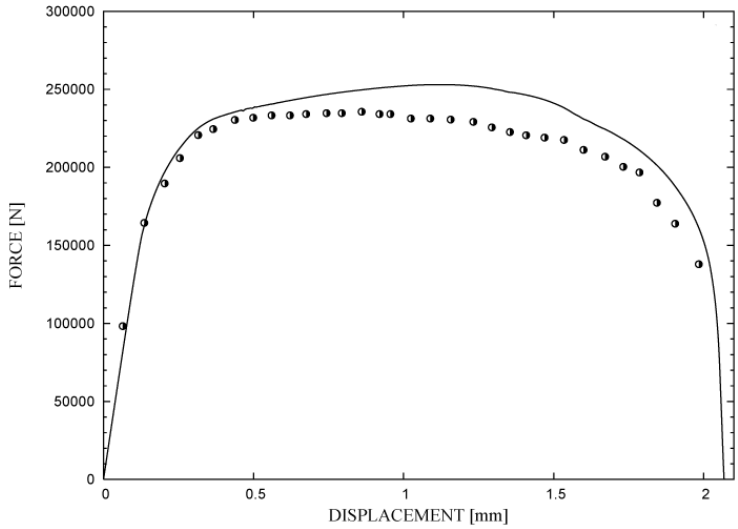

Figure 2.6: Comparison of experimental and numerical load-displacement curves of a pre-cracked TA30 specimen

structures, convergence of the global iterations (aimed at simultaneously satisfying the equilibrium equations, the yield criterion and the plastic flow rule) is often difficult. Some of the results just presented could only be obtained by replacing the true, unknown plastic parts of the increment of strain and its gradient between times t and $t + \Delta t$ by explicit estimates deduced from the values of the plastic parts of the strain and its gradient at times $t - \Delta t$ and t.

2.2.6 Conclusion

The GLPD micromorphic model of ductile rupture has been implemented into some FE programme. The major ingredient of the implementation consists of an implicit (backward Euler) algorithm used to solve the problem of projection of the elastic stress predictor onto the complex GLPD yield locus. This algorithm

ensures existence and uniqueness of the solution provided that an explicit scheme is adopted for the porosity. The problem is reduced to numerically solving a system of two equations on two scalar unknowns. Numerical applications have finally been presented with a double aim: (i) check that mesh size effects are no longer present in FE computations when the GLPD model is used instead of Gurson's; (ii) examine the quality of the agreement between numerical predictions and experimental results for some typical ductile rupture tests. The conclusion is that the GLPD model passes the two tests. It may thus be regarded as a viable solution to the problem of unlimited localization of strain and damage in Gurson's model. However numerical computations using the GLPD model are quite time-consuming, obviously because of the increased number of nodal degrees of freedom. Also, convergence of the global iterations often reveals difficult. A proposal to solve these numerical difficulties was suggested recently by Bergheau *et al.* [41] a few years after I defended my Ph.D. thesis. What follows summarizes the predictions of this algorithm which the authors, Bergheau *et al.*, kindly allowed me to report in this dissertation.

2.2.7 Bergheau *et al.*' s new algorithm for the GLPD model

Bergheau *et al.* [41] have proposed a new numerical implementation of the GLDP model aimed to address the difficulties observed in the numerical implementation of the GLPD model in Enakoutsa [10] and Enakoutsa and Leblond [12]. The main point of Bergheau *et al.* [41]'s algorithm was a trick to eliminate the additional variables using equality in a weak sense of nodal strains and strains defined by velocity fields, this has permitted to reduce the number of DOF from 6 per node in 2D finite calculations to its standard one. The trick comprises writing a constrained equation between the new nodal DOF and the strain components in a weak form as it is the usage the numerical implementation of FE problems involving dynamic effects, a "mass-matrix" thus appears on the left-hand side of the vectorial relation. Following the standard procedure adopted in the numerical implementation of dynamic problems, this matrix is lumped and inverted straightforwardly, to connect the new DOF to the nodal displacement explicitly. As expected, the reduction of the number DOF facilitated the convergence of the global elastoplastic iterations. For more details about the derivation of the algorithm the reader is referred to the works of Bergheau *et al.* [41].

Bergheau *et al.* [41]'s algorithm was validated using an analytical solution of the problem of circular bending of a beam in plane strain which we developed as a reference analytical solution during my Ph.D. thesis and which has validated the first version of the numerical implementation of the GLDP model into SYSTUS© finite element code developed by ESI Group, see Enakoutsa [10] and Enakoutsa and Leblond [12]. Let me mention briefly here that I also developed the analytical solution of an analogous model problem in Enakoutsa [13], the beam being modeled by a second gradient elasticity law I proposed following a previous suggestion of dell'Isola *et al.* [9]. An illustration of the problem model is presented in Figure 2.7. The first version of the GLPD numerical algorithm of Enakoutsa [10] and Enakoutsa and Leblond [12] and Bergheau *et al.* [41]'s modified version satisfactorily mirrored well the analytical predictions of the problem. Figure 2.8 compare the analytical and numerical results got with both Enakoutsa [10] and Enakoutsa and Leblond [12]'s as well as Bergheau *et al.* [41]'s GLPD numerical

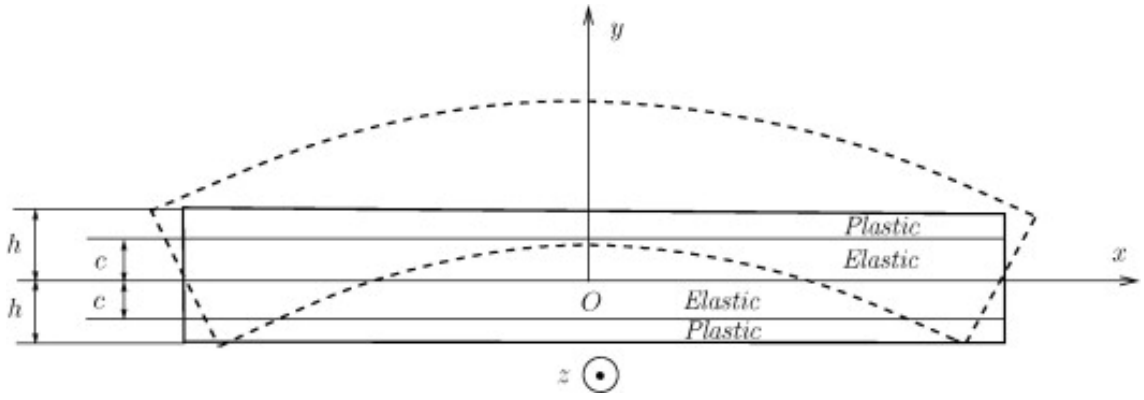

Figure 2.7: Circular bending of beam in plane strain

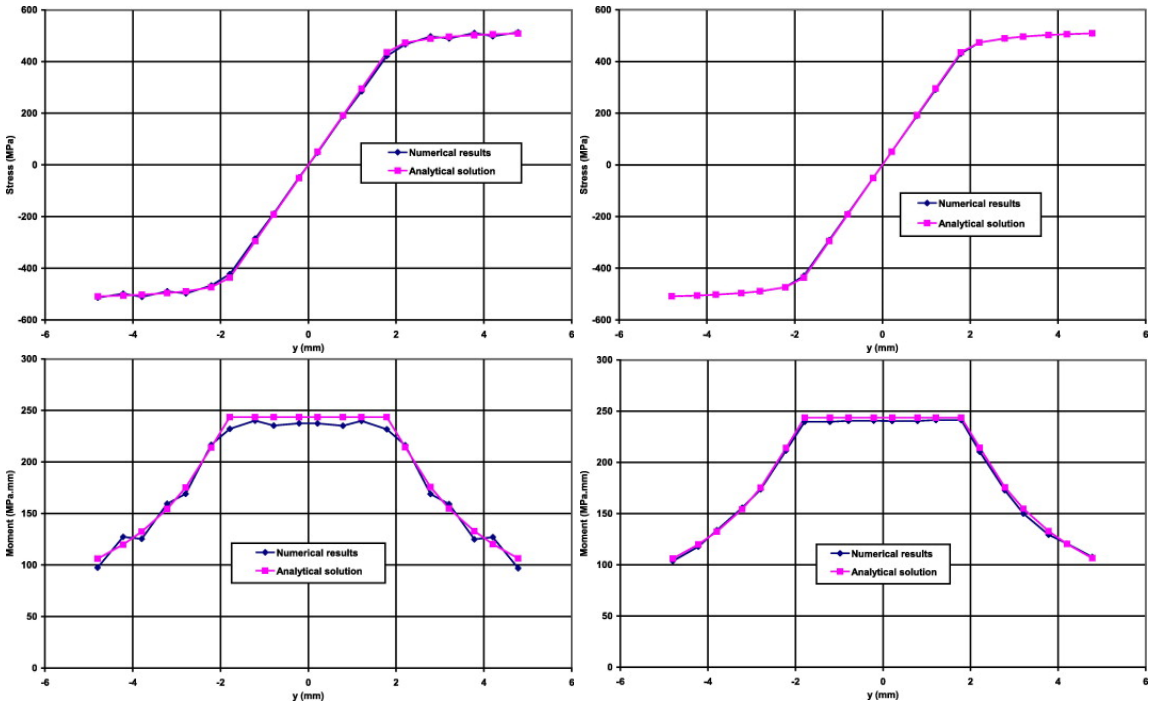

Figure 2.8: Stress and Moment Distributions in the Beam with [10] and Enakoutsa and Leblond [12]'s as well as Bergheau *et al.* [41]'s GLPD Numerical Algorithm

programmes at an instant for the components σ_{xx} of the Cauchy stress and M_{xxy}. The two distributions are given as a function of y. With no surprise, the numerical repartition of the stress linearly depends on y and reproduced accurately the analytical results for the two numerical programmes. Figure 2.8 also show that the moment is constant within the elastic zone and falls down to zero in the plastic zones which both numerical programmes predictions mirror well. However, some minor numerical oscillations resulting from numerical imperfections were observed using Enakoutsa [10] and Enakoutsa and Leblond [12]'s algorithm but as showed by ductile fracture test applications reported in Enakoutsa [10] and Enakoutsa and Leblond [12], these oscillations have no effects on the general results. The numerical oscillations disappeared with the use of Bergheau *et al.* [41]'s algorithm and

the agreement with the analytical solution is almost perfect. The improvement brought by Bergheau *et al.* [41]'s algorithm upon the results is got thanks to the interpolation scheme: quadratic for the displacement like with Enakoutsa [10] and Enakoutsa and Leblond [12]'s algorithm, but linear instead of quadratic for the strains. Given the results, the numerical implementation is accurate and elasticity (or the hypo-elasticity) and the plasticity in the GLDP model were well accounted for.

As an application, 2D numerical simulations of experiments of ductile rupture of a pre-notched and pre-cracked axisymmetric specimen and a CT specimen are performed. The calculations are pursued without difficulties up to a late stage of the rupture process, and the results are mesh-independent as it is expected in non-local models' predictions. Also, a good agreement between experimental and computed loaddisplacement curves is got for values of the parameters governing void coalescence compatible with those suggested by micromechanical numerical simulations, this could never be achieved in calculations based on Gurson [17]'s standard model, see Figure 2.9 The GLPD model was used to simulate ductile

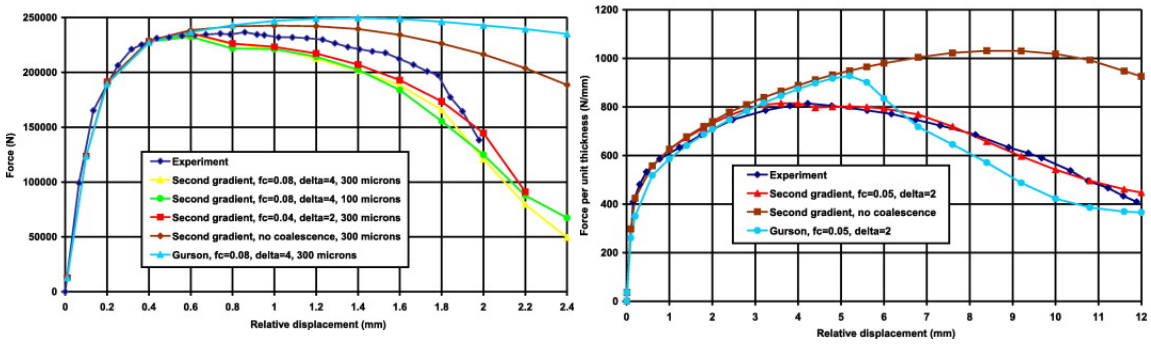

Figure 2.9: Comparison of experimental and computed loaddisplacement curves of the TA30 and CT specimen, Bergheau *et al.* [41] and Yang *et al.* [65]

rupture of the bimetallic (low-alloy/stainless) steel which is a surrogate of steel materials used in the nuclear industry, see Yang *et al.* [65]. These simulations were compared with the experimental fracture process of an interface between a ferritic (18MND5) steel and a stainless (309L) steel, joined by a Submerged Arc Welding (SAW) process, as reported in the works of Mas *et al.* [44, 46, 45]. The GLPD model predicted that the crack starts at the intersection of the cylindrical and planar free outer surfaces, on the fusion line (see Figure (2.11, 2.12) and Figure 2.10). It then propagates toward the interior of the specimen, in the decarburized zone. It remains stuck to the martensitic layer except in the immediate vicinity of the central axis of symmetry, at the end of its propagation. These results were compared with the simulation of the same structure using Gurson's model. In the simulation with Gurson's model the crack starts at the centre of the notched section of the specimen, at a distance in the deformed configuration. The crack then extends toward the free surface. It gets closer to the fusion line while propagating but never reaches it, remaining at a minimum distance in the deformed configuration, see Figure 2.10. The difference between the predictions of the two models is appealing and even though none of the two agreed with Mas *et al.* [44, 46, 45]'s experiments. Other detailed observations from Mas *et al.*

[44, 46, 45]'s work show that crack initiated near the martensitic layer which the GLPD model predicted well.

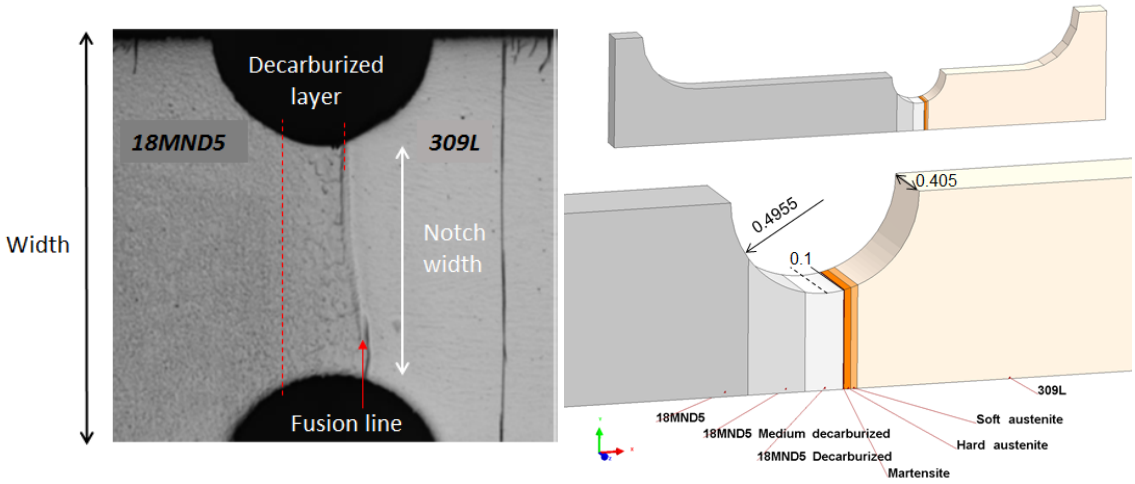

Figure 2.10: Photo of the bimetallic specimen and schematic picture showing dimensions and metallurgical structures, Bergheau *et al.* [41] and Yang *et al.* [65]

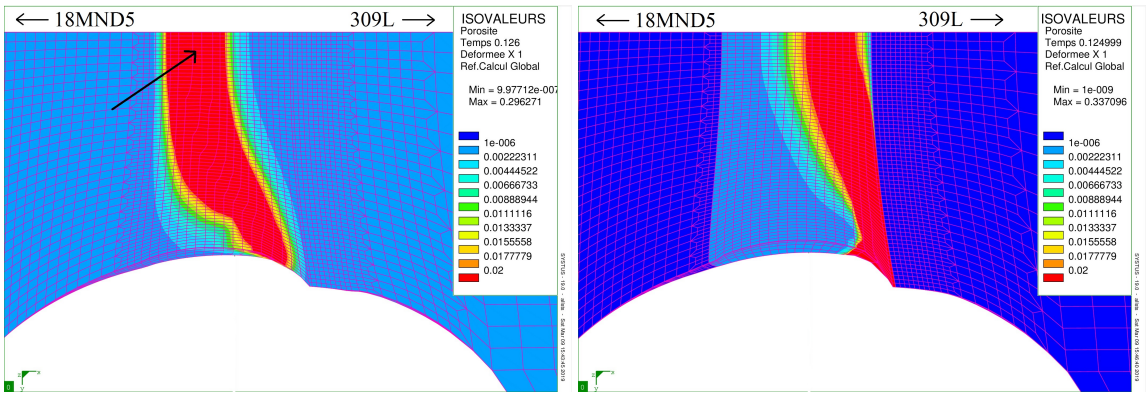

Figure 2.11: Crack paths in the bimetallic joint - External view, Bergheau *et al.* [41] and Yang *et al.* [65]

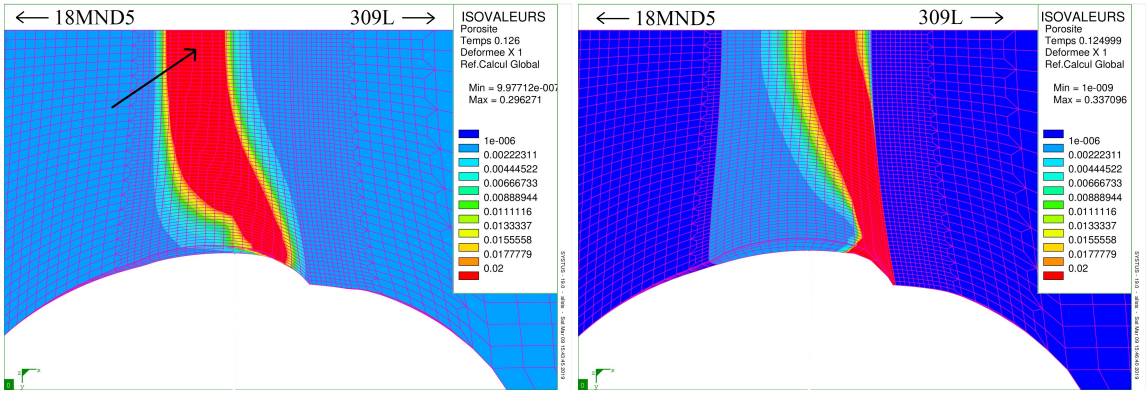

Figure 2.12: Crack paths in the bimetallic joint - View of the plane of symmetry, Bergheau *et al.* [41] and Yang *et al.* [65]

2.3 Nonlocal modeling in high velocity impact failure of metals

2.3.1 Introduction

Numerical simulations of high velocity impact related problems include classical constitutive models, which can not address the post-bifurcation mesh dependence issues, unless, they include a characteristic length scale, either in the form of spatial gradients, or integral nonlocal terms, Pijaudier-Cabot and Bazant [5] Such a length scale is added to the Bammann *et al.*'s [1] model through a manner suggested a long time ago by Pijaudier-Cabot and Bazant [5] to describe the response of aluminum (6061-T6) and steel (HY-130) disks impacted by a rigid projectile moving at various velocities. The motivation is to assess the robustness of Pijaudier-Cabot and Bazant [5]'s suggestion through the ability of the method to predict a numerical propagation of the damage free of the mesh size discretization, and to match available experimental results.

2.3.2 Nonlocal BCJ model and numerical applications

The BCJ model is a physically based plasticity/damage model rooted in J_2 deviatoric plasticity theory. The constitutive equations of this model are widely discussed in Bammann *et al.* 's [1] and has been widly used to predict dynamic ductile failure of metals and structures. Its formulation classically involves the following rate dependent yield surface:

$$\mathbf{D}^p = \sinh\left(\frac{\| \bar{\sigma}' - \bar{\alpha} \| - \bar{\kappa}}{1-\bar{\phi}}\right) \frac{\bar{\sigma}' - \bar{\alpha}}{\| \bar{\sigma}' - \bar{\alpha} \|}. \tag{2.47}$$

where $\bar{\sigma}'$ is the deviatoric part of the Cauchy stress σ, κ, and α are the isotropic and hardening laws defined y the evolution equation laws

$$\dot{\bar{\kappa}} = \left(H(\theta) - R_d(\theta)\bar{\kappa}^2\right) \| \mathbf{D}^p \| - R_s(\theta)\kappa^2 \tag{2.48}$$

$$\dot{\alpha} - \mathbf{W}_e\alpha + \alpha\mathbf{W}_e = h(\theta)\mathbf{D}^p - (r_s(\theta) + r_d(\theta) \| \mathbf{D}^p \|) \| \alpha \| \alpha \tag{2.49}$$

The damage ϕ evolves from an initial value ϕ_0 with a given $\dot{\phi}$ by the plastic strain rate $\mathbf{D}^p$ and the porosity by the relation:

$$\dot{\phi} = \left(\frac{1}{(1-\phi)^n} - (1-\phi)\right) \sinh\left(\frac{(1-n)}{(1+n)} \frac{\mathrm{tr}\sigma}{\| \bar{\sigma}' - \bar{\alpha} \|}\right) \| \mathbf{D}^p \|, \tag{2.50}$$

where n is a model parameter. Following a previous suggestion of Pijaudier-Cabot and Bazant [5], we introduce the nonlocal concept in the BCJ model by delocalizing only the equation of the damage evolution equation through the use of a convolution integral, including a Lorentz's weighting function the width of which introduces a characteristic length scale aimed at solving pathological mesh dependence issues encountered in simulations with the local BCJ model.

In the subsequent, we applied the local and nonlocal BCJ models to the numerical simulations of a high velocity impact induced damage problem using LS-DYNA© FE code. Two cases were considered, the simulations using the 6061-T6 aluminum and HY-130 steel. In the first case, a 6061-T6 aluminum circular disk of thickness 3.2mm and 57.2mm diameter is impacted by a rigid penetrator with a given initial velocity. The disk obeyed both the local and nonlocal BCJ material model behaviors, while the penetrator was assumed to be rigid. Four different mesh densities for the disk, a coarse, medium, fine and very refine mesh sizes for which the minimum element size in the impact zone is $0.24, 0.18, 0.12 \text{and} 0.08\text{mm}$, respectively, were considered. The material model parameters for 6061-T6 aluminum, determined from tensile, compressive and notch tests in Horstemeyer *et al.*'s [3] work, are used along with a characteristic length scale $\text{l} = 0.4\text{mm}$.

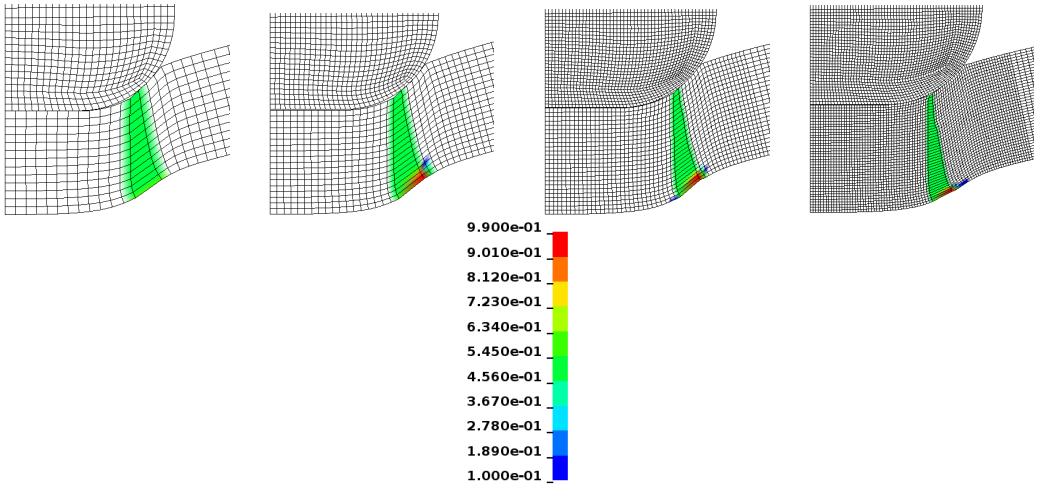

Figure 2.13: Contour plots for the damage at impact velocity 107m/s at a given time of the impact event. The simulations were performed with the local BCJ model.

Figure 2.13 illustrates, for the four different mesh sizes, the damage contours at the impact velocity of 107m/s at a time of the impact. These figures show that after the initiation of failure, the failed zone propagates through the thickness of the disk from its backside to the top side within *a layer of width one element size.* Also, once the failed zone reaches the top side of the disk, a plug is fully cut from the disk through the one element size damaged layer.

Figure 2.14 is the analogous of Figure 2.13 for the nonlocal BCJ model for a length scale $\text{l} = 0.4\text{mm}$. The localization of the damage still take place after the initiation of the damage, but the localization zone does not shrink for refine element sizes as it was the case for the computations with the local BCJ model. Also, these predictions agree well with the aluminum 6062-T6 failure experiments performed at Sandia National Laboratories and reported in Bammann *et al.* [2], see Figure 2.15.

The thickness of the disk used in the simulations with the HY-130 steel is smaller than the case with the aluminum disk and worths 2.54mm whereas, the radius re-

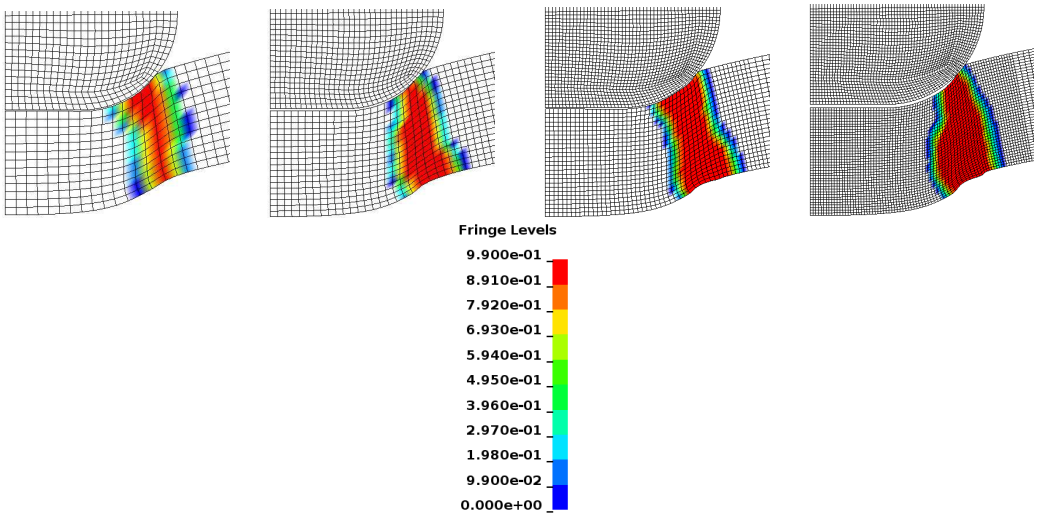

Figure 2.14: Contour plots for the damage at impact velocity of 107 m/s at a given time for the four meshes considered, using the nonlocal BCJ model with a length scale l=0.4 mm

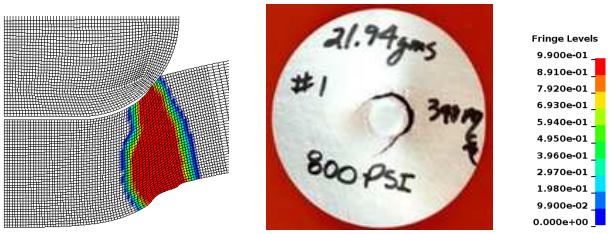

Figure 2.15: Comparison of Sandia National Laboratory experiments with the FE analyses using the nonlocal BCJ model for a length scale l=0.4 mm and a 107 m/s impact velocity.

mains the same. Here, only three different mesh densities are considered; the minimum element size in the impact region of the disk is given by $0.12, 0.08 and 0.03 mm$ for the fine, medium and coarse meshes, respectively. The constitutive parameters used in the simulations for the HY-130 steel are obtained from a series of simple experiments and are provided by Johnson and Holmquist [4].

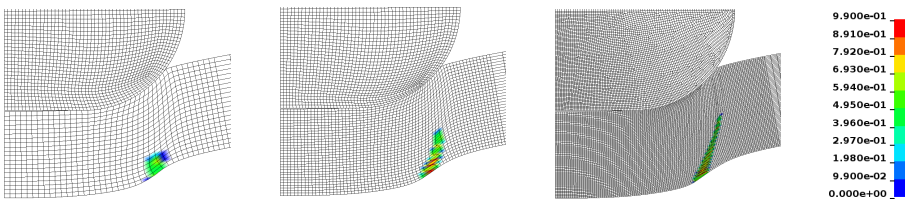

Figure 2.16: Contour plots of the damage predicted by the local BCJ model with HY-130 steel for three mesh densities in the case of the HY-130 steel and an initial velocity of 200 m/s.

Figure 2.16 illustrates the distribution of the damage predicted by the local BCJ model with the HY-130 steel for the three mesh densities and an initial velocity of 200m/s. The damage concentrates in a narrow shear band the width of which depends on the mesh discretization. The shear failure mode predicted by the calculations match the experimental observations reported by Weingarten and Revelli [6] where the steel disk failed in the diagonal. Note the difference with the aluminum disk which exhibits a tensile type failure mode.

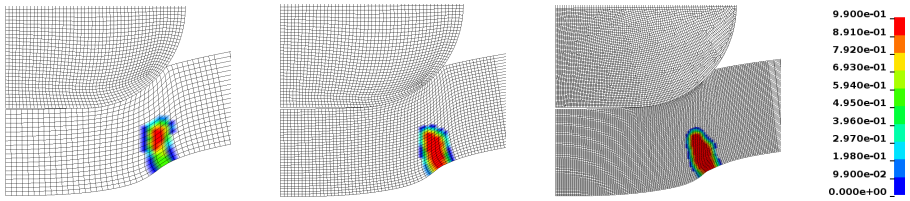

Figure 2.17: Contour plots of the damage predicted by the nonlocal BCJ model for three different mesh densities in the case of the HY-130 steel. The characteristic length scale used in the calculations l and the initial velocity are 0.25 mm and 200 m/s, respectively.

Figure 2.17 is the analogous of Figure 2.16 for a characteristic length scale $l = 0.25mm$. Here, the distribution of the damage for the three meshes, spread over several elements, are almost similar. However, these numerical predictions do not match the experimental observations of Weingarten and Revelli [6]. A distinct shear localization band does not form and the distribution of the damage follows a diagonal which is, curiously enough, in the opposite direction to the one observed experimentally. The origin of this drawback is still unclear and its investigation is left for future work.

2.3.3 Conclusion

A Pijaudier-Cabot and Bazant [5]-like nonlocal BCJ model is used to describe the response of aluminum (6061-T6) and steel (HY-130) disks impacted by a rigid projectile. Numerical results are checked to be independent of the finite element size and agreed well with the experiments for aluminum disk.

2.4 Research Project-Dynamic ductile fracture

Failure of ductile material results from voids nucleation, growth and coalescence at the microscopic scale. Under dynamic loads conditions, the cavities growth is sped up resulting in strong accelerations of matter near the internal surface of the voids. These accelerations will play a key role in the fracture's process of the material, but also on the macroscopic behavior. Molinari and co-workers (see [33], [34], [35], [36], [37], [38], [39]) used a multi-scale approach to model dynamic ductile damage. In their approach the macroscopic stress is the sum of a quasi-static contribution and a dynamic contribution. The quasi-static contribution comes from Gursons or Gologanus model. The dynamic contribution of the stress is got analytically by relying on an elementary representative volume (a hollow sphere of a spheroidal shape) and on a kinematically admissible velocity field as proposed by Gologanu (1993). These theoretical developments were incorporated into FE codes and predicted correctly problems involving dynamic loads. However, to be best of my knowledge, the post-bifurcation problems which always occur in constitutive models involving softening based on local approaches was not included in Molinari theoretical framework for dynamic fracture of materials.

2.4.1 Extension of the GLDP theory to include inertial effects

One aim of my research proposal is to address these issues by extending Molinari and co-workers theoretical framework to model dynamic ductile fracture by including one or several characteristic length scales. To do so, I am proposing to extend the Gologanu's ([15]) homogenization of a representative volume element (RVE) subjected to non-linear boundary strain rate (which has led to a micromorphic model type and has been successfully applied predict failure in several metallic structure components under static loading conditions) to include inertial effects as suggested by Molinari and co-workers. The outcome of the procedure I am proposing shall involve a third rank tensor besides the usual symmetric second rank Cauchy stress tensor. I will develop explicit relations between the macroscopic Cauchy stress and strain rate, and a third order rank tensor and strain rate gradient thanks to the application of the principle of virtual work. The third rank tensor will involve a characteristic length scale which represents the size of the RVE. I already developed some preliminary results for this procedure. I will complete the procedure by performing a limit analysis of the RVE from which a yield criterion that depends on inertial effects will be deduced. This criterion will include a parameter related to the void volume fraction (the porosity) which evolution equation will be got by assuming incompressibility of the matrix of the RVE just like with the Gurson' [17] model. The instantaneous rate of change of the plastic deformation will be related to the criterion trough normality property. Other phenomena such as strain hardening will be phenomenologically accounted for. Finally, as high rate deformation problems involve thermal effects (adiabatic shear bands in tiny localization region), I will couple the proposed mechanical model with thermal effects using both the strong and weak coupling forms.

Once the analytical model is got, I will develop numerical schemes based on a radial return algorithm (which has favored the numerical implementation of several inelastic models) to incorporate the model into a FE code (preferably LS-DYNA which is well known to be used for the numerical simulations of problems involving

dynamics fracture). Optimization routines based on experimental data available in the literature will be developed to find the proposed model parameters. Other methods such as molecular dynamics simulations can also find some model parameters and to characterize the fracture behaviors at lower length scales. The experimental data will include stress-strain curves got from tensile and compression tests on various metallic materials under different temperatures and strain rates. Along with Dr. Douglas Bammann and his students at Mississippi State University I performed a few of such experiments on a tank car body material (TC-128B Steel) in the context of the United States Department of Transportation project on *V*irtual Accident and Injury Reconstruction which are shown in Figure 5.4, 2.19, 2.20, and 2.21 below. The figures show that at room tempera-

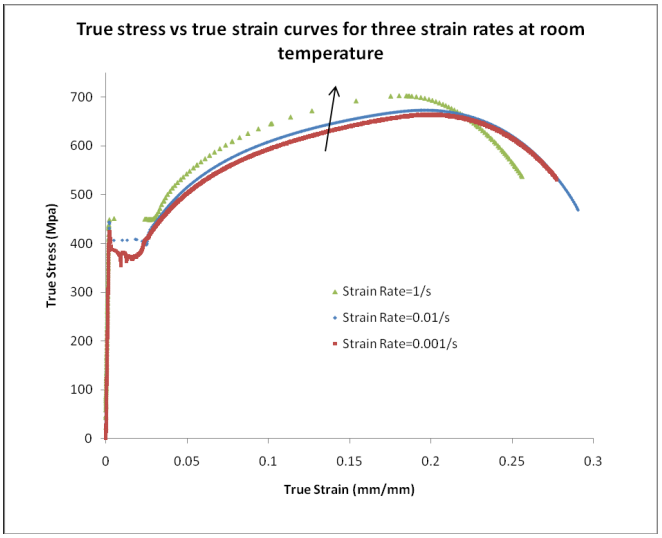

Figure 2.18: TC-128B steel round specimen tension tests at ambient temperature for different strain rates. The experimental data show that an increase in the strain rate applied to the specimen yields an increase in the strength and hardening of the material until the softening regime. Also, note that the initially high yield stress is followed immediately by a sudden drop in the stress.

ture an increase in the strain rate is followed by an increase in the hardening and strength of the TC-128B steel until the beginning of the softening regime of the material. In the softening regime of the TC-128B steel the picture is different: the curves representing the stress-strain for $0.1s^{-1}$ and $0.01s^{-1}$ strain rates are quasi similar, while the stress-strain curve corresponding to $1s^{-1}$ fall under the two others, contrary to the situation in the hardening regime. The curve also shows that the upper and lower yield strengths and yield point extension that occur on the stress-strain curve corresponding to the lower strain rate. This feature is characterized by an initially high yield stress followed immediately by a sudden drop in stress. With continuing straining the stress stays nearly constant for several percent strains before normal strain hardening begins.

I plan to augment the data base of experiment on the TC-128 B steel by performing high rate experiments under compression, tension, and torsion at high strain rates (10^3 to 10^5/ sec) on other lightweight materials. I will also consider a critical set of experiments representing fracture mechanisms that occur in engineering

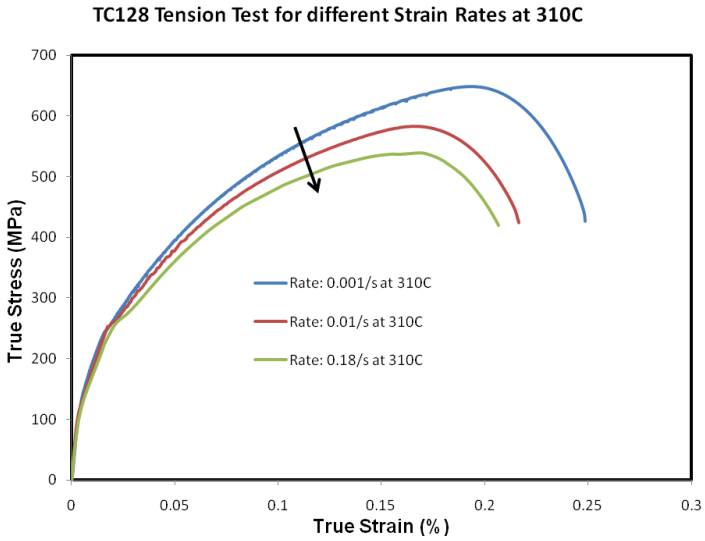

Figure 2.19: TC-128B steel tensile tests for different strain rates at 310C.The experimental data show that an increase in the strain rate yields a decrease in the strength and the hardening of material during all the loading history of the material. This might be related to a dynamic aging effects. Note that, unlike the ambient temperature tensile tests, the decrease of the material strength and hardening still hold.

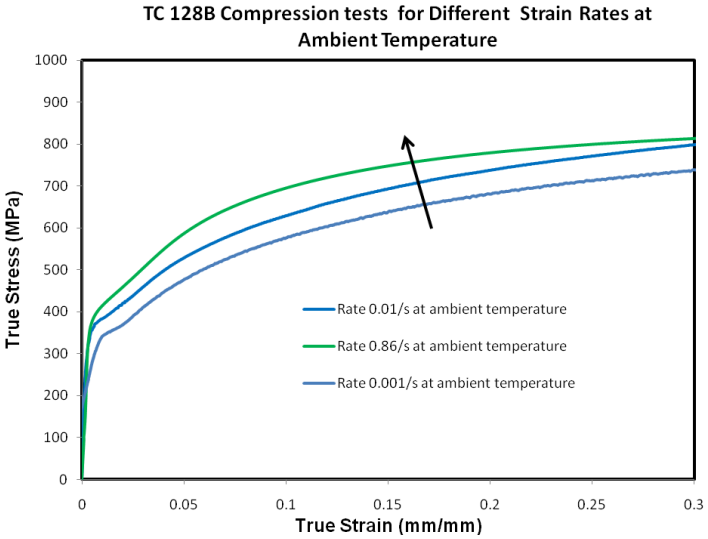

Figure 2.20: TC-128B steel round specimen compression tests at ambient temperature for different strain rates. As in the tensile tests, these figures demonstrate that an increase in the strain rate yields an increase in the strength and hardening of the material; however, the material does not show any softening regime.

applications. These experiments will validate the analytic tools I am proposing to develop. All material characterization and evaluation will require the use of high strain rate tension-compression-torsion, low and high strain rate, variable temperature environment, multiaxial fatigue loading frame, together with TEM

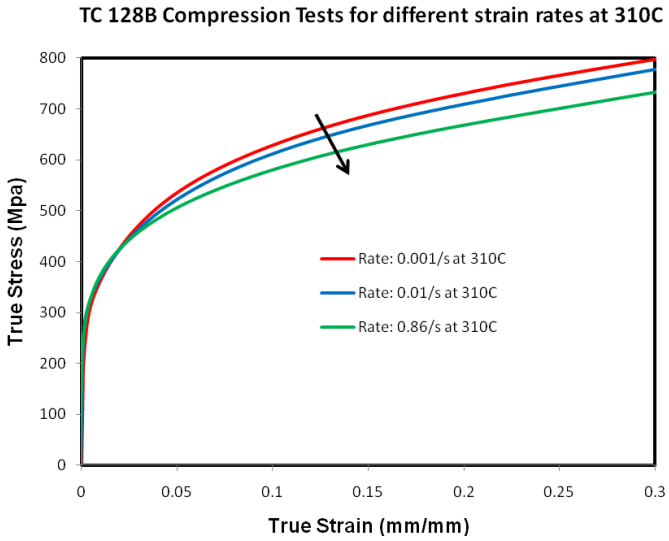

Figure 2.21: TC-128B steel round specimen compression tests at ambient temperature for different strain rates. As in the tensile tests, these figures demonstrate that an increase in the strain rate yields an increase in the strength and hardening of the material; however, the material does not show any softening regime.

(nanoscale), SEM (meso-scale), and optical microscopic (microscale) tests. Equipments required to perform these tests are available at Mississippi State University where I have a partnership with Dr. Youssef Hammi with whom I have a decade of collaborative works on material models development.

Once the dynamic ductile failure model is developed, I plan to use it to conduct post fracture fragmentation analyses of mesh free and finite element methods by explicitly calculating fragmentation projection at the structure scale of the models. The stability of the solutions will be a part of the investigation. The fragmentation analysis should allow the designers to predict fragmentation trajectory of various fracture parts got from finite element simulations, and to develop a new visualization method for use with reconstruction methods for vehicles accidents for instance.

2.4.2 Crack propagation with meshfree method

For fracture and crack propagation, I plan to develop two novel methods to assess the computational cost and an increase in accuracy over existing methods. Both methods will use FE to discretize the structure up to the point of incipient fracture, but differ in the simplicity of their implementation and the accuracy afforded by each method. The first and simplest to implement in existing FE codes, augments the FE domain by splitting element edges, allowing the crack to propagate through the FE domain with no element erosion. While working at K&C, I actively took part in implementing this approach for calculations conducted to predict the debris cloud generated by projectiles impacting quasi-brittle structures. This method, which was made for efficient large-scale calculations, provided results that compared well with debris test data.

In the second approach, the FE domain is enriched by coupling it with a Meshfree Reproducing Kernel Particle Method (RKPM) domain, which provides a robust formulation in regions where fractures are propagating or material is undergoing massive levels of deformation. This method is much more complex to implement, but can be far more accurate and robust. While working at K&C I was an active member of the development of an innovative coupled FE/RKPM algorithm and have got fantastic results that compared with penetration test data. Examples illustrating the predictions of the FE/RKPM method are displayed in Figures 2.22 and 2.23. This method evolves a FE domain dynamically into a Meshfree domain using triggering criteria provided by a dynamic fracture model using point-wise nodal coupling. The advantages of this approach that is in contrast to existing methods that convert finite elements to Smooth Particle Hydrodynamic (SPH) particles (for example, in codes like LS DYNA and ABAQUS), are the increase in accuracy afforded by RKPM in the cracked regions (to avoid mesh refinement), the use of evolution triggers natural to physics-based material models (to avoid mesh sensitivity), and the computationally efficiency provided by using FE in regions that do not fracture (to limit computational cost).

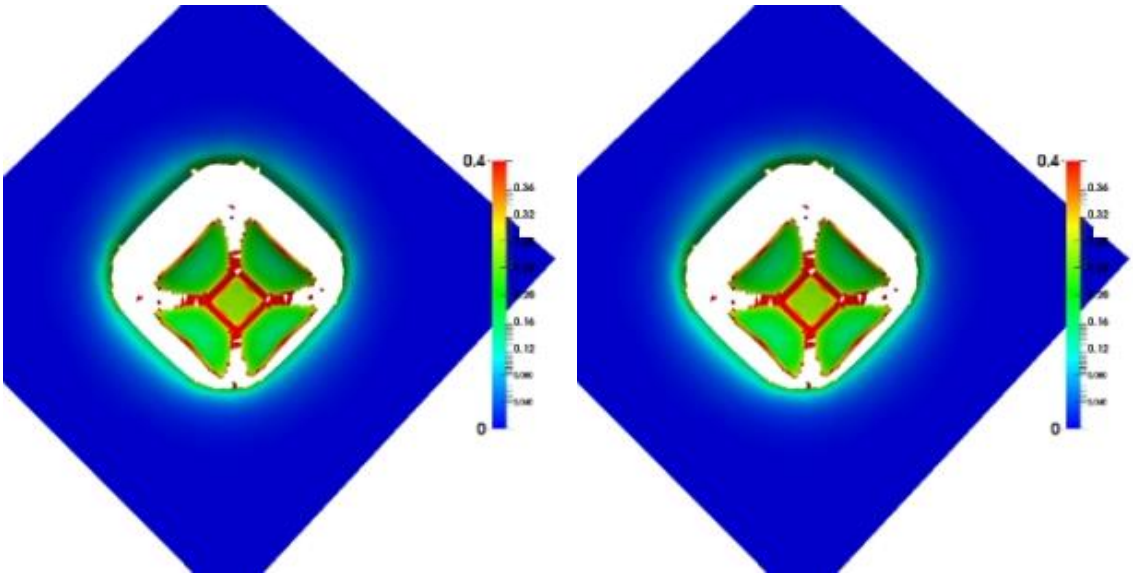

Figure 2.22: Schematic demonstration of node splitting and FE/RKPM methods coupled with BCJ model. (left) Use of element erosion with the BCJ. (right) Evolutionary FE/RKPM with the BCJ.

Both proposed methodologies will make use of damage indicators provided by the material model to evolve the element-splitting or conversion from FE to RKPM dynamically and automatically. The method is general and can be used with any validated dynamic failure model as the one I described above. The current homogenization methods these models are based do not seem to be advanced enough to build a non-local macroscopic law from microscopic hypotheses only. That is why other gradient based damage models that are thermodynamically sounds can also be considered. In this sense, I will establish a partnership with Douglas Bammann to propose a gradient-based model inspired from a recent work of Solanki and Bammann [170] to address numerical instabilities associated with

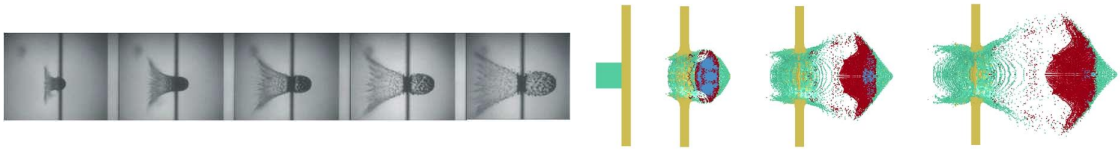

Figure 2.23: Experimental observations of the debris cloud formation during the shot of an Al1100 spherical projectile impacting an Al2024 target at a velocity 4050m/s compared with numerical simulation of fracture, fragmentation and debris formation with FE/RKPM methods, experiments adapted from Plassard *et al.* [69]

modeling the post-bifurcation regime of the material.

2.4.3 Solanki and Bammann gradient ductile damage theory

The theory will be routed in the coupling of micro force balance laws of Gurtin [16] along with a consistent thermodynamic approach; as a result, evolution equations of state variables with physical length scales consistent with both the kinematics and the thermodynamic will be obtained. The evolution equation of the damage will naturally account for the effects of damage nucleation, growth and coalescence. Extension of the thermodynamic to include other material defects (such as dislocation and disclination) and the effects of species such as hydrogen and carbon will also be considered. The framework will provide a consistent structure for multi-scale events. Once developed the model will be included into FE code with a higher number of DOF (because of gradient terms in the model) and applied to simple structures to better understand their properties, identify their limits and propose study methodologies. This last point includes in particular the question of the identification of the characteristic internal length of the material.

Chapter 3

Continuum modeling of flexoelectricity

3.1 Introduction

With the rapid developement of nanoscale technologies, there is a revival of interest in the study of flexoelectric phenomena in solid materials. The flexoelectric effect describes the generation of an electric polarization under mechanical strain or stress gradient or the reverse, that is, the mechanical field response to an electric field gradient. Early studies of this topic mostly look at liquid crystals and biomembranes. However, recently development in the nanoscale characterization of hard materials have revealed its importance also in solid structures, including flexible electronics, thin films, and energy harvesters. From a theoretical standpoint, flexoelectric effects were first predicted for crystalline dielectrics by Maskevich and Tolpygo [104], and later observed and described from a phenomenological standpoint by Kogan [97].

The theory of flexoelectricity is analogous to the polarization-gradient approach suggested by Mindlin [108] which links the polarization gradient to the strain field, see Askar and co-workers [73], Bursian and Trunov [74], and Catalan and co-workers [76] to name few. More generally, most of the works on the theoretical modeling of the flexoelectric effect result from generalized continuum approaches. The later comes from the seminal works by Lord Kelvin, the Cosserat brothers and before them by the (maybe not so universally known) Italian mathematician Gabrio Piola, and has recently (mainly due to the increase of the power of the computers) been object of intensive study in the works of Sciarra and co-workers [117], Sedov [115], Madeo and co-workers [102, 101], Rosi and co-workers [113], Pideri and Seppecher [110], Placidi and co-workers [111], dell'Isola and co-workers [80] among others. Generalized continuum theories such as micropolar and micromorphic approaches of Eringen [90] and Eringen and Suburi [91, 92] were applied to model flexoelectric effect in materials, see for instance Chen [77] and Romeo [112].

Other fundamental models of flexoelectric effects based on generalized continuum approaches result from the application of Toupin [120]-like variational principle. Among them we can mention the works of Mao and Purohit [103] and of Sharma and co-workers [119]. The governing equations of the flexoelectric effect in the works of Mao and Purohit are analagous to those of Mindlin [105, 106] strain gradient elasticity theory. The constitutive relations of the flexoelectricity model

presented by Sharma and co-workers are inspired from a previous work by Sahin and Dost [114] and include both the polarization and the second gradient of the displacement field; the contributions of the higher order terms (fifth and higher order tensors) in the internal energy were not accounted for. These approximations were necessary to reduce the number of parameters involved in Sharma and co-workers model so that practical numerical nanoscale electromechanical coupling applications based on this model are amenable.

Recent works by Enakoutsa and co-workers [87, 88] went beyond these approximations. Namely, these authors proposed a model for flexoelectric effect in materials resulting from Toupin [120] and Gao and Park [93]-like variational approaches. This model is based on an internal energy density function which generalizes the one suggested by Mao and Purohit [103] by accounting for a fifth-order tensor which represents the coupling between first and second order gradient effects (as a general rule these effects exist in all non-centrosymmetric materials) following an earlier suggestion by dell'Isola et al. [81, 83, 82, 84]. Enakoutsa and co-workers [87, 88]'s proposal was recently studied by Enakoutsa [86, 89]. In the latter works, a benchmark analytical solution of the problem of a thin-walled cylinder deformed in plane strain based on the proposed model for flexoelectric effect was developed as an application of this model. The outcome of the solution developed has clearly evidenced the correlation between the strain gradient and the electrical polarization generated, establishing thus some analytical foundations of flexoelectric based nanodevices, especially nanogenerators and nanopiezotronics devices. Also, Enakoutsa and co-workers [87, 88]'s works are in the same vein of the previous ones of Wang and co-workers [121, 122] who developed a nanogenerator system which has the potential to convert the mechanical energy produced by the mechanical bending of a zinc oxide nanowire into an electricical energy, see [78].

Similar studies aimed at designing nanoscale piezoelectric based devices exit. Among them, we can mention the works of Gao and Wang [95] where a perturbation theory was used to derive an analytical solution for the piezoelectric potential repartition in the cross section of a bending nanowire; also, Shao and co-workers [118] presented a simplified but efficient constitutive model to calculate the piezoelectric potential in a bending nanowire. Furthermore, Moemeni and co-workers [109] fabricated a nano-composite generator which consits of an array of zinc oxide nanowires based on some analytical solution. The contributions of the flexoelectric effects, which is known to be tremendous at the material lower level length scales, were neglected in the studies mentioned above, perhaps as a first step.

In this work we propose to rectify this drawback and/or to complete the very few exsiting studies that account for the flexoelectric effects in their proposed flexoelectric based nanodevice prototypes. To do so we proposed a new constituive model for flexoelectric materials, see for instance Enakoutsa and co-workers [87, 88]. The advantage of this model over its few competitors is that it accounts for more detailed physics description, which is by now required by both theoretical and applicative reasons. This model will be used to solve a few boundary value problems as part of its assessment. Problems of polarization of cylindrical tubes and hollow spheres subjected to axisymmetrical loads are solved. The chapter is organized as follows.

In Section 3.2, we present a brief review the governing equations of the flexolectric effect model as presented by Enakoutsa and co-workers [87, 88]. This model is derived from Toupin [120]-like variational formulation for electromechanical problems. The model consists of three independent constitutive relations, each of them defining some electromechanical "stress" which results from a postulated internal energy density function. A simplified version of Enakoutsa and co-workers [87, 88]'s model for the flexoelectric effect in material, which differs from the simplifications introduced by Sharma and co-workers [119], is also presented. Next, in Section ?? the simplified version of Enakoutsa and co-workers [87, 88]'s model is used to predict analytically the polarization induced over a thin spherical shell and a thick walled cylindrical tube subjected to axisymmetric loading conditions. The procedure of the solution of these problems is analogous to those developed in Gao [94], Gao and Park [93], Collins and co-workers [79]. The solutions of these simple problems offer not only a direct comparison to classical elasticity and strain gradient elasticity but also some insights into the polarization fields near point defects in flexoelectric materials

3.2 Constitutive equations

This section presents the governing equations of Enakoutsa and co-workers [87, 88]'s model for flexoelectric effect in materials as well as its simplified version.

3.2.1 Generalities

The constitutive relations of Enakoutsa and co-workers [87, 88]'s model are derived from a postulated internal energy density function $\mathcal{W}$ wich depends on the strain and its gradient as well as the polarization and its gradient, that is, $\mathcal{W} \equiv \mathcal{W}(D_{ij}, D_{ij,k}, P_i, P_{i,j})$ in the context of small displacement and deformation assumptions. The proposed internal energy density function generalizes the one suggested by Sahin and Dost [114] and adopted by Sharma and co-workers [119]; this function is defined as

$$\mathcal{W} \equiv \left\{ \begin{array}{rl} & \frac{1}{2} C_{ijkl} D_{ij} D_{kl} + \frac{1}{2} H_{ijklmn} D_{ij,k} D_{lm,n} + \frac{1}{2} \chi_{ij} P_i P_j \\ + & e_{ijk} P_i D_{jk} + G_{ijklm} D_{ij} D_{kl,m} + K_{ijkl} P_i D_{jk,l} + a_{ij} P_{i,j} \\ + & \frac{1}{2} b_{ijkl} P_{i,j} P_{k,l} + d_{ijkl} P_{i,j} D_{kl} + g_{ijk} P_i P_{k,j} \end{array} \right.$$

with

- $\mathcal{C} \equiv C_{ijkl,1\leq i,j,k,l\leq 3}$ is the usual fourth-rank "simple" elastic (stiffness) constants tensor;
- $\boldsymbol{e} \equiv e_{ijk,1\leq i,j,k\leq 3}$ represents the third-rank piezoelectric constants tensor;
- $\mathcal{H} \equiv H_{ijklmn,1\leq i,j,k,l,m,n\leq 3}$ and $\mathcal{G} \equiv G_{ijklm,1\leq i,j,k,l,m\leq 3}$ denote the sixth-rank and fifth-rank SGE elastic constants as suggested by dell'Isola and co-workers [81, 83, 82, 84];
- $\mathcal{K} \equiv K_{ijkl,1\leq i,j,k,l\leq 3}$ is the fourth-rank flexoelectric constants tensor;
- $\boldsymbol{\chi} \equiv \chi_{ij,1\leq i,j\leq 3}$ is the familiar second order reciprocal dielectric susceptibility tensor;

- $\mathbf{d} \equiv d_{ijkl,1\leq i,j,k,l\leq 3}$ is a Mindlin [107]'s fourth-order tensor which connects the gradient of polarization to the strain;
- $\mathbf{b} \equiv b_{ijkl,1\leq i,j,k,l\leq 3}$ is the polarization gradient-polarization gradient coupling fourth order tensor;
- the material constant tensor $\mathbf{g} \equiv g_{ijk,1\leq i,j,k\leq 3}$, which was introduced by Mindlin [107], links the polarization with the gradient of the polarization;
- the material constant tensor $\mathbf{a} \equiv a_{ij,1\leq i,j\leq 3}$, which was also introduced by Mindlin [107], is linked to the gradient of the polarization and is introduced to avoid strain and polarization localization at the surface of the body, see Mindlin [107];
- the vector $\mathcal{P} \equiv P_{i,1\leq i\leq 3}$ is the polarization vector field while $P_{i,j1\leq i,j\leq 3}$ is a second order tensor representing the gradient of the polarization vector;
- the comma denotes the differentiation with respect to spatial variables;
- $\mathcal{D} \equiv D_{ij,1\leq i,j\leq 3}$ is the second-rank symmetric strain tensor which is defined as

$$D_{ij} = 1/2\left(u_{i,j} + u_{j,i}\right),$$

  with $\mathbf{u} \equiv u_{i,1\leq i\leq 3}$ denoting the displacement vector field.

The elastic constants tensor $\mathcal{C}$, and the SGE constants tensors $\mathcal{H}$ and $\mathcal{G}$ in Eq.(3.1) obey the following symmetry properties

$$\begin{cases} C_{ijkl} &= C_{klij} \\ G_{ijklp} &= G_{lpijkl} \\ H_{ijklpq} &= H_{lpqijk}. \end{cases} \tag{3.1}$$

Using the symmetry properties of the strain tensor $\mathcal{D}$ we obtained some additional symmetry properties upon the tensors $\mathcal{C}$, $\mathcal{H}$, and $\mathcal{G}$ defined as

$$\begin{cases} C_{ijkl} &= C_{ijlk} = C_{jikl} \\ G_{ijklp} &= G_{jiklp} = G_{ijkpl} \\ H_{ijklpq} &= H_{jiklpq} = H_{ijkplq}. \end{cases} \tag{3.2}$$

Details on the symmetry properties of the material constant tensors $\mathbf{b}$ and $\mathbf{d}$ are provided, for instance, in Mindlin [108], while Kogan [96, 97] can be consulted for the flexoelectric effect constants tensor $\mathcal{K}$. Details studies of the mathematical properties of the flexoelectric effect constants tensor can be found in Le Quang and He [98]. The piezoelectric constants tensor $\boldsymbol{e}$ obeys the usual symmetry properties given by

$$e_{ijk} = e_{jik}.$$

3.2.2 Governing equations

The internal energy density function (3.1) is used to define an internal energy $\mathcal{E}^i$ as

$$\mathcal{E}^i = \int_\Omega \mathcal{W} dv = \frac{1}{2}\int_\Omega \left(\Sigma_{ij}D_{ij} + M_{ijk}D_{ij,k} - E_iP_i + E_{ij}P_{i,j}\right) dv \tag{3.3}$$

with the components of the Cauchy stress, Σ_{ij}, the hyperstress, M_{ijk}, the local electric force, E_i, the higher order local electric force, E_{ij}, and the gradient of the strain, $D_{ij,k}$, given by

$$\begin{cases} \Sigma_{ij} &= \dfrac{\partial \mathcal{W}}{\partial D_{ij}} = C_{ijkl}D_{jk} + G_{ijklm}D_{kl,m} + e_{ijk}P_l \\ M_{ijk} &= \dfrac{\partial \mathcal{W}}{\partial D_{ij,k}} = G_{ijklp}D_{lp} + H_{ijklpq}D_{lp,q} + K_{ijkl}P_l \\ E_i &= -\dfrac{\partial \mathcal{W}}{\partial P_i} = e_{ijk}D_{jk} + K_{ijkl}D_{jk,l} + \chi_{ij}P_j \\ E_{ij} &= \dfrac{\partial \mathcal{W}}{\partial P_{i,j}} = b_{ijkl}P_{k,l} + d_{ijkl}D_{kl} + g_{ijk}P_{k,j} + a_{ij} \end{cases} \tag{3.4}$$

and

$$D_{ij,k} = \frac{1}{2}\left(u_{i,jk} + u_{j,ik}\right), \tag{3.5}$$

$u_{i,1\leq i\leq 3}$ being the displacement vector field.

The work done by the external forces $\mathcal{E}^e$ is defined as

$$\mathcal{E}^e = \int_\Omega \left(f_iu_i + E_i^0P_i\right) dv + \int_{\partial\Omega} \left(t_iu_i + q_iDu_i\right) da \tag{3.6}$$

where

- f_i is the external body force;
- E_i^0 denotes the external electric body force;
- t_i is the Cauchy traction vector;
- q_i is the double stress traction vector;
- $\partial\Omega$ is the closed smooth bounding surface of Ω;
- Du_i is the normal (directional) derivative of the displacement component u_i defined by

$$Du_i = n_lu_{i,l} \tag{3.7}$$

with n_l being the outward unit normal vector to the surface $\partial\Omega$. Let us mention that the integrand $(t_iu_i + q_iDu_i)$ in the right-hand of Eq.(3.6) was also adopted by Gao and Park [93].

We shall now apply Toupin and Mindlin [120, 107]-like variational approaches to obtain both the balance equations and the boundary conditions. To do so, an additional term is needed in the integrand (the energy density function) of the energy density (3.1) to be consistent with Toupin [120] and Mindlin [107] variational approaches; thus, the new energy density function is given by

$$\mathcal{W} = \left\{ \begin{array}{rl} & \frac{1}{2}\left(\Sigma_{ij}D_{ij} + M_{ijk}D_{ij,k} - E_iP_i + E_{ij}P_{i,j}\right) \\ - & \frac{1}{2}\epsilon_0\left(\nabla\Phi\right)_i\left(\nabla\Phi\right)_i + \left(\nabla\Phi\right)_i P_i \end{array} \right.$$

with Φ being an electric potential which is related to the local electric force E_i as

$$E_i = \left(\nabla\Phi\right)_i \tag{3.8}$$

With this new expression of the density function, the variational approaches of Toupin and Mindlin [120, 107] as well as Gao and Park [93] can be applied to the internal energy (3.8) and the external energy (3.6) in a body occupying a volume Ω bounded by a surface $\partial\Omega$, separating Ω from the external environement $\Omega^\star$ to obtain, in the context of quasi-static analyses, the following balance equations

$$\left\{ \begin{array}{l} \Sigma_{ij,j} - M_{ijk,jk} + f_i = 0 \\ E_i + E_{ij,j} - \left(\nabla\Phi\right)_i + E_i^0 = 0 \\ -\epsilon_0\left(\nabla\Phi\right)_{ii} + P_{i,i} = 0 \quad in \quad \Omega \\ \left(\nabla\Phi\right)_{ii} = 0 \quad in \quad \Omega^\star \end{array} \right. \tag{3.9}$$

and the boundary conditions

$$\left\{ \begin{array}{rcl} \Sigma_{ij}n_j - \left(M_{ijk}n_k\right)_{,j} + \left(M_{ijk}n_kn_j\right)_{,l}n_j & = & t_i \\ M_{ijk}n_jn_k = q_i & & \\ n_i\left(-\epsilon_0\left[\left[\left(\nabla\Phi\right)_i\right]\right] + P_i\right) = 0 & & \\ n_iE_{ij} = 0 & & \end{array} \right. \tag{3.10}$$

where $\left[\left[\left(\nabla\Phi\right)_i\right]\right]$ is the jump in $\left(\nabla\Phi\right)_i$ across the bounding surface of the body Ω.

Eqs.(3.5) and (3.4) along with the boundary conditions (3.10) constitute the governing equations for the model proposed by Enakoutsa [87, 88] for elastic flexoelectric materials under small deformation assumptions.

3.2.3 Simplified version

This section presents a version of Enakoutsa and co-workers [87, 88]'s model when the material is centrosymetric where the classical piezoelectric effect is absent. In this case, according to Mindlin [107], the piezoelectric coefficients tensor $e_{ijk,1\leq i,j,k\leq 3}$, the "Mindlin constants" tensor $g_{ijkl,1\leq i,j,k,l\leq 3}$ which links polarization with the gradient of the polarization as well as the fifth rank strain gradient elastic tensor $G_{ijklm,1\leq i,j,k,l,m\leq 3}$ vanish. Therefore, the electromechanical forces (3.4) reduce to

$$\begin{cases} \Sigma_{ij} &= C_{ijkl}D_{jk} \\ M_{ijk} &= H_{ijklpq}D_{lp,q} + K_{ijkl}P_l \\ E_i &= K_{ijkl}D_{jk,l} + \chi_{ij}P_j \\ E_{ij} &= b_{ijkl}P_{k,l} + d_{ijkl}D_{kl} + a_{ij} \end{cases} \tag{3.11}$$

For the particular case of linear isotropic materials, the strain gradient elastic constants in the reduced electromechanical forces relations Eq.(3.11) are reduced to those of dell'Isola and co-workers [81] which result from some material symmetry arguments previously proposed by Suicker and Chang [116]. Also, the electromechanical coupling coefficients tensors $\chi_{ij,1\leq i,j\leq 3}$, $K_{ijkl,1\leq i,j,k,l\leq 3}$, $d_{ijkl,1\leq i,j,k,l\leq 3}$ and $b_{ijkl,1\leq i,j,k,l\leq 3}$ simplified to those obtained by Masson [99] and Mindlin [107] and used in Maranganti and coworkers [100] so that the electromechanical stress relations (3.11) become:

$$\begin{cases} \Sigma_{ij} &= \lambda D_{kk}\delta_{ij} + 2\mu D_{ij} \\ M_{ijk} &= 2c_1 D_{kp,p}\delta_{ij} + c_1 D_{pp,j}\delta_{ik} + c_1 D_{pp,i}\delta_{jk} + c_2 D_{ll,k}\delta_{ij} \\ &+ 2c_3(D_{jq,q}\delta_{ik} + D_{iq,q}\delta_{jk}) + 2c_4 D_{ij,k} + 2c_5(D_{ik,j} + D_{jk,i}) \\ &+ \delta_{ij}k_{12}P_k + k_{44}(\delta_{ik}P_j + \delta_{jk}P_i) \\ E_i &= k_{12}D_{ik,k} + k_{44}(D_{ji,j} + D_{jj,i}) + \chi P_i \\ E_{ij} &= b_{12}\delta_{ij}P_{k,k} + b_{44}(P_{j,i} + P_{i,j}) + b_{77}(P_{j,i} - P_{i,j}) \\ &+ d_{12}\delta_{ij}D_{kk} + 2d_{44}D_{ij} + a\delta_{ij} \end{cases} \tag{3.12}$$

where

- the symbol δ_{ij} denote the Kronecker delta tensor;
- the coefficients $c_{i,1\leq i\leq 5}$ are the strain gradient elastic material constants of dell'Isola and co-workers [81];
- the constants k_{ij} represent the non-zero flexoelectric coupling effect moduli;

- the constants b_{ij} and d_{ij} are the Masson [99] and Mindlin [107] non-zero electromechanical coupling effect modulii;
- λ and μ denote the usual Lame elastic stiffness tensor

The relations (3.12) include sixteen constitutive constants; along with the balance equations and boundary conditions Eqs.(3.9, 3.10), these relations define a simplified version of Enakoutsa and co-workers [87, 88]'s model for the flexoelectric effect in linear elastic solids. The practical used of this version of the model is demonstrated in the two following sections.

3.2.4 Application of the model: the thin-walled nanowire problem

In this section, I present a closed form analytical solution for the problem of a thin-walled cylindrical nanowire made of zinc oxide subjected to some external pressure. The nanowire is of inner and outer radii r_i and r_e, respectively and obeys the constitutive relations (3.12) where the strain gradient elastic coefficients $c_{i,1\leq i\leq 5}$ are given as functions of the Lame elastic coefficients λ and μ, following a suggestion made by Gologanu and co-workers [15] and studied by Enakoutsa [10] and Enakoutsa and Leblond [12] some years ago. In Gologanu and co-workers [15]'s proposal, the strain gradient elastic constants are related to the Lame elastic coefficients as

$$\left\{\begin{array}{lcl} c_1/(b^2/5) & = & -\frac{\lambda}{4} \\ c_2/(b^2/5) & = & \lambda \\ c_3/(b^2/5) & = & \left(\frac{\lambda}{16}-\frac{\mu}{4}\right) \\ c_4/(b^2/5) & = & \mu \\ c_5 & = & 0 \end{array}\right. \tag{3.13}$$

with the parameter b representing some material charateristic length scale. The problem is assumed to be a plane strain problem and for this reason the component of the displacement in the z-direction is assumed to be equals to zero. Use is made of the classical cylindrical coordinates r, θ and z and the corresponding orthogonal basis e_r, e_θ, e_z and the following property on a radial vector $\mathbf{W} \equiv \Delta U$:

$$(\nabla D)_{hhi} = U_{h,hi} = W_i \quad \text{and} \quad (\nabla D)_{ihh} = U_{i,hh} = \Delta U_i,$$

that is,

$$(\nabla D)_{hhi} = (\nabla D)_{ihh} = W_i. \tag{3.14}$$

The canonic decomposition Eq.(3.14) was invented by Enakoutsa [10] and later used in the solution of several boundary problems involving curvilinear coordinates, see Enakoutsa [85, 86] to name few. Figures (3.1,3.2) illustrate this model problem.

We want to find axi-symmetric solutions where the displacement vector field $\mathbf{U}$, the polarization vector field $\mathbf{P}$ and the electric potential field Φ are assumed to be radial, which means that $\mathbf{U} \equiv U(r)e_r$, $\mathbf{P} \equiv P(r)e_r$ and $\Phi \equiv \Phi(r)$. The procedure of solution of the thin-walled cylindrical problem consists of finding the

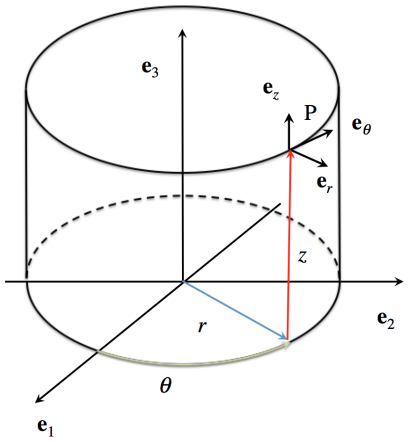

Figure 3.1: Cylindrical coordinates associated with the problem model

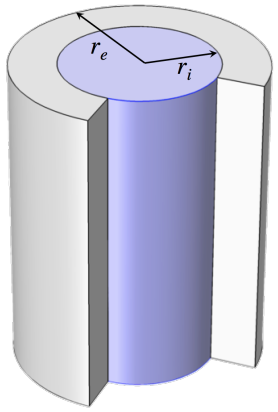

Figure 3.2: Polarization of the cylindrical tube undergoing axisymmetric loading model problem

radial displacement field and deduces the polarization vector field using the balance equations Eqs.$(3.9)_{1,2}$ and then calculate the electric potential Φ. We start by taking the spatial derivatives of the stress and the higher order electric force as well as the second spatial derivatives of the hyperstress in Eq.$(3.12)_{1,2}$. Using the properties (3.14) and the constitutive constants (3.13) we get, after derivation and application of the Kronecker delta symbol:

$$\begin{cases} \Sigma_{ij,j} &= (\lambda + 2\mu)\, W_i \\ M_{ijk,jk} &= 2\dfrac{\mu b^2}{5}\dfrac{\lambda+2\mu}{\lambda+4\mu}(\Delta W)_i + (k_{12}+k_{44})\, P_{k,ik} + k_{44}(\Delta P)_i \\ E_i &= (k_{12}+2k_{44})\, W_i + aP_i \\ E_{ij,j} &= (d_{12}+2d_{44}+b_{12}+2b_{44})\, W_i. \end{cases} \tag{3.15}$$

Using the relations (3.15) in the balance equations (3.9) we get the following re-

duced system of equations:

$$\begin{cases} W_i - \dfrac{2\mu}{\lambda+4\mu}\dfrac{b^2}{5}(\Delta W)_i + \dfrac{k_{12}+k_{44}}{\lambda+2\mu}P_{k,ik} + \dfrac{k_{44}}{\lambda+2\mu}(\Delta P)_i = 0 \\ \\ \left(k_{12}+2k_{44}+d_{12}+2d_{44}+b_{12}+2b_{44}\right)W_i + aP_i - (\nabla\Phi)_i = 0 \end{cases} \tag{3.16}$$

in the absence of body external mechanical and electrical forces, that is, $f_i = E_i^0 = 0$. The system of equations (3.16) then reduces

$$\begin{cases} W_i - \dfrac{2\mu}{\lambda+4\mu}\dfrac{b^2}{5}(\Delta W)_i + k^2 P_{k,ik} + k^3(\Delta P)_i = 0 \\ \\ k^4 W_i - (\nabla\Phi)_i + \chi P_i = 0 \end{cases} \tag{3.17}$$

where

$$\begin{cases} k^2 &= \dfrac{k_{12}+k_{44}}{\lambda+2\mu} \\ \\ k^3 &= \dfrac{k_{44}}{\lambda+2\mu} \\ \\ k^4 &= k_{12}+d_{12}+b_{12}+2\left(k_{44}+d_{44}+b_{44}\right). \end{cases} \tag{3.18}$$

Using the component $(3.9)_3$ of the balance equations (3.9), Eqs.(3.19, 3.18) reduce to

$$\begin{cases} W_i - 2\dfrac{\mu b^2}{5}\dfrac{\lambda+2\mu}{\lambda+4\mu}(\Delta W)_i + k^2 P_{k,ik} + k^3(\Delta P)_i = 0 \\ \\ k^4 W_i - \chi' P_i = 0 \end{cases} \tag{3.19}$$

Upon substituting of $(3.19)_2$ into Eq.$(3.19)_1$, we find

$$W_i - 2\frac{\mu b^2}{5}\frac{\lambda+2\mu}{\lambda+4\mu}(\Delta W)_i + k^2 P_{k,ik} - \frac{k^3 k^4}{\chi'}(\Delta W_i) = 0. \tag{3.20}$$

Remembering that both the displacement and polarization vector fields only depend on the radial coordinate r, Eq.(3.20) becomes

$$W_r - \left(2\frac{\mu b^2}{5}\frac{\lambda+2\mu}{\lambda+4\mu} + \frac{\left(k^2+k^3\right)k^4}{\chi'}\right)(\Delta W)_r = 0 \tag{3.21}$$

or in compact form

$$\mathbf{W} - k(\Delta\mathbf{W}) = 0; \quad k = 2\frac{\mu b^2}{5}\frac{\lambda+2\mu}{\lambda+4\mu} + \frac{\left(k^2+k^3\right)k^4}{\chi'} \tag{3.22}$$

The solution of the differential equation Eq.(3.22) is well-known and yields

$$U(\rho) = D_1 I_1(\rho) + D_2 K_1(\rho) + D_3 \rho + \frac{D_4}{\rho}. \tag{3.23}$$

In Eq.(3.23)

- $\rho = \sqrt{k}r$ and the definitions of the constants $D_{i,1\leq i\leq 4}$ (the values of these constants will be fixed by the boundary conditions of this problem) have been changed
- I_1 and K_1 are the modified Bessel functions of the first and second kinds of order one, respectively.

3.2.5 Application of the model: polarization of a thin spherical shell

This section is devoted to the solution of a polarization problem for a thin spherical shell deformed under axisymmetric loading conditions problem, the deformation being inhomogeneous. The matrix of the shell is supposed to be linear elastic, obeying the constitutive relations decribed above. The model problem is illustrated in Figure (3.3). The problem under consideration involves spherical sym-

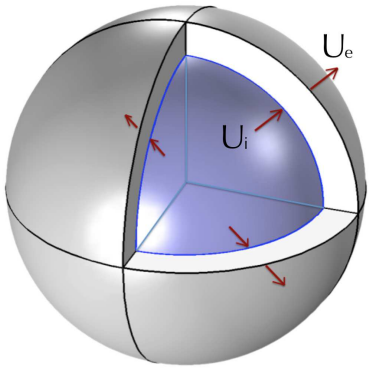

Figure 3.3: Polarization of a thin spherical shell undergoing axisymmetric loading model problem

metries, hence the displacement and polarization vector fields (denoted here by $\mathbf{U} \equiv U_r$ and $\mathbf{P} \equiv P_r$, respectively) in the spherical shell are radial. The derivation of the solution of this problem is analogous to the case of the polarization of the cylindrical shell problem; the balance equations are combined with the consitutive laws as defined above to get the radial displacement and polarization fields as:

$$U(x) = \alpha\left(1/x - 1/x^2\right)e^x + \beta\left(1/x + 1/x^2\right)e^{-x} + \gamma x + \delta/x^2. \tag{3.24}$$

$$P(x) = \alpha_1\left(1/x - 1/x^2\right)e^x + \beta_1\left(1/x + 1/x^2\right)e^{-x} \tag{3.25}$$

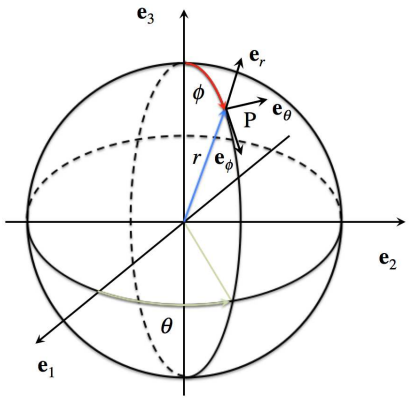

Figure 3.4: Polar coordinates associated with the problem model

In Eqs.(3.24,eqn:PoleVect) the variable $\chi \equiv kr$, and α, β, γ, δ, α_1, and β_1 represent integration constants which are fixed through constitutive boundary conditions and imposed boundary conditions.

The analytical solutions developed raise several points of interest which are presented as follows.

- The displacement vector field includes the combined effects of strain gradient elasticity and flexoelectricity. The magnitude of the displacement field vector is substantially reduced with respect to the classical elasticity and strain gradient elasticity solutions. The explanation is that in flexoelectric materials some part of the external forces work is employed to polarize the material, unlike in elastic materials where all the work produced by the external forces is stored in the material as an elastic energy.
- The polarization vector field is also significantly affected by the flexoelectric effects. The polarization in the spherical shell and cylinder is determined by the combined effects of strain gradient through the constants and the flexoelectric constants.
- When the strain gradient constants vanish, the spherical shell is still polarized (strain gradient-polarization couplings) according to the formula (3.25) through the flexoelectric constants. Eq.(3.25) also shows that the polarization vector field can be controlled by the mechanical loading parameters. However, it is not clear from this equation how mechanical loading will affect the polarization of the spherical shell.

3.3 Research project

Along with partners at the Sapienza University of Rome, I proposed a continuum mechanics based model to predict flexoelectricity in materials at nanoscale and applied the model to various small scale structure problems under different mechanical and electrical loads. The model can describe how flexoelectricity influences the electromechanical coupling behaviors of the materials; however, there

are several limitations and other aspects of the model that require further developments. These areas of improvement are as follows.

- When deriving the governing equations and the boundary conditions, we considered simplifications in the formulation process, including higher order couplings between the strain and strain gradients and the strain gradient and the polarization gradient. These coupling effects, however, may have a significant influence on the size effects in nano piezoelectric materials for instance. Inelastic behaviors and large strains effects were also disregarded in the model.

- Also, surface effects such as surface piezoelectricity, surface electricity and surface stress were neglected in the model even though it is well established that these effects, from experimental view points, influence several nanoscale piezoelectric materials' properties, including the size dependent effects.

- The flexoelectricity model does not include dynamic effects which are critical when considering vibrational behaviors. I plan to study how flexoelectricity affects wave propagation, especially in structures with periodic cells. The failure mechanisms and material defects effects (dislocations and disclinations) were also neglected. I plan to investigate dynamic crack growth in flexoelectric materials which yields electro-magnetic radiation because of the time dependent electrical field. Problems in which flexoelectricity influences nano-scale structures' stabiity (buckling) will also be considered.

In this research proposal, I plan to augment the predictive capabilities of the model we developed by incorporating all the features listed above. I will also develop numerical algorithms based on finite-difference or finite element method with a high order DOF or their variants and applied to several problems of interest to predict the behavior of complicated structures. For instance, I plan to develop a mixed formulation based on a suggestion of Amanatidou and Aravas [72] to address the higher-order differential governing equations because of the flexoelectricity in the constitutive equation of the model. Other numerical framework such as the one we used to implement the GLPD model which introduced the penalization of the gradient term will also be explored.

Another phenomenon of interest which is directly related to flexoelectricity is the pyro-paraelectricity. Chin *et al.* [75] have proposed to use the gradient effects through flexoelectricity to create thermal-electric sensor devices. This area of research is at infancy and new modeling development are required to complete the available experimental work, which are also new. In this research effort, I will explore different modeling methods for this phenomenon based on generalized continuum modeling approach of Toupin. I hope that this research effort will lead to a better understanding of pyro-paraelectricity from a modeling standpoint point.

The new capabilities for flexoelectric and pyro-paraelectric materials will include several constitutive material model parameters which I plan to find through molecular dynamic simulations or homogenization methods. The results will be useful for developing a virtual electromechanical functional materials laboratory (which will include electromechanical material models, experimental data, model parameters, and high performance numerical algorithms.) The findings of this laboratory

will be enabled rationalized design, optimization and scaleup of sensors, actuators and energy harvesters based on the principle of flexoelectricity.

Chapter 4

Modeling dislocations and disclinations defects

4.1 Introduction

A polycrystalline material deforms upon exposure to an external load, and subsequently, its grains rotate to align themselves to the direction of the imposed boundary conditions. At large strains, geometrical necessary dislocations (GNDs), boundaries (GNBs) and disclinations (GNDcls) are started in the material as an energetically favorable alternative to the formation of gaps, overlaps and holes. In a continuum modeling of the behavior of polycrystalline materials this is described by geometrically necessary dislocation densities (the torsion of the space) and disclination densities (curvature of the space), as showed in Clayton et al. [134]. The main reason for which dislocation and disclination defects are to be introduced in the continuum modeling is that such defects convey important implications regarding size effects and self-organization of dislocation substructure which has become increasingly clear in experimental characterization at finer length scales, see here also the work of Clayton et al. [134]. For example, in the bending of thin nickel beams, Stolken and Evans [174] observed that plastic work hardening increases sharply with a decrease in the thickness of the thin beams. In torsion tests, Fleck et al. [142] found that the torque normalized by the twist of a thin wire of copper of diameter 12 microns was at least three times as high of that in a wire with a diameter of 120 microns. Tests performed at the micro or nano scale, such as a nano-indentation (see the works of Ma and Clarke [154], McEkhaney et al. [157], Pool et al. [164], and Stelmashenko et al. [171]), showed that the micro-hardness of materials is considerably higher than the macro-hardness. It is widely accepted that hardness and strength increase as the specimen size is decreased, a phenomenon that many researchers have related to dislocation motion in the materials.

In the description of the polycrystalline material as a continuum, geometrically necessary dislocation and disclination defects lead to incompatibilities resulting in internal stresses that are described by higher order spatial gradients of the deformation which are not always easy to deploy numerically into finite element codes. Traditionally, there have been several approaches to handle the numerical formulation of models including higher-order gradient of fields and/or of internal variables. Such an implementation can differ significantly depending on the gradient model type (Laplacian of an internal variable, first and/or second-order

spatial gradient of internal variable or field, *curl* of internal variable or field, etc.). Vector elements method can be used in the numerical implementation of *curl*-based plasticity model. These types of elements were originally introduced to solve Maxwells equations (see the work of Ndlec [160] and Jin [146] for more insights) to interpolate the magnetic field. The interpolated field of such elements is characteristically divergence-free, i.e., its *curl* is non zero. The vector field element method has been transferred into computational plasticity to interpolate the plastic part of the deformation gradient for a three-dimensional version of a plasticity model including elastic curvature, see Regueiro et al. [167]. Let mention that other methods were reported in the literature to solve *curl* related type equations using the Stokes-Helmholtz decomposition. Similar methods based on finite element analysis and spectral Fast Fourrier Transform are reported by Roy and Acharya [166, 169], respectively. An extensive report on the vector finite element method can be consulted in Regueiro et al. [167].

As a first order approximation, the *curl* of the inelastic velocity gradient is often used to represent the geometrically necessary dislocations and the *curl* of this the disclination density in large deformation theory with multiplicative decomposition of the deformation gradient. In this work we present the distribution of geometrically necessary dislocation and disclination densities as described by the *curl* and the *curl* of the *curl* of the plastic part of the velocity gradient for many classical micromechanical benchmark problems. While a formal inclusion of calculating the *curl* within this model will be implemented into finite element codes, useful information can be got by using elasticity solutions of far field stress applied to the boundary of a body containing defects as voids, cracks, disclinationd, and dislocations. Since at any instant the direction of impending plastic flow depends only upon the current stress state and the current state of the material, these solutions are viewed as "snapshots" at an instant in time of an evolving process. This "snapshots" method was also used by Yong-Shin and Dawson [176] in modeling void growth in visco-plastic materials for applications in metal forming processes and molecular dynamics simulations of a material behavior at small length scales.

We calculate the plastic part of the velocity gradient using an existing strain rate and temperature dependent dislocation based plasticity model, the evolving microstructural model for inelasticity, so-called EMMI model and outlined in Marin et al. [153]. The EMMI model uses a hyperbolic sine dependence upon the second invariant of the deviatoric stress to describe the symmetric part of the plastic part of the velocity gradient. The skew symmetric portion of the inelastic velocity gradient (plastic spin) is described in terms of the skew-symmetric tensor product of the plastic flow and a second order structure tensor that is the second order truncation of the orientation distribution function (ODF), which are introduced to represent the directional dislocation slip on the active slip systems. Using ODFs to describe plastic anisotropy has been previously explored by other authors. The details of the approach and examples of the predictive capability of the current model is described in Ning and Aifantis [161]. The plastic part of the velocity gradient is calculated using MATHEMATICA © from this stress field and is explored for various states of the material in terms of assumed values of the internal state variable, including the structure tensor. The full field state of inelastic flow is then calculated at that instant and the spatial dependence of the GNDs (*curl* of plastic velocity gradient) and the geometrically necessary disclination are determined.

The chapter is structured as follows.

1. Sections 2, 3 and 4 describe the main elements of the constitutive relations of the modified EMMI model to include anisotropy. In the EMMI model the material anisotropy is modeled using a second order orientation tensor and incorporated in the flow rule via a scalar variable describing the coaxiality between the second order orientation tensor and the direction of plastic deformation. The representation of material anisotropy using a second order orientation tensor allows for evolution of anisotropy independently of the kinematics hardening. In the modified model the skew symmetric portion of the plastic part of the velocity gradient (plastic spin) is a function of the plastic stretching and a second order structure tensor resulting from the truncation of the ODF for dislocations on multiple slip systems in crystal plasticity that has been used in the description of the material texture. The closure properties of this truncation yield an equation describing the evolution of the structure tensor.

2. In Section 5 we present an approximated continuum modeling of dislocation and disclination densities as tensor variables.

3. Next, Section 6 presents the solutions of benchmark micromechanical problems including a plate with a hole, the geometry of the hole varying from circular to ellipsoidal, subjected to uniaxial loading conditions. The numerical calculations were performed using MATHEMATICA.

4. Finally, Section 7 discusses the results got along with potential avenues for further improvements of the EMMI model accounting for void nucleation effects.

4.2 The original EMMI model

The constitutive model used in this study is the Evolving Micro-structural Model of Inelasticity (EMMI) outlined in Marin et al. [153]. It consists of the following elements.

4.2.1 Kinematics

The model equations are derived in the intermediate configuration which results from the multiplicative split of the deformation gradient as presented in Lee [152] and Lee and Liu [151]. The deformation gradient ($\mathbf{F}$) is given by:

$$\mathbf{F} = \mathbf{F}_e \mathbf{F}_\mathrm{p} \tag{4.1}$$

where $\mathbf{F}_\mathrm{p}$ is the plastic part of the total deformation gradient that facilitates mapping relevant variables from the reference material configuration to the intermediate. Similarly, $\mathbf{F}_e$ is the elastic part of the total deformation gradient that aids in mapping relevant variables from the intermediate configuration to the current. The intermediate configuration is a load-free configuration associated

with permanent deformation due to internal defects while the current configuration represents a material configuration with an applied load. An illustration of the multiplicative deformation gradient into its elastic and inelastic parts is presented in Fig.(4.1). Following the thermodynamics for materials with internal

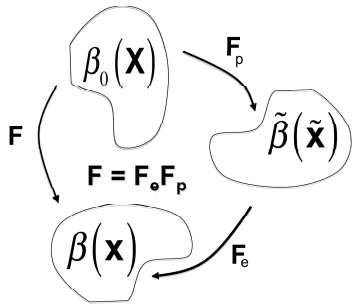

Figure 4.1: Finite strain decomposition of the deformation gradient $F = F_e F_p$

state variables presented by Coleman and Noll [136] and Coleman et al. [135], the model equations are derived in a compatible load free intermediate configuration and then pushed forward to the current configuration. The velocity gradient determined using Eq.(4.1) is:

$$\mathbf{l} = \dot{\mathbf{F}}\mathbf{F}^{-1}. \tag{4.2}$$

The symmetric and skew symmetric portions of the velocity gradient are therefore:

$$\mathbf{d} = \frac{1}{2}\left[\mathbf{l} + \mathbf{l}^{\mathrm{T}}\right], \qquad \mathbf{w} = \frac{1}{2}\left[\mathbf{l} - \mathbf{l}^{\mathrm{T}}\right]. \tag{4.3}$$

Both portions of the velocity gradient can further be decomposed into elastic and plastic parts such that:

$$\mathbf{d} = \mathbf{d}_e + \mathbf{d}_p, \qquad \mathbf{w} = \mathbf{w}_e + \mathbf{w}_p. \tag{4.4}$$

In addition, the velocity gradient in the current configuration is written as

$$\mathbf{l} = \dot{\mathbf{F}}\mathbf{F}^{-1} = \dot{\mathbf{F}}_e\mathbf{F}_e^{-1} + \mathbf{F}_e\dot{\mathbf{F}}_p\mathbf{F}_p^{-1}\mathbf{F}_e^{-1} \tag{4.5}$$

where the plastic velocity gradient in the intermediate configuration is defined by

$$\mathbf{L}_p = \dot{\mathbf{F}}_p\mathbf{F}_p^{-1}. \tag{4.6}$$

Eq.(4.6) will be useful to define the dislocation and disclination densities' tensors in the subsequent.

The velocity gradient in the intermediate configuration is given by

$$\mathbf{L} = \mathbf{F}_e^{-1} \mathrm{l} \mathbf{F}_e = \mathbf{F}_e^{-1} \dot{\mathbf{F}}_e + \dot{\mathbf{F}}_p \dot{\mathbf{F}}_{p^{-1}} = \mathbf{L}_e + \mathbf{L}_p \tag{4.7}$$

where the elastic velocity gradient in the intermediate configuration reads $\mathbf{F}_e^{-1}\dot{\mathbf{F}}_e$. Therefore, the velocity gradients in the current configuration are written in terms of the velocity gradients in the intermediate configuration as

$$\mathrm{l} = \mathbf{F}_e \mathbf{L} \mathbf{F}_e^{-1};\ \mathrm{l}_e = \mathbf{F}_e \mathbf{L}_e \mathbf{F}_e^{-1};\ \mathrm{l}_p = \mathbf{F}_e \mathbf{L}_p \mathbf{F}_e^{-1}. \tag{4.8}$$

The velocity gradient may be additively decomposed into the deformation tensor $\mathbf{d}$ and spin tensor $\mathbf{w}$ in the current configuration as follows:

$$\mathrm{l} = \mathbf{d} + \mathbf{w}. \tag{4.9}$$

Furthermore, the plastic deformation rate tensor $\mathbf{d}_p$ and plastic spin tensor $\mathbf{w}_p$ can be written in terms of their intermediate configuration counterparts as

$$\mathbf{d}_p = \mathrm{sym}(\mathrm{l}_p) = \mathrm{sym}\left(\mathbf{F}_e \mathbf{L}_p \mathbf{F}_e^{-1}\right), \qquad \mathbf{w}_p = \mathrm{skew}(\mathrm{l}_p) = \mathrm{skew}\left(\mathbf{F}_e \mathbf{L}_p \mathbf{F}_e^{-1}\right) \tag{4.10}$$

4.2.2 Internal State Variables Evolution Laws

With the assumption of linear elasticity, given a homogeneous isotropic material the Cauchy stress rate is:

$$\mathring{\boldsymbol{\sigma}} = \dot{\sigma} - \mathbf{w}_e \boldsymbol{\sigma} + \boldsymbol{\sigma} \mathbf{w}_e = \frac{\boldsymbol{\sigma}}{\mu(T)} \frac{d\mu(T)}{dT} \dot{T} + 2\mu(T)\, \acute{\mathbf{d}}_e + \lambda(T)\, \mathrm{tr}(\mathbf{d}_e)\mathbf{I} \tag{4.11}$$

where $\mu(T)$ and $\lambda(T)$ are the temperature dependent Lame coefficients; $\acute{\mathbf{d}}_e$ is the deviatoric part of the symmetric portion of the velocity gradient that is determined by:

$$\acute{\mathbf{d}}_e = \acute{\mathbf{d}} - \mathbf{d}_p. \tag{4.12}$$

Isotropic Hardening The isotropic hardening internal state variable is associated with the annihilation and generation of statistically stored dislocations (SSD) where its evolution equation is cast in a hardening minus recovery format. The dynamic recovery portion was introduced by Kocks and Mecking [148] and Estrin and Mecking [141], while the static recovery portion was presented by Nes [159]. The evolution equation is given by:

$$\dot{\kappa} = [(1 - C_\kappa)H(T) + C_\kappa H(T)\eta - R_d \kappa]\, \dot{\bar{\epsilon}}_p - R_s \kappa \sinh\left[\frac{Q_s}{2\mu c_\kappa}\kappa\right] \tag{4.13}$$

where $R_d(T)$ is the dynamic recovery parameter, $R_s(T)$ is the static recovery parameter, Q_s determines the order of the static recovery, C_κ and c_κ are isotropic hardening constants, and $H(T)$ is a temperature dependent isotropic hardening constant. The isotropic hardening parameter η is the scalar coaxiality term defined as in Eq.(4.23). The isotropic hardening modulus H_κ is reduced to a single variable given by:

$$H_\kappa = 2\mu(T)\, C_\kappa H(T) \tag{4.14}$$

Kinematic Hardening The back-stress is a stress-like internal state variable associated with the annihilation and generation of geometrically necessary dislocations. In a similar approach, the evolution equation for the back-stress $\boldsymbol{\alpha}$ is cast in a hardening minus recovery format given by:

$$\mathring{\boldsymbol{\alpha}} = \dot{\boldsymbol{\alpha}} - \mathbf{w}_e\boldsymbol{\alpha} + \boldsymbol{\alpha}\mathbf{w}_e = \left[h(T)e^{(C_a(1-\eta)}\right]\mathbf{d}_p - r_d\dot{\bar{\epsilon}}^p\sqrt{\frac{2}{3}}\,\|\boldsymbol{\alpha}\|\,\boldsymbol{\alpha} \tag{4.15}$$

$r_d(T)$ is the recovery parameter, C_a, $h(T)$ are the kinematic hardening modulii.

4.2.3 Plastic Flow

The plastic flow rule is given by:

$$\dot{\bar{\epsilon}}_p = f(T)\sinh\left[\frac{\sigma_{eq}}{\kappa + Y_0} - 1\right]^{n(T)} \tag{4.16}$$

where $n(T)$ and $f(T)$ are temperature dependent constants associated with the rate sensitivity of the material, Y_0 is the initial yield stress of the material, and T is the temperature variable. κ and $\boldsymbol{\alpha}$ are internal state variables associated with annihilation and generation of SSDs and GNDs, respectively. The equivalent stress is given by:

$$\sigma_{eq} = \sqrt{\frac{3}{2}\,\|\boldsymbol{\xi}\|} \tag{4.17}$$

where $\boldsymbol{\xi}$ is:

$$\boldsymbol{\xi} = \acute{\boldsymbol{\sigma}} - \frac{2}{3}\boldsymbol{\alpha} \tag{4.18}$$

and $\acute{\boldsymbol{\sigma}}$ is the deviatoric portion of the Cauchy stress.

A modification of the original EMMI model to account for the evolution of recrystallization and grain growth can be suggested. This proposal shall involve internal state variables representing dislocation density tensor and the spacing between geometrically necessary sub-grain boundaries. To describe both single and multiple peak recrystallizations, the model will enable tracking of the evolution of recrystallized volume fraction. These suggestions were included and validated in an old version of the original EMMI model, so-called the Bammann-Chiesa-Johnson (BCJ) model, see for instance Bammann et al. [129]. The validations of the extented BCJ model to include recrystallization are reported in the works of Brown and Bammann [133] and can serve as baseline for a modified EMMI model that account for recrystallization effects.

4.3 Anisotropy law

The evolution of anisotropy is represented by a second order orientation tensor outlined by Advani et al. [125, 126] and applied to polycrystalline materials by Prantil et al. [165], in which the orientation tensor is defined by the orientation distribution function of a unit vector bisecting two active slip systems. The rate of change of material anisotropy is captured using the orientation tensor given by:

$$\mathring{\mathbf{A}} = \dot{\mathbf{A}} - \mathbf{w}_e\mathbf{A} + \mathbf{A}\mathbf{w}_e = \lambda_g\left(\mathbf{A}\mathbf{d}_p + \mathbf{d}_p\mathbf{A} + \mathbf{d}_p\right) - 2\lambda_g\left[\mathbf{B} : \mathbf{d}_p\right] \tag{4.19}$$

where λ_g is a fitted parameter associated with the orientation of active slip systems and $\mathbf{B}$ is a fourth order orientation tensor. The parameter λ_g is associated with the fibers or particles shape and can be determined by microstructure characterization of the materials. A closure approximation is required to reduce the fourth order orientation tensor to a function of the second order orientation tensor while maintaining all required symmetries of the higher order tensor. Linear and quadratic closure approximations are two commonly used closure approximations in which Advani et al. [125, 126] showed that the linear closure approximation is exact for completely random orientations and the quadratic closure approximation is exact for highly aligned orientations. To maintain a higher degree of accuracy through all orientations, they recommended a hybrid closure approximation that is a linear combination of the linear and quadratic closure approximations using a scalar measure of orientation. The contraction operation $\mathbf{B} : \mathbf{d}_p$ is given by:

$$\mathbf{B} : \mathbf{d}_p = \frac{1}{7}\left[1 - f_A\right]\left[(\mathbf{A} : \mathbf{d}_p)\mathbf{I} + 2\mathbf{A}\mathbf{d}_p + 2\mathbf{d}_p\mathbf{A}\right] + \frac{2}{35}\left[f_A - 1\right]\mathbf{d}_p + f_A\left[\mathbf{A} : \mathbf{d}_p\right]\mathbf{A} \tag{4.20}$$

where f_A is a scalar measure of orientation given by:

$$f_A = \frac{3}{2}\mathbf{A} : \mathbf{A}^T - \frac{1}{2}. \tag{4.21}$$

Evolving anisotropy is incorporated into the flow-rule through a scalar coaxiality term used to describe the degree of alignment between the direction of plastic flow and anisotropy. A simple formulation yields

$$\eta(\phi) = \cos(\phi), \tag{4.22}$$

while a more refined one is given by:

$$\eta(\phi) = C_1\cos(\phi) + C_2\cos(2\phi) + C_3\cos(3\phi) + C_4\cos(4\phi) \tag{4.23}$$

where C_1, C_2, C_3 and C_4 are fitted anisotropic parameters. In Eqs.(4.22,4.23) the variable ϕ is defined by:

$$\phi = \cos^{-1}\left[\frac{\acute{\mathbf{A}}}{\left\|\acute{\mathbf{A}}\right\|} : \frac{\mathbf{d}_p}{\|\mathbf{d}_p\|}\right] \tag{4.24}$$

where $\acute{\mathbf{A}}$ is the deviatoric portion of the orientation tensor. The form of the coaxiality term is extended from the work presented by Lubarda and Krajcinovic [155] where they solved for the ODF equation by expanding the dot product of various damage orientation tensors with random direction tensors. This technique was later applied to polycrystalline materials by Marin et al. [128]. Similar forms of ϕ were presented in the works of Wegener and Schlegel [175], Bammann et al. [129], and Miller et al. [130], and François [143] where ϕ was defined using the direction of the back-stress and the plastic flow. The anisotropic parameters must sum up to unity, that is:

$$\sum_{n=1}^{4} C_i = 1, \tag{4.25}$$

this ensures that $\eta = 1$ when the direction of plastic flow is coaxial with the direction of developed anisotropy. The symmetric portion of the velocity gradient is given by:

$$\mathbf{d}_p = \sqrt{\frac{2}{3}}\dot{\bar{\epsilon}}_p \mathbf{N} \tag{4.26}$$

where $\mathbf{n}_p$ is the modified direction of plastic flow. $\dot{\bar{\epsilon}}_p$ is the equivalent plastic strain rate modified to account for anisotropic behavior proposed by Marin et al. [128] given by:

$$\dot{\bar{\epsilon}}_p = f(T)\sinh\left[\frac{\sigma_{eq}}{\eta(\phi)\kappa + Y_0} - 1\right]^{n(T)} \tag{4.27}$$

where $n(T)$ and $f(T)$ are constants associated with the rate sensitivity of the material, $\eta(\phi)$ is the scalar coaxiality term and Y_0 is the initial yield stress of the material, and T is the temperature variable. κ and $\boldsymbol{\alpha}$ are the isotropic and kinematic internal state variables, respectively. The equivalent stress is given by:

$$\sigma_{eq} = \sqrt{\frac{3}{2}\|\xi\|} \tag{4.28}$$

where ξ is:

$$\xi = \acute{\sigma} - \frac{2}{3}\boldsymbol{\alpha} \tag{4.29}$$

and $\acute{\sigma}$ is the deviatoric portion of the Cauchy stress. The modified direction of plastic flow must account for the directional effects of material anisotropy and is therefore given by:

$$\mathbf{N} = \frac{\mathbf{n}_T}{\|\mathbf{n}_T\|} \tag{4.30}$$

where $\mathbf{n}_T$ is defined as:

$$\mathbf{n}_T = \mathbf{n}_{\boldsymbol{\sigma}} - C_{\sigma\eta}\mathbf{n}_A \tag{4.31}$$

where $\mathbf{n}_{\boldsymbol{\sigma}}$ is the direction of the equivalent stress given by:

$$\mathbf{n}_\sigma = \frac{\xi}{\|\xi\|}. \tag{4.32}$$

The scalar $C_{\sigma\eta}$ is the ratio given by:

$$C_{\sigma\eta} = \frac{\sigma_{eq}}{\eta(\phi)}. \tag{4.33}$$

The direction of plastic flow imposed by the anisotropy $\mathbf{n}_A$ is given by:

$$\mathbf{n}_A = \zeta(\phi)\left(\acute{\mathbf{A}} - C_{\xi\mathbf{A}}\frac{\xi}{\|\xi\|}\right) \tag{4.34}$$

where the scalar $\zeta(\phi)$ is given by:

$$\zeta(\phi) = m\left[C_1 + 4C_2\cos(\phi) + 3C_3\left(4\cos(\phi)^2 - 1\right)\right] + m\left[16C_4\cos(\phi)\left(2\cos(\phi)^2 - 1\right)\right] \tag{4.35}$$

where m is difined by:

$$m = \left[\|\xi\| \left\| \acute{\mathbf{A}} \right\| \right]^{-1}. \tag{4.36}$$

The scalar $C_{\xi \mathbf{A}}$ is given by:

$$C_{\xi \mathbf{A}} = \frac{\xi : \acute{\mathbf{A}}}{\|\xi\|}. \tag{4.37}$$

The plastic part of the skew symmetric portion of the velocity gradient which follows from a constitutive definition presented by Prantil [165] is defined as:

$$\mathbf{w}^p = \frac{1}{\lambda_g} \left(\acute{\mathbf{A}} \mathbf{d}_p - \mathbf{d}_p \acute{\mathbf{A}} \right) \tag{4.38}$$

where λ_g is a fitted constant associated with the angle between active slip systems. Bammann and Aifantis [132] proposed a similar form of the plastic spin based on the micromechanics of single slip. Other forms were proposed by Dafalias [137] using representation theorem.

4.4 Dislocation and disclination modeling

4.4.1 Overview

The classical continuum theory of dislocation systems dates back to Kroner [149]. This theory describes the dislocation system as a function of a second-order tensor eld which is dened as the *curl* of the plastic distortion, see, for instance, deWit [138]. Later, the framework of the multiplicative decomposition of the deformation gradient was introduced to model dislocations' effects in metals under large deformations. An important feature of the multiplicative decomposition of the deformation gradient is that, while $\mathbf{F}$ is compatible, $\mathbf{F}_e$ and $\mathbf{F}_p$ are incompatible; this property is related to the formation of dislocations and disclinations defects in the material. When the strain becomes large enough, geometrical necessary dislocations, geometrically necessary boundaries, and geometrically necessary disclinations are accounted for as an energetically favorable alternative to the formation of several types of defects including gaps, overlaps and holes. In the material's description as a continuum eld, the GNDs and geometrically necessary disclinations lead to incompatibilities resulting in internal stresses that can be modeled by higher order spatial gradients of the deformation. Hence, the resulting models of the polycrystalline material include natural, physical length scales.

Other types of modeling continuum media including dislocation and disclination defects exist, especially in small strain formulation. Eringen and Clauss [140] solved the elasticity problem of internal stresses in a micropolar body containing both dislocations and disclinations. The disclination density tensor in this formulation results from the non-vanishing of the RiemannChristoffel curvature tensor; in the small strain theory Eringen and Claus represented the disclination tensor density by the *curl* of the curvature (which is the gradient of the extra rotational DOF in the micropolar theory). In other crystal plasticity theories, the disclination density tensor becomes another state variable with a conjugate internal stress. The balance of angular and linear momentum in the theory of Eringen and Claus

are the meso-scale momentum balance laws for the meso-scale internal stresses and moments. This results in an additional backs-tress on the slip system and the fact that internal stresses are self equilibrated at the meso-scale level, leaving the macroscopic momentum balance laws unchanged and the Cauchy stress symmetric. Some recent theories introduced an additional length scale to be determined from experimental data, atomistic or micromechanical simulations. This can easily be extended to nite deformation, but the multi-length scale concept is unchanged. While this approach will require a reformulation of some numerical schemes, it may be necessary for certain problems.

4.4.2 The Model

. Failure in crystals starts when misorientation at a point in the continuum become too large to support further rotation. In a continuum modeling of damage in the crystals this is described by geometrically necessary dislocation densities and disclination densities. deWit [138] proposed a theory to model dislocations and disclinations density tensors based on small deformations hypothesis. In deWit's proposal, the dislocation density tensor is the *curl* of the plastic distortion which includes a contribution from the usual plastic strain and a plastic rotation; the disclination density tensor is modeled by the *curl* of the plastic-bend twist, the plastic bend-twist being described itself as the *curl* of the plastic distortion, see Fig.(4.2). In this work, we propose to extend deWit's suggestion to the case of

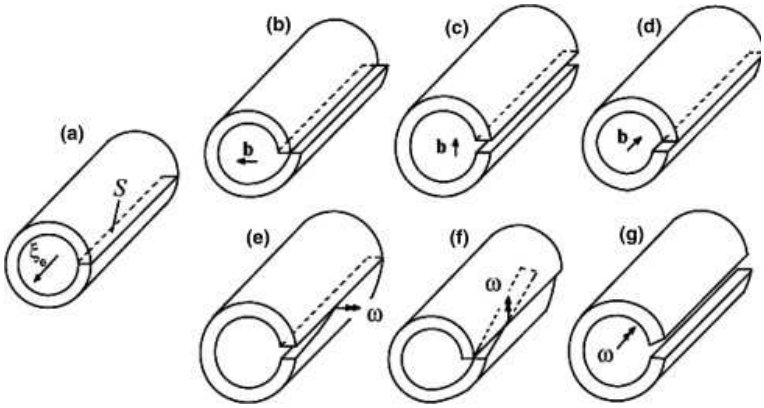

Figure 4.2: Volterra's defects: (a) reference cylinder with defect line ξ_0 and cut surface S; (b,c) edge dislocations and (d) screw dislocation with Burgers vector $\mathbf{b}$; (e,f) twist disclinations and (g) wedge disclination with Frank vector $\mathbf{w}$, Clayton et al. [134]

finite strains with multiplicative decomposition of the deformation gradient theory. In our proposal, the plastic distortion tensor is represented by the plastic part of the velocity gradient, the bend-twist variable the *curl* of the plastic part of the velocity gradient. The *curl* of the plastic part of the velocity gradient is used to represent the geometrically necessary dislocations density tensor and the *curl* of this the disclination density tensor. With these assumptions, we get

$$\begin{cases} \boldsymbol{\theta} & \equiv & \nabla \times (\nabla \times \mathbf{l}_{\mathrm{p}}) \\ \boldsymbol{\beta} & \equiv & \nabla \times \mathbf{l}_{\mathrm{p}} \\ \mathbf{l}_{\mathrm{p}} & \equiv & \mathbf{d}_{\mathrm{p}} + \mathbf{w}_{\mathrm{p}} \end{cases} \tag{4.39}$$

These two approximations will be sufficient since the main aim of this study is to demonstrate that material texture orientation plays a key role in the damage of polycrystalline materials and should be accounted for in constitutive damage models of polycrystals; such feature is missing many current damage models for these materials.

4.5 Problem definition and methodology

The aim of this section is to present analytical predictions of the distributions of the dislocation and disclination densities in a plate containing a circular, and then ellipsoidal hole and subjected to uniaxial tension loading conditions. To meet this aim, we use the spatial stress distributions solutions of these classical benchmark problems for the case where the plate material obeys a simple elasticity law; these problems are abundant in the literature, see Timoshenko [173], Inglis [145], and Kirch [150]. It is well known that a thin rectangular plate subjected to a uniaxial tension load yields a uniform stress distribution in the plate. Introducing a hole in the plate disturbs the uniform stress distribution near the hole, resulting in a significantly higher stress than the average stress in the plate, especially around the hole. The plate subjected to a compression loading can be analyzed as a 2-D plane strain elasticity problem. In theory, if the plate is infinite, then the stress near the hole is three times higher than the far field stress, as showed by the contour plot of the component "2,2" of the stress field in the plate in Figure 4.5. Figure 4.3 illustrate the two problem models under consideration, the first one on the left side, and the second one on the right side. A comprehensive review of

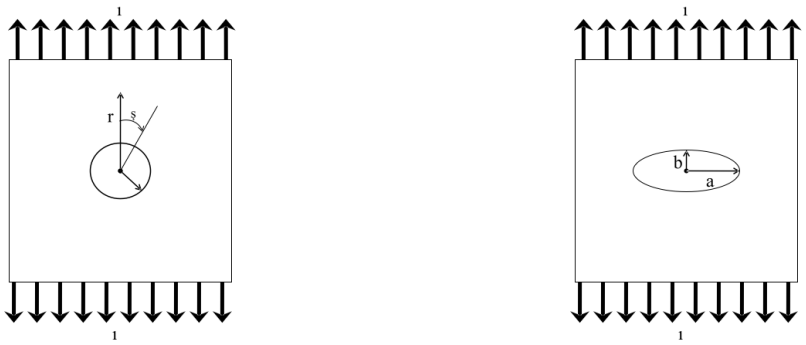

Figure 4.3: (Left)Circular hole in infinite plate. (Right) Elliptical hole in infinite plate.

the analytical solutions of the benchmark problems (involving elasticity behavior) used in this work can be found in the works of [173, 145, 150].

The constitutive relations of the EMMI model accounting for anisotropy effects have been incorporated into MATHEMATICA as a material point simulator to capture the texture of a rolled material. The EMMI model is used to compute each of the component of the structure tensor. Since at any instant the direction of impending plastic flow depends only upon the current stress state and the current state of the material, these solutions can be viewed as "snapshots" at an instant

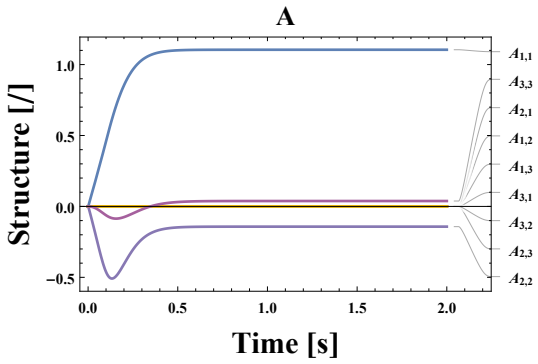

Figure 4.4: Evolution of the structure tensor ($\mathbf{A}$) as a function of the time showing the predicted texture of the material after 20% of deformation for the case of a plain strain compression test.

in time of an evolving process. We determine the structure tensor texture of the material after 20% of deformation, see Figure 4.4. Then, using the velocity gradient as a forcing function, we integrate all the constitutive differential equations of the model (stress rate, isotropic rate, kinematic rate and structure tensor rate) for the case of a plane strain compression.

The plastic part of the velocity gradient is calculated from this stress field and is analyzed for various states of the material in terms of assumed values of the internal state variable of the EMMI model, including the structure tensor. The full field state of inelastic flow is then calculated at that instant and the spatial dependence of the geometrically necessary dislocation (*curl* of plastic velocity gradient $\mathbf{l}_p = \mathbf{d}_p + \mathbf{w}_p$) and the disclination (*curl* of the *curl* of the plastic part of the velocity gradient) are determined.

Using the results predicted by the changed EMMI model for a thin flat plate containing a circular, then an ellipsoidal hole, with a constant distributed far field stress, the plastic flow and plastic spin are calculated assuming an initially isotropic texture. Then various inclination angles of the material texture regarding the horizontal are considered for the case where the hole in the plate is circular: $\gamma_i = [0°, 20°, 40°, 60°]$.

To simulate the reorientation of the texture of the material, we rotate the structure tensor using the following expression:

$$\mathbf{A}'(\gamma_i) = \mathbf{R}(\gamma_i)\,\mathbf{A}\,\mathbf{R}^t(\gamma_i) \tag{4.40}$$

4.6 Results and discussion

The solutions of various distributions for geometrically necessary dislocation and disclination density tensor components are presented in the figures appended to the paper for both the cases where the hole has a circular and elliptical shapes. Figure 4.6 displays the contour plots of the 1,1 component of the disclination density tensor distribution in the plate for different angles of orientation of the material texture (0, 20, 40, and 60°). We recall that these plots are based upon

a distributed far field stress that is applied at the top and bottom of a thin plate containing a circular hole, the hole simulating a crack in the plate material.

The major observation from these figures is that the change of the angle of orientation of the material texture in the plate affects the density of the disclination defects (per unit area for a specific zone) and their locations. This feature appears better in Figure 4.7 which represents the distribution of the "3,2" components of the disclination density tensor in the plate for the material texture oriented 60° regarding the horizontal line. Here, the disclination defects originate near the circular hole; the highest defects concentration is horizontally distributed in the plate, while the highest concentration of the disclination defects follows a direction 45° inclined with horizontal line of the plate when the texture orientation of the material is 0°. This inclination reduces when the material texture orientation varies from 0 to 60°. Similar features are observed for the distribution of the components "2,3" of the disclination density tensor. However, these effects are related to the lowest concentration of the disclination defects, the highest concentration being confined in small zones near the vicinity of the circular hole. The size of the highest concentration zone reduces when the orientation angle changes from 0 to 60°. The orientation angle for the material texture does not affect the distribution of the remaining components of the disclination density tensor since distribution of the disclination remains the same for any material texture orientation considered.

Figure 4.8 represent the distribution of the components of the dislocation density tensor for the case of the plate with a circular hole and is the analogous of Figure 4.6 for the disclination density tensor when the angle of orientation of the material texture changes from 0 to 60°. In these plots, the density of geometrically necessary dislocations are emitted from the corners, which is in good agreement with the dislocation theory. Figure 4.5 shows the stress triaxiality at each point

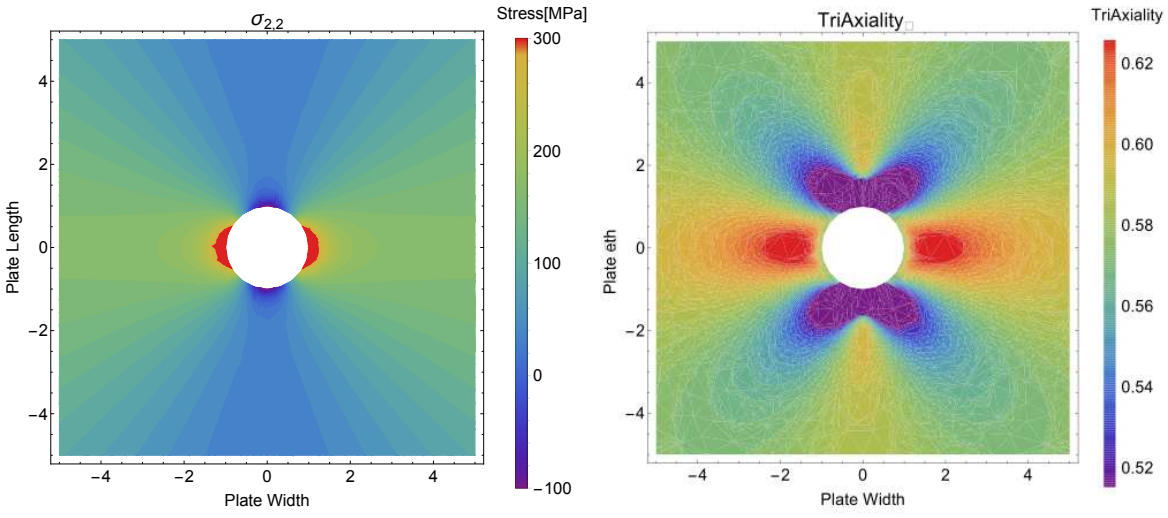

Figure 4.5: Cauchy stress for the case of the plate with circular hole. (Left) "2,2" component of the stress. (Right) stress triaxiality.

of the plate based on the EMMI model. This figure shows that the stress triaxiality distribution in the plate is not uniform; the magnitude of the concentrated

stress does not exceed the material's theoretical cohesive strength to yield fracture of the plate; however, it is enough to cause a mismatch of the material internal texture. Also, dislocations and/or disclinations defects nucleate in the polycrystalline material from the vicinity of the hole where the concentration of the stress is maximum as showed in Figure 4.5. This feature is universal and was observed in many numerical and experimental tests. Among these works, let us mention the works of Rice [168] which investigated dislocation emission from a crack tip based on Peierls-Nabarro model, [163, 158]. Rice suggested that a stressed slip plane from the crack tip developed; this allows some small slip displacement to occur near the tip as a response to small applied loading, and as the load increases, the emerging dislocation configuration becomes unstable and yields to form diclocation that is driven away from the crack. The experimental works of Ohr [162] have showed that the nucleation of a dislocation from a crack tip yields crack blunting and when the crack is blunted to a certain extent, the emission of dislocations from a crack tip can be interrupted. In addition, Figure 4.5 shows that the stress triaxiality concentration around the hole is independent of the material texture orientation, which affects, however, both the repartition of the disclination and dislocation defects around the hole.

The simulations for the plate with the elliptical hole are time consuming, the main reason being the complexity of the stress field for the solution of the elastic problem this geometry involves. We represent half of the contour plots in the plate even though the distribution of the dislocation and disclination densities in the plate is not symmetric because of the non-symmetric nature of the *curl* of the plastic part of velocity gradient and its *curl*.This approximation is reasonable in view of the aim of to this study.

Figure 4.9 displays the distribution of the disclination density tensor components in the plate with the elliptical hole, while Figure 4.10 presents that of the dislocation density tensor components for the same model problem. In the two cases, the densities of the dislocation and disclination defects tensor components are not uniform in the plate: the maximum density occurs around the hole, while this density remains homogeneous at the points in the plate that are near its upper and lower boundaries.

The figures also show that both the dislocation and disclination defects nucleate near the vertices of the elliptical hole. In addition, similar to the case of the plate with a circular hole, the distribution of the dislocation and disclination densities' tensors become homogeneous at locations of the plate far from the hole. The figures also demonstrate that the distribution of the dislocation and disclination densities expand in a direction perpendicular to the loading direction.

The correlation between the high density of the dislocation and disclination defects near the (ellipsoidal and circular) hole is expected since dislocation and disclination densities exhibit great effects on the strain and stress fields around the hole, as several previous independent studies have showed. Therefore, these defects must be accounted for in a refined modeling of the mechanisms that govern void nucleation, growth, and coalescence in polycrystalline materials.

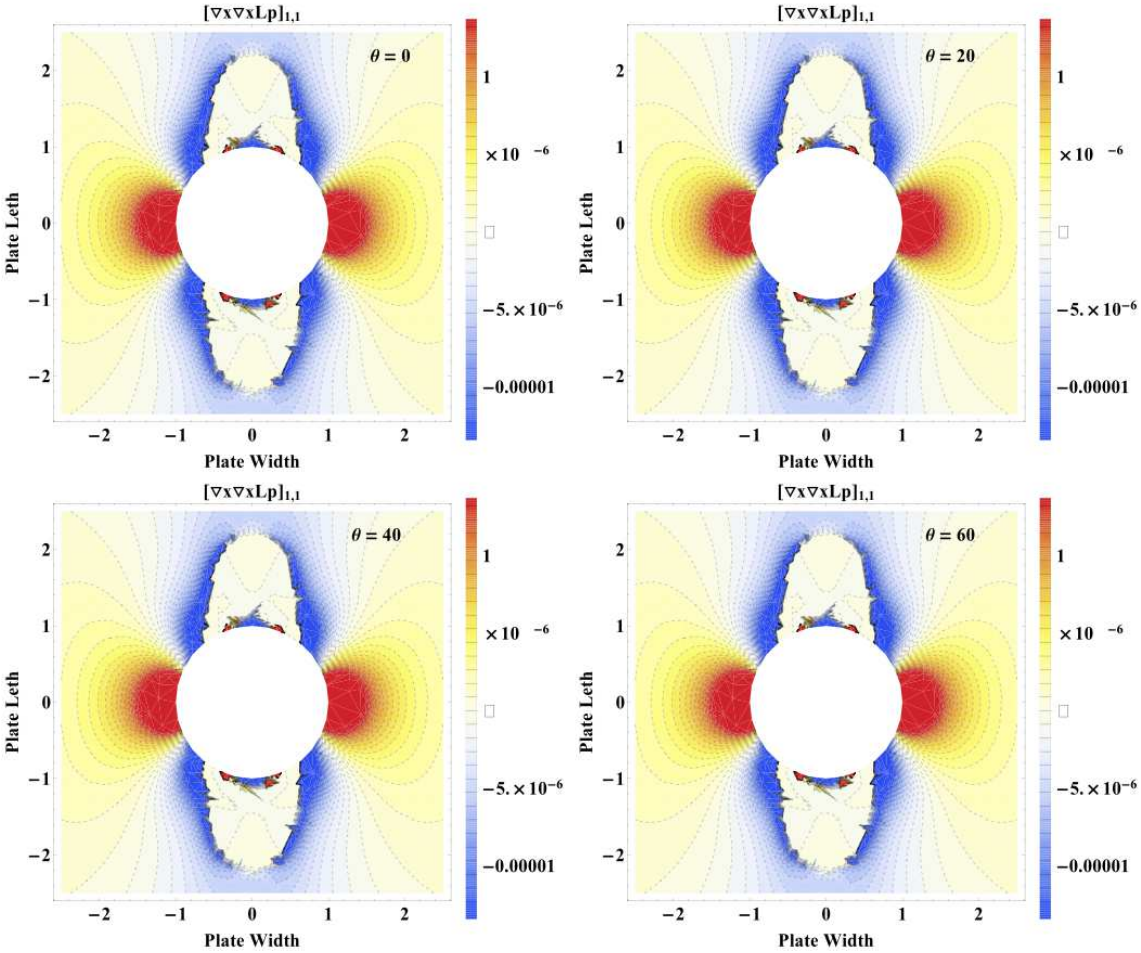

Figure 4.6: Distribution of the disclination density tensor component "1,1" in the plate for the case of the plate with a circular hole and different angles of orientation of the material texture: 0, 20, 40, and 60°

4.7 Conclusion

A representation of the dislocation and disclination incompatibility effects were introduced into an evolving micro-structural model for inelasticity by representing the geometrically necessary dislocations and disclinations as the *curl* of the plastic part of the velocity gradient and the *curl* of the *curl* of the plastic part of the velocity gradient. The proposed formulation was assessed based on classical elasticity solutions of some benchmark micromechanical problems: a plate containing a circular and an elliptical hole that is loaded in uniaxial tension and involving far field stress applied at the boundaries of the of plate. These solutions are used to predict the distribution of the GNDs and disclination densities and the stress distribution in the plate. The results got show that GNDs and disclination defects originate from the corners of the hole, which mirrors well results got form dislocation et disclination theories. The results also show that the stress triaxility distribution around the hole in the plate is not affected by the material texture orientation. This suggests that further explorations are needed to understand the role played by a combination of the stress triaxiality effects and the concentration

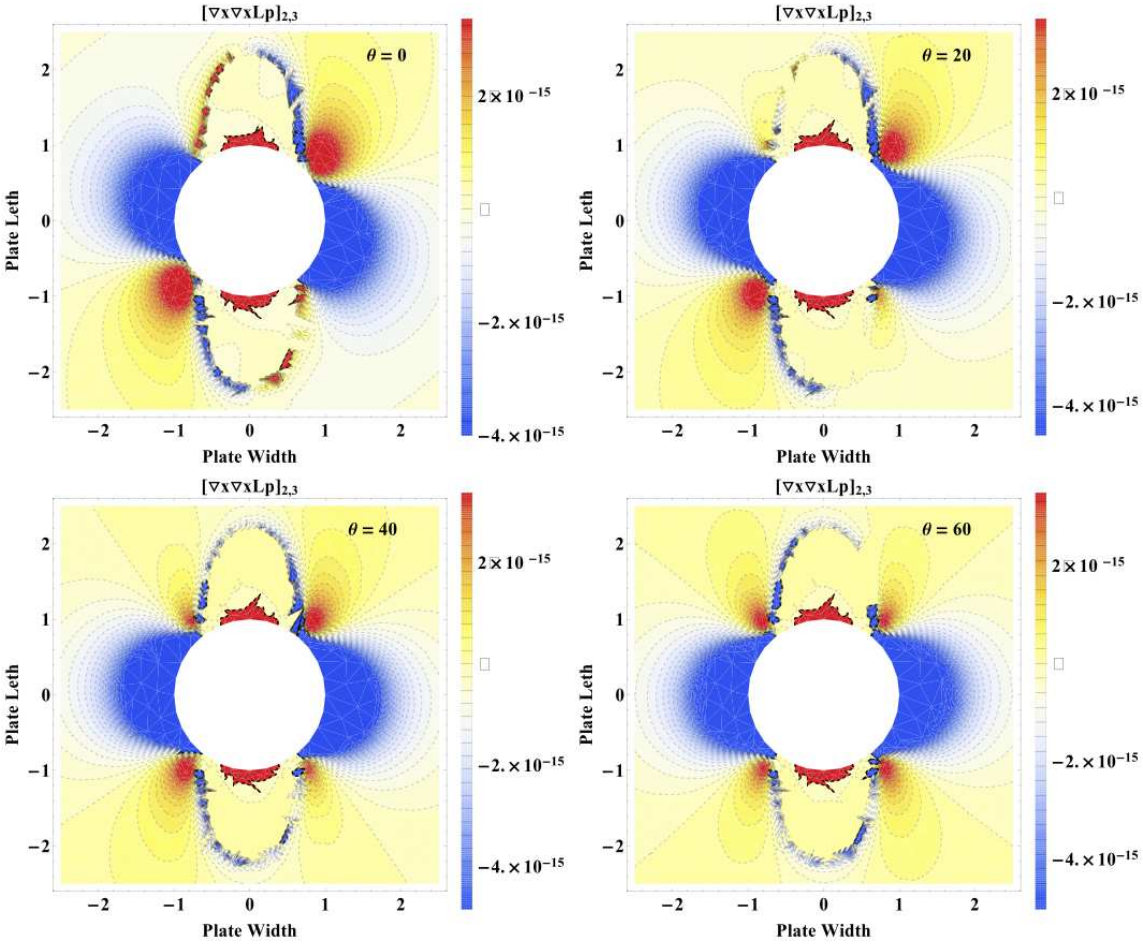

Figure 4.7: Distribution of the disclination density tensor component "2,3" in the plate for the case of the plate with a circular hole and different angles of orientation of the material texture: 0, 20, 40, and 60°

of dislocation and disclination defects on voids nucleation, growth and coalescence in polycrystalline materials for an accurate prediction of failure in such materials.

4.8 Research Project-Modeling Dislocations and Disclinations Effects at Finite Strain

The dislocation and disclination model I proposed along with A. Adedoyin and D. J. Bammann, two of my collaborators, was based on deWitt's proposal which we adopted in a finite deformation theory for inelasticity with no further justifications. Another more elaborated framework was developed by Bamman et al. to model crystalline metals including dislocations and disclinations defects. In Bammann et al.'s formulation the kinematics and balance laws are developed simulataneously at two scales of observations: at the macroscopic level a kinematics with a multiplicative decomposition of the deformation gradient and the meso-scale an additive decomposition of some affine connection into contributions from dislocations and disclinations defects. The standard angular momentum is enforced at the macroscopic level while at the meso-scale and "ad hoc" momentum

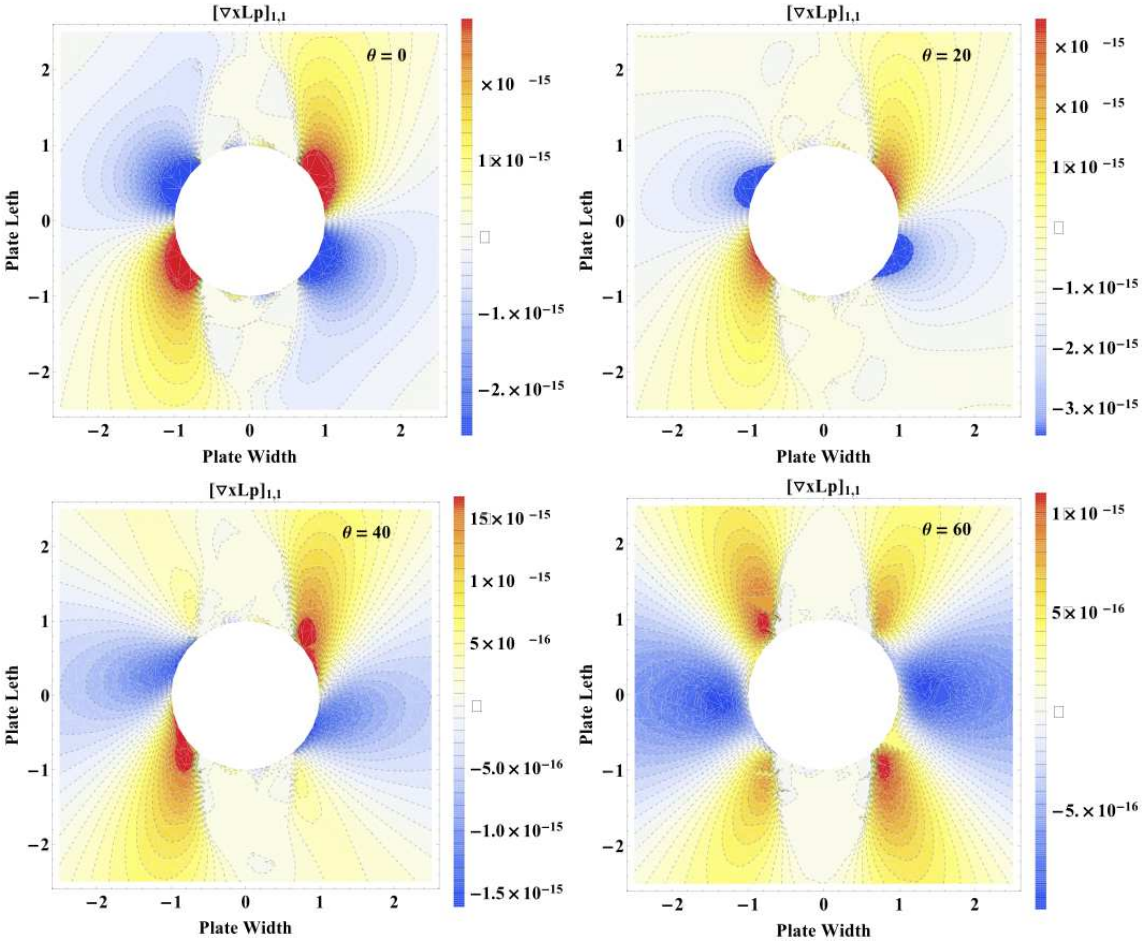

Figure 4.8: Distribution of the GNDs tensor component "1,1" for the case of the plate with a circular hole and different angles of orientation of the material texture: 0, 20, 40, and 60°

on the dislocations and disclinations densities are adopted.

My research proposal on this topic is rooted in Bamman et al. previous formulation. This proposal is to present the macroscopic formulation of a multi-scale finite plasticity model containing length scales due the presence of geometrically necessary dislocations and disclinations. The Coleman-Gurtin thermodynamics of ISVs motivated from the physics occurring at the meso-scale will be used. This approach will result in the development of an ISV finite micro-polar crystal plasticity model accounting for dislocations and disclinations and assuming a three-term multiplicative decomposition of the deformation gradient. A micro-polar term related to lattice defects rotation will also be introduced. The free energy will include a set of internal variables: elastic strains associated with statistically stored dislocations and disclinations, the disclination curvature tensor and the dislocation torsion tensor. The latter will be connected to spatial gradients, the *curl* of some components of the deformation gradient, introducing therefore two different length scales, to arrive at a dimensionally consistent strain measure. To complete the model, evolution equations for the ISVs will be provided.

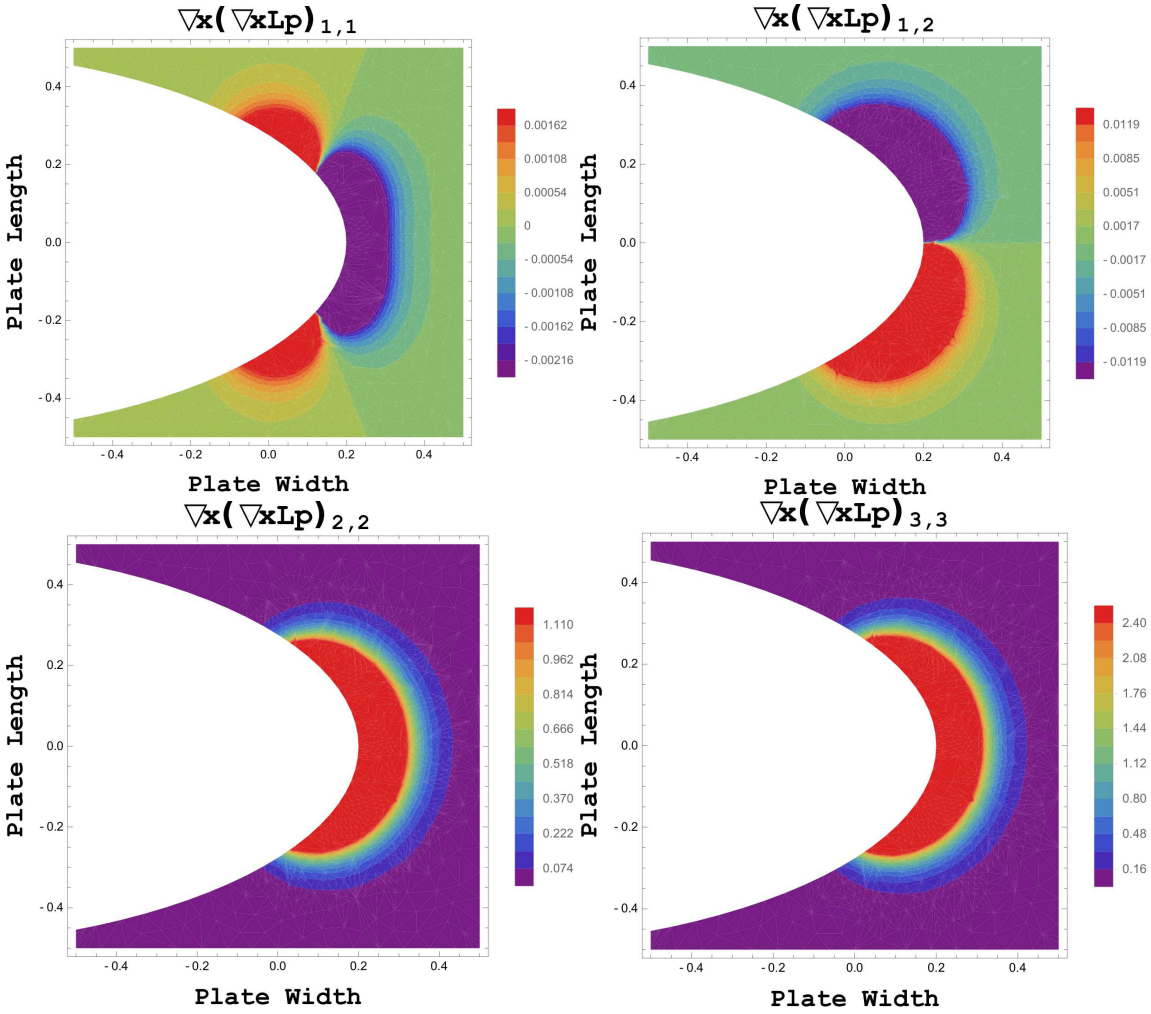

Figure 4.9: Distribution of the components of the disclination density tensor in the plate for the case of the plate with an elliptic hole.

The resulting micro-polar finite crystal plasticity model will require a special numerical implementation treatment because it involves the *curl* of some components of the deformation gradient, leading to a partial differential equation to solve for the plastic vector, rather than an ordinary differential equation for standard crystal plasticity models. Along with the linear momentum balance, this will lead to a coupled system of PDEs for which to solve numerically by a coupled finite element implementation, this is another challenge of our work. To address this challenge, I will use the vector elements method in the finite element formulation of the model. These types of elements were introduced to solve Maxwells equations to interpolate the magnetic field. The interpolated field of such elements is characteristically divergence-free, i.e. its curl is non zero. Douglas J. Bammann, my former posdoc mentor, has transferred the idea to plasticity, using the vector field element method to interpolate the plastic part of the deformation gradient for a 3-D version of the plasticity model with elastic curvature. I plan to leverage this experience in my numerical implementation of the proposed theory. I propose to

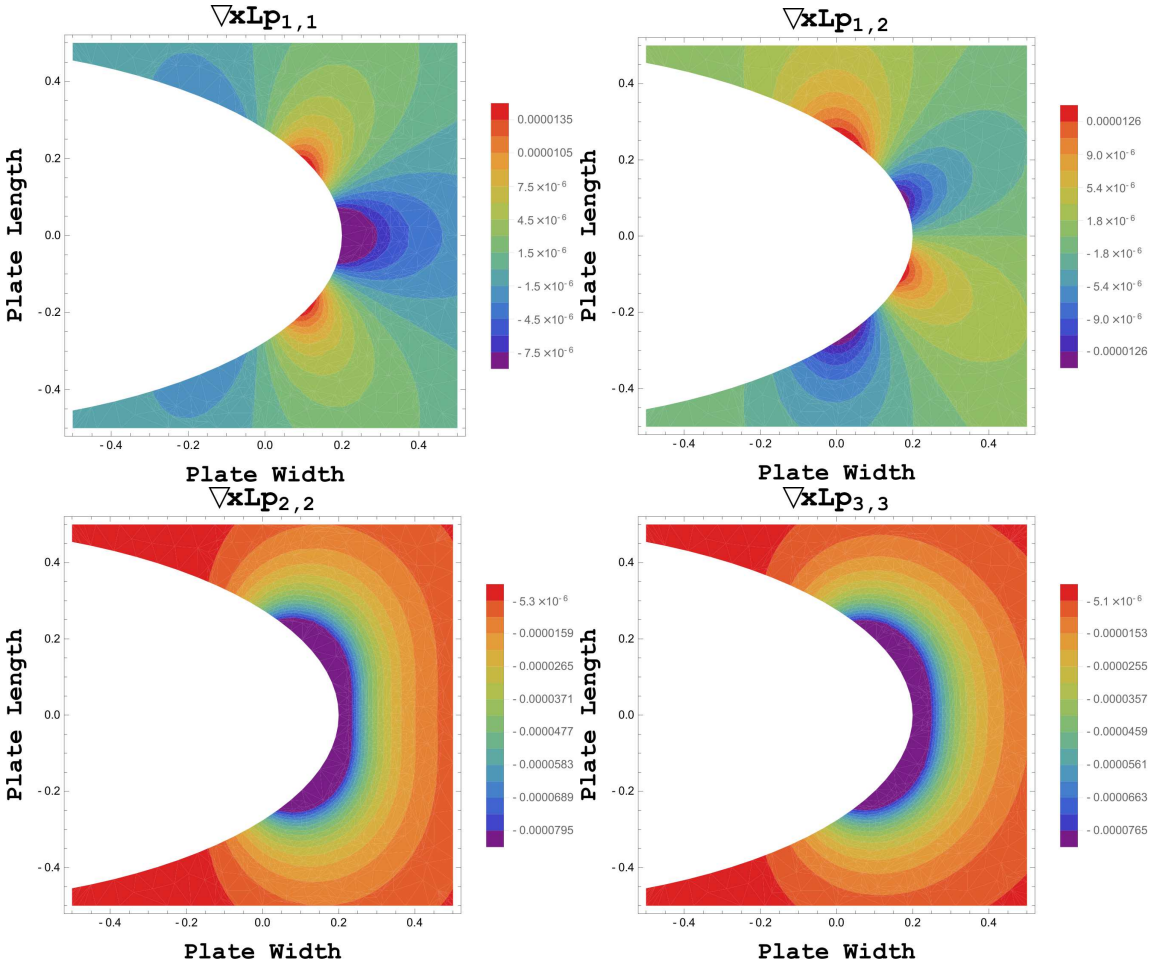

Figure 4.10: Distribution of the components of the dislocation density tensor in the plate for the case of the plate with an elliptic hole.

design new experimental techniques capable of identifying the underlying physical mechanism related to each length scale the model involved.

The proposed work will provide several contributions to material scientists and the mechanical engineering community. These contributions are summarized below:

- Robust computational physically based multi-length scale finite plasticity model containing dislocation and disclination defects.

- Physical mechanisms related to the length scales in the model.

Once the model is developed, boundary value problems at tiny length scales will be solved accurately in the cases outside the range of local continuum plasticity. Also, the solution of boundary value problems at the macroscopic scale will be mesh-independent. Such information is pertinent to current nanotechnology and structural engineering applications. If I am successful, the model will be extended to include damage and temperature effects.

The developed tool will be useful for the engineering community to investigate the plastic deformation of metals, especially in the post-bifurcation regime, and to solve boundary value problems at tiny length scales. Also, the underlying physical mechanisms behind length scales introduced in the model will be investigated through the design of challenging experiments. The work carried out on the physical mechanisms behind the length scales will be of high interest for the material science community. For the engineering community, a robust computational tool will be available to (i) investigate the post-bifurcation regime behavior, and (ii) accurately solve boundary value problems at tiny length scales. The end production of this project will include (i) presentations to national and international conferences, (ii) refereed papers, (iii) a framework and the corresponding modeling to link geometrically necessary dislocations and a macroscopic material model. Such a framework will be helpful for our mechanical engineering students to understand the role played by the geometrically necessary dislocations and the disclinations on the plastic deformation of metals.

Chapter 5

Modeling of ceramic matrix composites under extreme loadings

5.1 Introduction

Current challenges in aeronautical industries include the need to realize a reduction in fuel consumption and/or increases in the aircraft performance in extreme environments. Using high performance composite materials, such as ceramic matrix composites (CMCs), affords a means to meet these challenges. CMC materials have a lower density, offer an excellent resistance to thermo-mechanical fatigue loadings, and are valuable for gas turbine hot section components and hypersonic leading edge materials. CMC materials have a longer service life and make up an excellent alternative to metallic alloys in several aeronautical applications: combustion chambers, turbines shrouds, gas turbines, and nozzles where sharp temperature gradients are present.

To support the use of CMCs requires that analytic methods (i.e., material models) be developed to compute their thermal, mechanical, and coupled thermo-mechanical behavior/responses. These models include considerations pertaining to computing responses under extreme environments that induce severe thermal gradients and that must be able to capture degradation and failure of CMCs in such environments. Experimental approaches to understand CMC material inelastic behavior are very expensive. Also, the study of lower level systems failures resulting from extreme external conditions, such as those encountered for instance, during hypersonic flights, propulsion stages, for large scale complex systems is a primary research area that requires additional investigations. Alternatively, the use of validated predictive computational physics-based models which can describe accurately the different stages of CMCs behavior until failure are preferred. Such a predictive tool could enable the virtual study of structural behavior under extreme conditions and allows parametric studies to be performed to test opportunities to prevent and mitigate these issues. Current finite element (FE) models used to analyze structures composed of CMCs are often limited in scope to linear elastic regime which does not capture the strain and stress localization zones which are precursors of damage and fracture in a material under extreme thermo-mechanical loadings. Therefore, there is a need to develop a predictive tool that accounts for the progressive accumulation of such damage and assess whether the influence

this localized damage on the overall performance of the system within which it is a part which inevitably leads to material failure when the latter is subjected to extreme conditions.

The initiation of mechanical degradation in CMCs is attributed to the formation of various networks of matrix cracks; a hierarchy of such networks is presented in Forio and Lomon [178]. Several damage mechanisms could occur: matrix micro-cracking, fiber/matrix debonding, and fiber breakage. These mechanisms are strongly anisotropic: cracks could be normal to the loading direction or partly deviated by the reinforcement orientation. These cracks could be opened or closed depending on the loading and on the thermal residual stresses induced by cure processing. More precisely, under tensile loading, CMCs present a linear elastic response until the initiation and propagation of matrix micro-cracks and the partial re-opening of thermal cracks. These cracks mainly start at the singularity of macro-pores and propagate normally to the applied load direction. In a second stage, multiplication of matrix micro-cracks and the associated fiber/matrix debonding are propagating until matrix crack saturation, see [180]. Composites with a weak interface exhibit a "plateau-like behavior", see Naslain [181]. The matrix crack saturation is rapidly achieved (load transfer being poor) and the total failure occurred almost immediately after this saturation point. For composites that present high strain to rupture, after matrix saturation, a significant domain corresponding to a progressive load transfer to the fibers, which then fracture progressively, is observed, see El Bouazzaoui R. *et al.* [182]. Another set of cracks corresponding to multiple cracking of the bundle could occur, Bale *et al.* [183]. These composites present a broad non-linear domain and higher stresses with no plateau-like domain.

Several micro-mechanics analyses have been developed for predicting the onset and progression of failure within brittle composites, see Curtin [184], Lee and Daniel [185], Weitsman and Zhu [186], and Hedgepeth [187]. In what is now considered a classical analysis, Aveston *et al.* [188] discussed the "energetics of multiple fracture" in brittle composites, see Curtin [184]. This work has fueled similar studies for over several years. Many of the models presented over this time period are based upon the classical shear-lag formulation presented by Hedgepeth [187]. The approach parallels the method used by Cox [189] who first investigated the influence of a single short fiber embedded in an infinite medium, Carrere and Lamon [190], but can be adapted to investigate the response of unidirectional and cross-ply laminates if an equivalent damage state for the laminate can be determined. Unfortunately, this can be quite a difficult task. The complexities of brittle failure in composite materials have forced many researchers to rely on empirical data which has reduced the utility of the analytical models. In addition, many existing analytical solutions use failure criteria which over-predict the rate of matrix cracking. The most obvious case is the original ACK-model in which all the matrix cracks were assumed to form at a single applied stress, see Curtin [184]. This resulted in a "stepped" or "plateaued" stress-strain response where the material response curve is initially linear followed by a single large jump in strain during matrix failure then the response becomes linear again albeit with a smaller slope. Hence, even though the micro-mechanics approach is appealing because of its simplicity, solutions from many of the existing models do not mirror experimental data, see Weitsman and Zhu [186] and Evans *et al.*[191] and, there-

fore, alternate approaches are sought.

Within the literature, there are several more detailed analyses which avoid some simplifying assumptions used under the micro-mechanics approach, see Nairn [192] and Larson [193]. For example, several solutions use traditional fracture mechanics techniques to investigate the conditions for crack growth near a bi-material (fiber/matrix) interface, see Chawla [194] and Han *et al.* [195]. These models are useful since the development of valid design and failure criteria are contingent upon a full understanding of the micro-structural behavior of the laminate during loading. Unfortunately, modeling the behavior of an individual crack in this manner may require integration of many complex theories, e.g. linear elastic fracture mechanics, statistical analysis and variational mechanics; therefore, when considering the large number of cracks which are continuously developing and growing in a CMC, the analysis can be complex. To further compound the problem, the crack formation within the composite is dependent not only on the lamina properties but also on laminate and component geometries. In addition, matrix cracking is not the only damage mode observed in CMCs. Cracks can also develop within the fibers or along the fiber/matrix interface. Since the evolution of all these damages depends on the magnitude and type of loading, the operating environment must also be accounted for in the analysis. When considering all these effects, the problem quickly becomes overwhelming. Perhaps this explains why many first-order models have been reported in the literature, Pryce and Smith [196], Spearing and Zok[197], Ladeveze [198], and Ladeveze [199].

In addition, different macroscopic damage models based on the influence of the major microscopic mechanisms on the macroscopic behavior of the material were also proposed. In these models, the crack closing/opening phenomena can be accounted for by decomposing the tensile/compression elastic density energy, Ladeveze [200], Ladeveze [201], and Hild *et al.* [202].The crack micro-mechanisms of satin based CMCs manifest themselves at the macroscopic scale by some complex anisotropic damage. Each network of cracks induced a specific evolution law for the damage. Some models (for instance, Evans and Marshall [203]) were developed based on microscopic models. However, one difficulty lays in the damage's description for complex loadings or outside of the fibers axis, since the micro-models used only represent the behavior toward the fibers. In fact, one major modeling difficulty is to account for the complex cracks network because it is oriented by either the direction of the loading or that of the fibers. Models the kinematics of the damage of which is fixed by a referential related to the composite allows an easy description of the cracks networks oriented by the fibers, Camus [204], Gasser [205], Gasser *et al.* [206], and Gasser and Ladeveze [207], while models described in a referential related to the loading enable a better description of the whole network, Rouby and Reynaud [208].

Mechanical tests under cyclic loadings have evidenced a fatigue phenomenon which manifests itself by an evolution of the damage, a residual deformation and an evolution of the hysteresis loops of loading and unloading. An explanation of this phenomenon was given in Evans [209], Burr *et al.*, and [210] based on a ruin mechanism of the interfacial fibers/matrix debonding toward the fibers. These authors show that the fatigue damage of CMCs is partially driven by mechanical cycling. In addition, the ruin mechanism allows explaining the difference of the

fatigue behavior of some CMCs in the presence of temperature. A description of the ruin mechanism at the interface fibers/matrix was used in [211] to define a fatigue damage evolution law for a macroscopic model.

An outline for the development of a new form of CMC material model is described here. The intent is to obtain a formulation for a robust method for predicting the thermo-mechanical behaviors of these materials, particularly related to the cracking of the matrix (i.e., fracture responses) that might result in aerospace applications.

The CMC material model proposed relies on the classical modeling framework of the thermodynamics of irreversible processes with internal state variables, see for instance Letombe [213], Letombe [212], Baranger *et al.*[214], and Baranger *et al.* [215]. The different steps of the formulation are:

- selection of the state variables and of a potential (i.e., interpreting these variables is given by a potential form);
- computation of the associated thermo-dynamical forces by duality with state variables;
- computation of the state laws; and
- definition of the damage evolution laws and "ad hoc" failure criterion.

The proposed model formulation takes into account the crack networks and the associated fiber-matrix debonding through damage and inelastic strains. The inelastic part is relatively classical and the damage part is based on anisotropic and unilateral damage theory, a powerful approach introduced in Ladeveze [200], [201], and Hild *et al.* [202] which applied to *SiC/SiC* composites (see Camus [204] and Gasser and Ladeveze [207]) and concrete, see Baranger *et al.*, [214], Baranger *et al.*, and [215]. An extension of Ladeveze [200] and Ladeveze [201] formulation for CMCs to account for thermo-mechanical coupling effects is introduced in a way that the stress analysis depends on the temperature distribution and the temperature distribution depends on the stress solution.

5.2 CMC material model

The CMC model extends the one developed by Ladeveze [198] and [199] and to incorporate thermal expansion and coupled thermo-mechanical effects. In Ladevezes model, damage effects are coupled with the inelastic behavior of the CMC and thermal and coupled thermal and mechanical effects were disregarded. A detailed description of the procedure leading to the constitutive relations of Ladeveze et al.s model can be consulted in Cluzel *et al.*, [216], Baranger *et al.*, [214], and Letombe [213].

5.2.1 Extension of Ladeveze damage model for CMCs

This section presents the extension of Ladeveze et al. model for damage in CMC materials to incorporate thermal expansion and coupled thermal and mechanical effects. In the new model a linear thermal expansion coefficient is added to an

equation of state to account for the thermal and mechanical coupling effects. The mechanical to thermal effects are introduced by assuming an internal heat generation because of residual strain effects. The constitutive relations of the newly got model comprise two parts, a part related to the thermal effects, and the other one refers to temperature dependent physics based constitutive relations for cracking in CMCs.

5.2.2 Thermal Effects

The evolution of the temperature during thermo-mechanical deformation is assumed to be governed by a linear heat equation using the assumption of transverse heat transfer:

$$\rho C \frac{d\theta}{dt} - k\Delta\theta = Q \tag{5.1}$$

where ρ is the density, C is the specific heat capacity, k is the heat conductivity, Δ denotes the Laplacian operator symbol, and Q is the energy dissipated per unit time and volume, which is defined by

$$Q = \omega\sigma : D^r = \sigma : (D^{r_1} + D^{r_2}) \tag{5.2}$$

where σ is the Cauchy stress, D^r is the residual strain tensor which includes both the effects of residual strain associated to each of the direction of the tows of the woven composite, and ω is the fraction of the dissipation energy that is converted into heat.

5.2.3 CMC damage model

The constitutive equations of the material model are written in linearized elasticity, in Lagrangian formulation. They comprise temperature dependent expressions for the elastic and residual deformations ("yield criterion" and associated flow rule) and the evolution equation of the internal parameters (matrix and fiber damage evolution laws and hardening parameters evolution laws).

The starting point of the theoretical equations of the extended CMC material model is the classical additive decomposition of the total strain:

$$D = D^e + D^r + D^{th} \tag{5.3}$$

where D^{th} is the thermal strain, D^e and D^r are the elastic and residual strains.

Each of the term in this decomposition is defined as below.

Thermal strain part The thermal strain part is defined by the classical relationship

$$D^{th} = \alpha\,(\theta - \theta_{ref})\,I \tag{5.4}$$

where α, θ , θ_{ref} , and I are the scalar thermal expansion coefficient, the current temperature, the reference temperature, and the second order identity tensor, respectively.

Elastic strain part The elastic strain term in Eq. (5.3) is given by a nonlinear expression relating the strain with the Cauchy stress. We assume that the elastic modulii , A_0 , and B are independent of the temperature, which is a rather crude assumption since the temperature rise can degrade the material stiffness (with CMCs, this is only true when the temperature is high). The elastic strain part is given as:

$$D^e = A : \sigma^+ + A_0 : \sigma^- + B : \sigma \tag{5.5}$$

Residual strain part The residual strain is described using two uncoupled classical formulations of "associated plasticity" with isotropic hardening (one for each tow direction of the composite: the longitudinal and the transversal directions):

$$D^r = D^{r_1} + D^{r_2} \tag{5.6}$$

Residual strain term in the longitudinal direction In the longitudinal tow, the following effective and equivalent stresses are assumed (as defined in Ladeveze's original model)

$$\begin{cases} \sigma_1 = P_1 A A_0^{-1} \sigma^+ \\ \overline{\sigma}_1^{eq} = \sqrt{tr\left(\overline{\sigma}_1^2\right)} \end{cases} \tag{5.7}$$

with $P_1 = \begin{matrix} 1 & 0 & 0 \\ 0 & 0 & 0 \\ 0 & 0 & \beta \end{matrix}$ where β is the material model parameter defining the influence of the shear on the inelastic deformation. The temperature-depend yield surface is defined as

$$f = \sigma_1^{eq} - R\left(r_1, \theta\right) - R_0\left(\theta\right) \tag{5.8}$$

where r_1 is the cumulative residual strain and R is the temperature-dependent hardening function which must be calibrated experimentally, the latter is defined by:

$$R\left(\theta, p\right) = K\left(\theta\right) p^{\frac{1}{m(\theta)}} \tag{5.9}$$

with

$$\begin{cases} K(\theta) = C_1(\theta - \theta_{ref}) + C_2 \\ m(\theta) = C_3(\theta - \theta_{ref}) + C_4 \\ R_0(\theta) = C_5(\theta - \theta_{ref}) + C_6 \end{cases} \tag{5.10}$$

Note that Arrhenius temperature dependence-type functions could have been adopted in Eq.(5.10). However, for the CMC material of interest to this work, experimental observations have showed that the hardening regime does not drastically increase with temperature rise (at least up to 1200° C), which may otherwise have justified the choice of Arrhenius type of hardening dependent functions. Based on this observation, the proposed temperature dependence functions were chosen.

The inelastic flow rule defines the following evolution law:

$$\begin{cases} D^{r_1} = \mu \frac{\partial f}{\partial \sigma} = \mu \frac{\overline{\sigma}_1}{\sqrt{tr\left(\overline{\sigma}_1^2\right)}} \\ r_1 = -\mu \frac{\partial f}{\partial R} = \mu \end{cases} \tag{5.11}$$

where D^{r_1} is the effective residual strain rate and μ is the residual multiplier rate, which can be calculated through the consistency condition. Finally, to keep the dissipation constant, the actual residual strain rate is given by:

$$D^{r_1} = P_1 A A_0^{-1} D^{r_1} \tag{5.12}$$

Residual strain term in the transverse direction The formulation for the transverse tow (of the composite material) is similar as in the longitudinal direction. The effective and equivalent stresses are defined as below:

$$\begin{cases} \sigma_2 = P_2 A A_0^{-1} \sigma^+ \\ \overline{\sigma}_2^{eq} = \sqrt{tr\left(\overline{\sigma}_2^2\right)} \end{cases} \tag{5.13}$$

$$\text{with } P_2 = \begin{matrix} 0 & 1 & 0 \\ 0 & 0 & 0 \\ 0 & 0 & \beta \end{matrix}$$

Here also β represents the influence of shear on the inelastic deformation. The temperature-depend yield surface in this case is also defined by:

$$g = \sigma_2^{eq} - R(r_2, \theta) - R_0(\theta) \tag{5.14}$$

where r_2 , cumulative residual strain, and R , the temperature-dependent hardening function are given as in the case of the residual strain in the longitudinal direction. The associated plasticity flow rule yields the following evolution laws:

$$\begin{cases} D^{r_2} = \mu \frac{\partial g}{\partial \sigma} = \mu \frac{\overline{\sigma}_2}{\sqrt{tr\left(\overline{\sigma}_2^2\right)}} \\ r_2 = -\mu \frac{\partial g}{\partial R} = \mu \end{cases} \tag{5.15}$$

where D^{r_2} is the effective residual strain rate and μ is the residual multiplier rate, which can be calculated through some consistency condition. Finally, to keep the dissipation constant, the actual residual strain rate is given by:

$$D^{r_2} = P_2 A A_0^{-1} D^{r_2} \tag{5.16}$$

The remaining elements of the constitutive relations of the CMC material model comprise (i) temperature-dependent relations for the Young and shear moduli which are used to define the stiffness of the material (ii) temperature dependent damage hardening coefficient as in the original model of Ladeveze. The equations for the evolution of the matrix and fibers damage law remain formally the same as in the original CMC material model.

Temperature dependent Young and shear Modulus The temperature dependent orthotropic Young and Shear moduli are defined as:

$$E_i = E_i \left(1 - E_{temp} \left(\theta - \theta_{ref}\right)\right) \tag{5.17}$$

$$G_i = G_i \left(1 - E_{temp} \left(\theta - \theta_{ref}\right)\right), \tag{5.18}$$

for $i = 1$, $i = 2$, and $i = 3$

Temperature damage hardening coefficient The temperature-dependent matrix and fiber degradation yield stress limits are given as:

$$\begin{cases} \sigma_{m0} = \sigma_{m0} \left(1 - C_{\theta m} \left(\theta - \theta_{ref}\right)\right) \\ \sigma_{m1} = \sigma_{m1} \left(1 - C_{\theta m} \left(\theta - \theta_{ref}\right)\right) \\ \sigma_{f0} = \sigma_{f0} \left(1 - C_{\theta f} \left(\theta - \theta_{ref}\right)\right) \\ \sigma_{f1} = \sigma_{f1} \left(1 - C_{\theta f} \left(\theta - \theta_{ref}\right)\right) \\ \sigma_{f2} = \sigma_{f2} \left(1 - C_{\theta f} \left(\theta - \theta_{ref}\right)\right) \end{cases} \tag{5.19}$$

5.2.4 CMC-chemistry model

The chemistry part of the CMC model, which is because of high-temperature oxidation, involves two mechanisms. In the first one, the oxygen diffuses in the matrix cracks to the interface of the fiber/matrix; then, the oxygen reacts with the interface to create an oxide plug which slows the oxygen diffusion. This physio-chemical process can be described in the classical diffusion-reaction framework. The geometry being considered is that of a single reference crack. The output of this model is an evolution law for oxygen concentration around the fiber as a function of the time, damage state, stress, and temperature fields. The second mechanism is the fiber degradation, which is modeled in a more phenomenological way at the scale of the fiber. To model the degradation of the fibers, Ladeveze and Genet [179]'s suggestion that accounts for the fibers environment changes and uses a changed fatigue law is used, which is given by the relations:

$$\begin{cases} \theta(t)\,\sigma_1^R(t)^m = P \\ \theta(t) = \int C_f(\tau)\, e^{\left(-\frac{Q}{RT}\right)} d\tau \end{cases} \tag{5.20}$$

where the variable C_f is the evolving concentration of oxygen around the fiber (which contains information about the crack opening parameter and the temperature). P and Q are two model parameters that needed to be determined. Finally, the evolution of the strength of the fiber for variable loading of the fibers (temperature, crack opening, and oxygen concentration) can be got after differentiation by

$$\frac{d\sigma_1^R}{dt} = -\frac{1}{m}\left[P^{-1} C_f(t)\, e^{-\frac{Q}{RT}}\right]\left[\sigma_1^R\right]^{m+1} \tag{5.21}$$

Again, C_f is the concentration of oxygen on the fiber, which can be determined from the solution of a diffusion-reaction problem using a semi-analytical method. The diffusion-reaction problem is near the oxygen input on the fiber, which means the effects of the cracks geometry and the fiber size are tiny and can be ignored. Therefore, the problem can be written over a unidirectional space, Ladeveze and Genet [179].

The calculation of the oxygen concentration C_f follows a method proposed in Ladeveze and Genet [179] and is based on the assumption that the diffusion-reaction problem is quasi-stationary and thus it is uncoupled from the mechanical and chemical fields, so the reaction-diffusion coefficients are independent of the stress state.

Assuming that $\phi(x,\ t$ and $C(x,t)$ denote the oxygen flux and concentration in the oxide plug, respectively, Ficks diffusion equation and the conservation law are written as:

$$\begin{cases} \frac{\partial \phi}{\partial x} = 0 \\ \phi = -D\frac{\partial C}{\partial x} \end{cases} \tag{5.22}$$

for any arbitrary time t. The solution of this system of partial derivative equations can be got using appropriate boundary conditions, that is, the system

$$\begin{cases} \phi(-e(t), t) = kC(-e(t), t) \\ C(0,t) = C_0(t) \end{cases} \tag{5.23}$$

where *k is the reaction coefficient with the interface, C_0 is the concentration at the crack initial position, and $e(t)$ represents the thickness of the oxide layer, provides the analytical expression for the oxygen flux ϕ and concentration C.* The oxide layer $e(t)$ growth equation is given by the system of equations

$$\begin{cases} \frac{\partial e}{\partial t}(t) = -\frac{\rho}{M}\phi(-e(t), t) \\ e(0) = 0 \end{cases} \tag{5.24}$$

where ρ *and* M *represent the density and the molar mass of the oxide created by the reaction. The reaction rate at the crack tip calculated here is useful to determine the oxygen concentration* C *on the fiber, which is used to calculate the critical stress at which the fiber (of the CMC) breaks up. This provides a mean to bridge the chemistry part of the CMC model with its mechanical part since the same critical value is used to define a failure criterion for the composite.*

5.3 Validation and verification of the CMC material model

A numerical implementation of the newly got CMC model which bears some resemblance to Genet *et al.*, [217], Cluzel *et al.*, [216] and Genet *et al.* [217], Genet *et al.*, and [218]s numerical algorithm is proposed and incorporated into ABAQUS© FE software as a UMAT. Just like in Genet *et al.*, [217], Genet *et al.* , and [218], the numerical algorithm comprises local loop made of nested fixed-point iterations and Newton-Raphson iterations, the former to compute the damage state and the latter to invert the state which is non-linear, even when all the state variables are fixed. However, the implementation departs from Genet et al.s algorithm in the numerical implementation of the residual strain part of the total strain where a radial return-like algorithm was applied.

An extension of a method presented in Letombe [213] is used to calibrate the parameters of the CMC material model. The calculation is based on a SiC/SiC material developed by SAFRAN Group for which experimental data are available in the open literature. Simplified material response (i.e., for tension-compression, tension-tension cyclic, simple tension tests) are shown to show the capability of the CMC material model. They are based on dog bone and open hole specimen tests, which showed a good capturing of the non-linear material behavior in the SiC/SiC material.

5.3.1 Model calibration verification

The model parameters were calibrated primarily using tensile and tensile load-unload test data at RT (room temperatures) and ET (elevated temperatures). Verification calculations were performed using single solid elements and multi-element models of the test specimens. Figure 5.1 shows the ABAQUS FE model of the specimen geometry used in the verification calculations. The geometry represents the geometry used in the lab tests. An example comparison of the results for the simple tension and tensile load-unload calculations and tests are shown in Figure 5.2 for RTs and ETs. The results show an excellent agreement between the tests and the computations with the CMC material model for the single elements. For the multi-element specimen models, the results also show good comparisons but the stress is over-predicted.

The stress in the stress vs. strain curve predicted by the CMC damage model for the dog-bone specimen loaded in tension was obtained by summing up the reaction forces at all the nodes located on the edge face of the specimen where the displacement load was applied and dividing the resulting total force by the cross-section area of the specimen. The strain was obtained based on a 25-mm long section located in the specimen gauge section. The strain was computed from the displacement of two symmetric nodes located on the opposite sides of the chosen section of the specimen gauge. The section length computed from the two nodes was then divided by the initial section length to obtain the strain at each time increment.

For the rectangular specimens (with and without an open-hole), the stress in the stress vs. strain curve for the open hole tests was computed by summing up the reaction forces at all the nodes located at the face of the specimen where the dis-

placement load was applied and dividing the obtained force by the area of this face. The strain was obtained by choosing two symmetrical nodes in the longitudinal diameter (of the hole) direction. Initially, the distance between these two nodes is 40-mm. The displacement of each of the two nodes is stored at each time increment and used to update the distance between the two chosen nodes. The newly computed distance between the two nodes is then divided by the initial distance between the two nodes at each time increment gives the strain.

Figure 5.1 provides a comparison between the results predicted by the CMC material model and the experimental data for a dog bone specimen subjected to an incremental tension and compression loads. The comparisons show a reasonable agreement between the simulation results and the data.

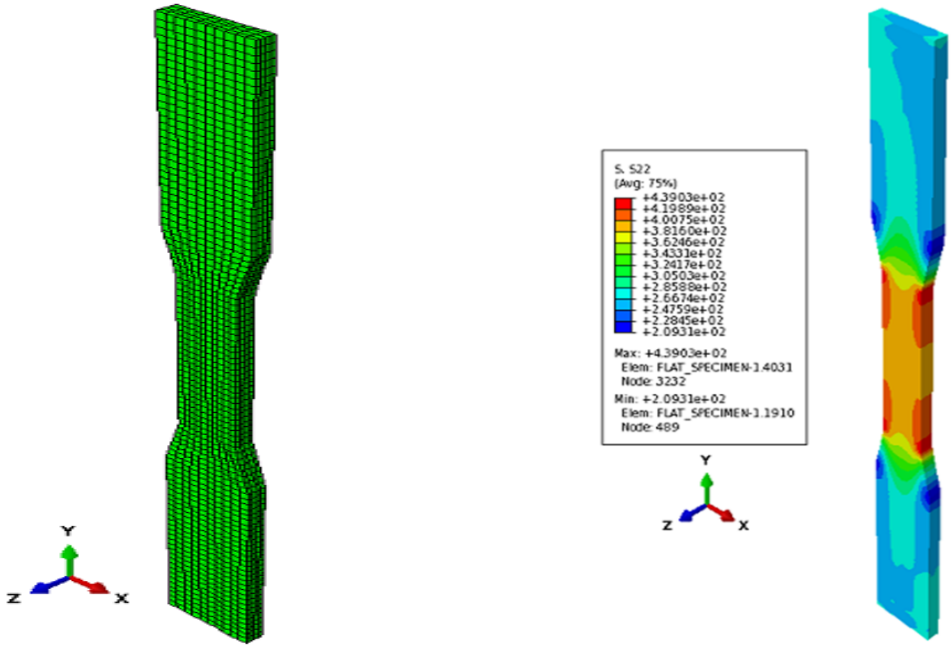

Figure 5.1: ABAQUS FE model of test specimen used for tension and load-unload computations

5.3.2 Model validation

A limited validation of the model was performed using test data for an open-hole test. The test comprised a rectangular-shaped specimen subjected to a monotonic tension force. Three variations of the test were conducted: 1) no hole, 2) with a 4-mm hole, and 3) with a 6-mm hole. The SAFRAN material used in these tests may not have been identical to the material used in the calibration effort but the material appears to display similar properties. The geometry and stress contours of the specimens are illustrated in Figure 5.4. The stress contours show the σ_{22} stress. Predictions with the CMC model showed relatively similar results and a similar pattern as the hole size increases, see the stress-strain plots in Figure 5.4.

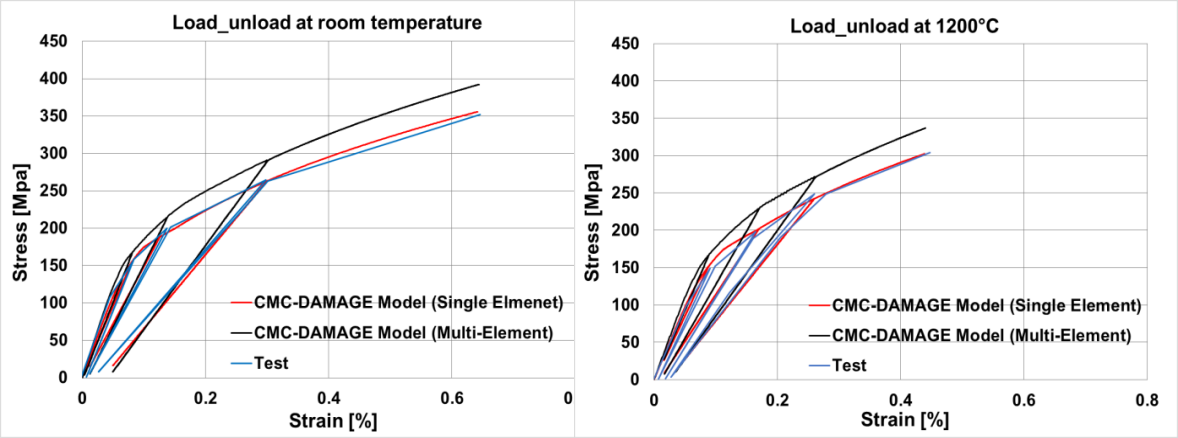

Figure 5.2: Tension load-unload comparisons

These results would likely improve (see Figure 5.5) if better CMC data was available, but show that the model captures the nonlinearity exhibited by these tests. These results also show the clear need for a consistent and well-characterized set of CMC data to both calibrate the CMC material models parameters and to validate its capability. This need is addressed in my research plan for CMC materials.

5.3.3 CMC chemistry model validation

The constitutive relations of the chemistry part of the CMC model were integrated into MATLAB code. A semi-analytical-numerical method was adopted. The oxygen concentration near the fibers was calculated analytically, while a first-order differential equation was used to find the evolution of the fiber strength as a function of the time. I assumed that the material used is a SiC/SiC CMC; the chemistry parameters and the model parameters are available in the open literature for this material, see Ladeveze and Genet [179]. Using these parameters, it was possible to simulate the change of the oxide plug thickness created by the reaction of the oxygen over the time.

Figure 5.3 represent the predicted oxide plug near the fiber growth based on the data provided in Ladeveze and Genet [179] for a SiC/SiC CMC for various temperature regimes. The growth for the oxide plug at intermediate temperatures (800 to 1000 °C), shown in Figure 5.3, is very slow. This was expected since the oxide plug plays no role in this range of temperatures. At elevated temperatures, however, the growth of the oxide plug layer thickness becomes important, see Figure 5.3.

5.4 Conclusion

A model for CMC materials including thermo-mechanical coupling effects that extends the one develop by Ladeveze and co-workers is presented and incorporated into ABAQUS FE code as a user material software. A verification and validation processes were conducted to check the ability of the model to represent typical thermo-mechanical behaviors of CMC materials.

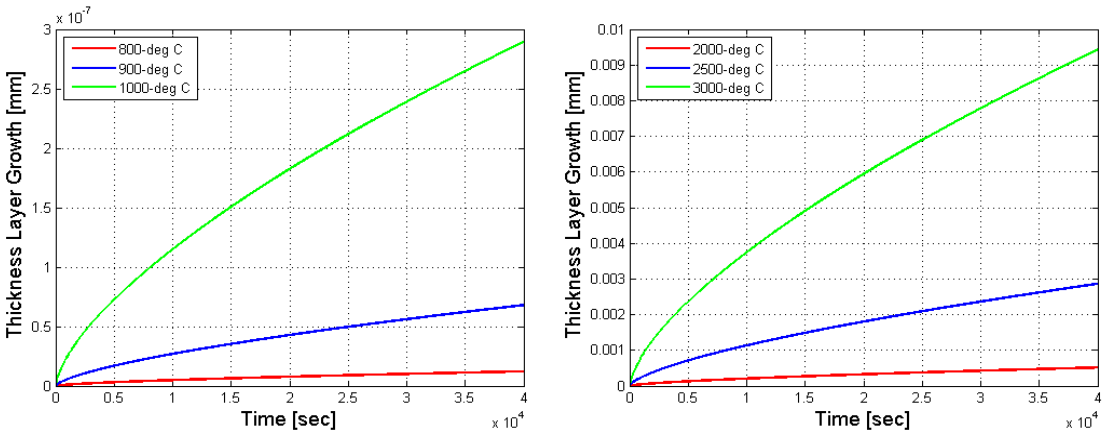

Figure 5.3: Thickness of the oxide layer growth as a function of time at various temperatures

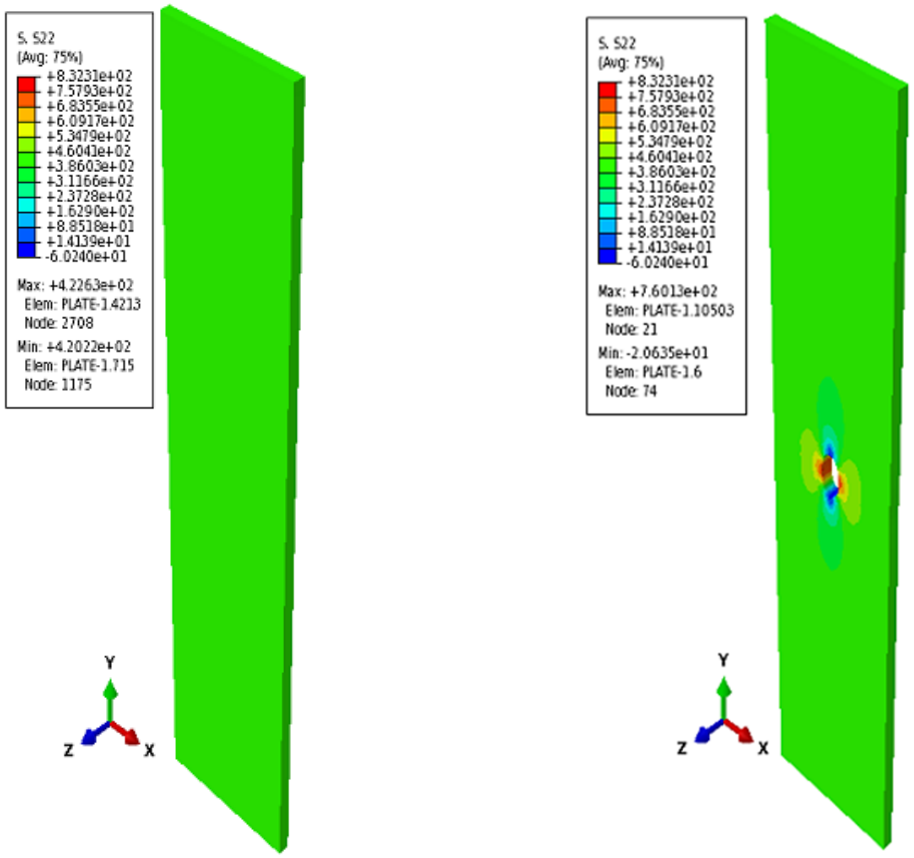

Figure 5.4: Open-hole ABAQUS FE predictions

5.5 Research project

The CMC-damage model will continue to be the primary focus of the proposed research effort. While improvements are proposed, the bulk of the effort will be tailored toward the usability of the model and further verification and validation

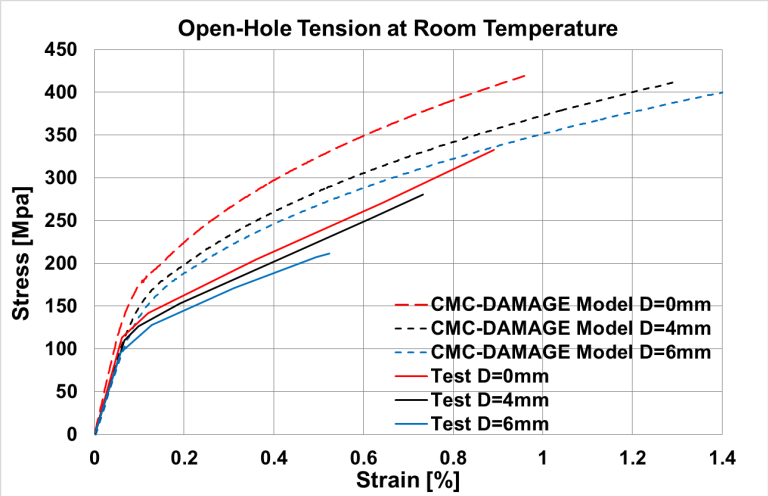

Figure 5.5: Prediction of open-hole tensile tests

for CMC materials of interest. Using the UMAT developed for the CMC-material model as a starting point, I plan to further study the performance of the model, especially related to the importance and sensitivity of each of the model parameters related to the specific forms of behaviors exhibited by the CMC that are to be characterized by the CMC material model. The goal here is to facilitate the use of the model, its fitting (i.e., calibration) to data, identify the capability afforded by the specific features of the model, all of which serve of generating a user guide that informs the user how to use and calibrate the material model. Also, software will be developed to aid the user in fitting model parameters. I will propose improvements to CMC-damage model formulation. These improvements are discussed in the work plan below.

- To enable the simulation of CMCs problems involving fracture, I propose to use an integral nonlocal formulation. In this integral nonlocal formulation, the constitutive relations of the material model are the same, except one which is replaced by its nonlocal counterpart. For instance, in damage-based models, the mechanical fields are kept the same, except the damage variable which is replaced by a convolution integral of the local damage variable. Doing so introduces a characteristic length scale in the material model. This length scale is related to the physics that occur at scales that are lower than the macroscale at which material models are derived.

- Fatigue of CMC structures is of growing interest and leads the industry and end-users to develop accurate fatigue modeling, and a better prediction of delamination in laminates during fatigue loading. High-temperature fatigue and thermo-mechanical fatigue studies represent an ongoing area of research. At high temperatures, the modeling of fatigue damage is complicated by time-dependent oxidation, diffusion, and creep. Special consideration will be allocated to the modeling of several of the fundamental damage mechanisms, such as for creep, fatigue, and dwell fatigue. The intent here is to link these mechanisms to the distributed microstructure attributes (e.g., fiber diameter, fiber spacing, coating thickness, fiber strengths, matrix porosity,

matrix phase composition, phase volume fraction, phase grain boundaries, film thickness, coating deformability). Efforts will be devoted to addressing the effects of environment, residual stresses, temperature gradients and multiaxial stress states on the various damage mechanisms in current and future modeling efforts.

A preliminary version of the CMC model including some simple fatigue model was implemented in an existing ABAQUS UMAT subroutine and we got the Figure 5.6 below.

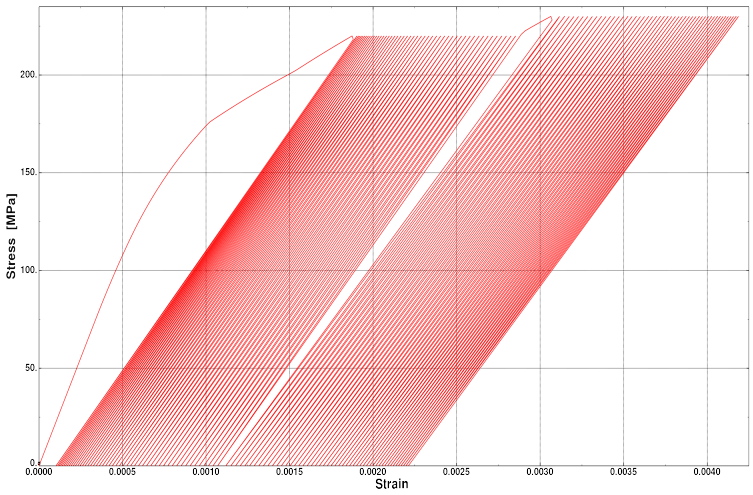

Figure 5.6: Fatigue behaviors in CMC-Preliminary results

- An inherent characteristic of composite materials, which must be taken into account, is the variability in strength and fatigue life data, and therefore, fatigue life prediction. This variability is higher than that observed in metals. The structural reliability provided by the conventional deterministic design approach (using safety factors) is different for composite and metal structures. Composite structures have to be designed with the same level of confidence as metallic structures and, therefore, uncertainty and sensitivity methodologies are of interest. Besides the scatter in strength and life data, the uncertainties of the applied loads also affect the reliability of a structure. To deal with these uncertainties, a safety factor of 1.5, traditionally used in aircraft structural design provides a high level of reliability although not quantifiable. A probabilistic certification method can provide additional and useful information for a more efficient structural design.

The following sub-sections provide additional information about the model enhancements and testing to be conducted.

5.5.1 The coupled chemo-mechanical CMC model

The chemistry component of the CMC material model covers the physicochemical behaviors exhibited by CMCs. This model was developed separately from the

CMC-damage model. Later on, the CMC-chemistry model will be incorporated directly into the ABAQUS implementation. In the current CMC-chem model, I considered the formation of an oxide layer on the fiber, oxygen diffusion through the oxide layer, and the oxygen concentration around the fiber to determine the degradation of the fibers. This formulation was implemented in MATLAB and requires the solution of the reaction and diffusion differential equations. While this approach is relatively realistic, it may be too difficult and cumbersome for users of the model. As a result, I propose to implement a more simplified version of this model, which considers the fiber's surface in direct contact with the ambient air without accounting for the growth of an oxide layer and oxygen diffusion through the oxide layer. Thus, the CMC chemistry will provide a means to address both the more complex situations and the simpler situations associated with matrix cracking and fiber oxidation.

With my students Joshuer Loper, Mari Martinez, and Jacob Pollak at California State Polytechnic University, Pomona I simulated the stress induced on a crack on the fiber based on the CMC chemistry model described in section above to get the Figure 5.7 below. This figure shows that as time goes by the fiber is loosing its bearing capacity. Future works will improve the accuracy and quality of these figures and compared them with available experimental data.

5.5.2 Algorithm optimization

In terms of discretization of constitutive equations, stress integration algorithms are a key component of FE routines implementing complex nonlinear elastoplastic-damage models formulated in a differential form. During an FE computation, the stress state is updated at each Gauss point by numerical integration of the relevant constitutive model. Given that such operations are repeated many times during one analysis, the accuracy, robustness and efficiency of the integration algorithm are crucially important to the overall performance of the material model. Several alternative approaches are available for numerical integration of elastoplastic-damage models. The constitutive equations are solved using two sequential iterative algorithms: a fixed-point solver to determine the damage-dependent compliance tensors, and a Newton-Raphson to calculate the stress. This approach has not shown numerical instabilities in the current CMC user material subroutine but for more complicated loading and structures, some instabilities may be expected. First order implicit schemes can be linearized exactly yielding the so called consistent tangent matrix. Using such a matrix, the Newton-Raphson method offers a quadratic rate of convergence at the global level once the solution is sufficiently close to the correct solution.

5.5.3 Parameter sensitivity and fitting procedure

The CMC material model uses several material constants that may be difficult to calibrate without intuitive initial guess solutions. Developing a fitting procedure and software (that considers the experimental data, initial model parameter values and parameter constraints, i.e., allowable ranges, and solution settings) can be very helpful in calibrating material constants, particularly related to achieving optimal values related to the results desired. The fitting procedure will invoke the CMC

user material subroutine that will use the material constants as input and then generate output variables to gauge the effects of input variations. An optimization module will be designed to find values for a user-specified set of parameters/ranges, which will generate model points close to the experimental data.

5.5.4 Automating parameter selection

As part of a research effort, I plan to automate the selection process for the CMC-damage and CMC chemistry models so that the user will have an easy means to use the CMC material model. I used this approach for other material models that have large numbers of parameters that needed to be calibrated, especially when complex behaviors are to be captured. This is accomplished by developing software specifically for fitting the model to test data.

5.5.5 Material testing for calibration, verification, and validation

In the feasibility study of the CMC-damage model, it was difficult to do an accurate material model calibration, verification, and validation since many details about the tests and the data collected (i.e., boundary conditions, initial conditions, input loads, strain gage placement, post-processing etc.) were not reported in the papers found in the open literature. The goal in this research effort is to perform high quality lab tests in collaboration with my partners at different Universities and research centers for which I will have a detailed knowledge about the test setup and results. The comprehensive and precise material testing to be done will focus on determining the mechanical and thermal properties of the CMC material to be characterized by CMC-damage model. The test data will calibrate parameters in the model related to capturing such behaviors as material anisotropy, thermal effects on the properties of the fiber and matrix, and interface friction between the fibers and the matrix material.

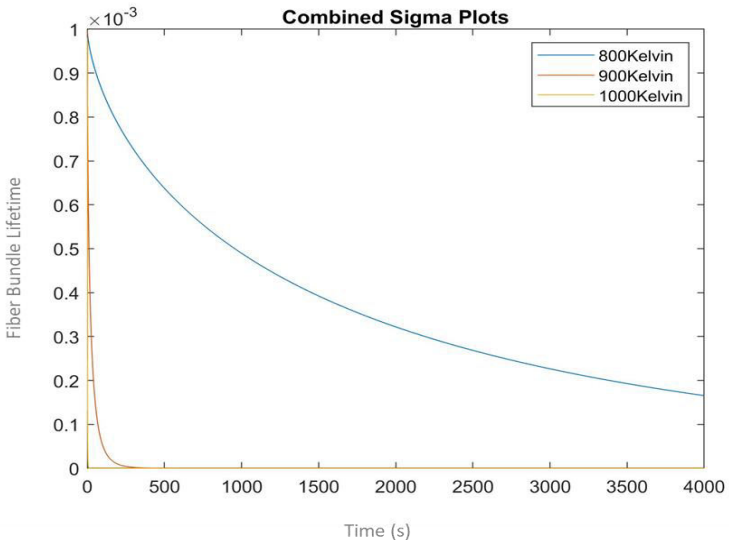

Figure 5.7: Stress induced on a crack in a typical CMC at elevated temepratures

Chapter 6

Modeling of phase transformation plasticity

6.1 Overview of the model

In this research topic I collaborated with Adetokunbo A. during his PhD dissertation (which he performed under the direction of Dr. Douglas Bammann) to develop a complete non-linear thermoplastic-mechanical theory for the finite deformation response of multi-phase materials with application to TRIP steels. The research project is motivated by the need for a better understanding of heat treatment and quenching of metal alloys. In the model, a continuum based evolving material model for inelasticity (so called EMMI) developed by Bammann's framework has been extended to capture the occurrence of more than a single phase coexisting in a polycrystalline material. We also combined the EMMI framework with thermodynamic ideas of Gurtin and coworkers on micro-forces, a new treatment of interfacial stresses, and transformation kinetic laws because of Lusk et al. The model parameters are identified from the literature and optimization routines calibrated at different strain rates and temperatures.

A self-consistent model is used to account for phase interactions. The model is then applied towards the stress-strain response of 5120 steel at various temperatures, strain rates, and carbon content. Finally, a thermo-mechanical BVP involving quenching of a hollow rod is tested numerically. The effect of including transformation plasticity in the model is quantified, as are the evolution of stress and volume fractions of the martensite and austenite phases.

6.2 The model predictions

Figure 6.1 is an example of the model predictions illustrating the phase fraction evolution; it shows that there is a full conversion from the austenitic to the martensitic phase, see Figure 6.2-(a). However, in Figure 6.2-(b) the TRIP strain is dramatically decreasing after full conversion. We are still looking for experimental results in the literature to validate Figure 6.2 shows our phase transformation model fitted to the mechanical response of 5120 austenite and martensite steel to experimental data.

Our work provides a valuable new contribution to the literature on theoretical and computational modeling of transformation plasticity at finite strains and high

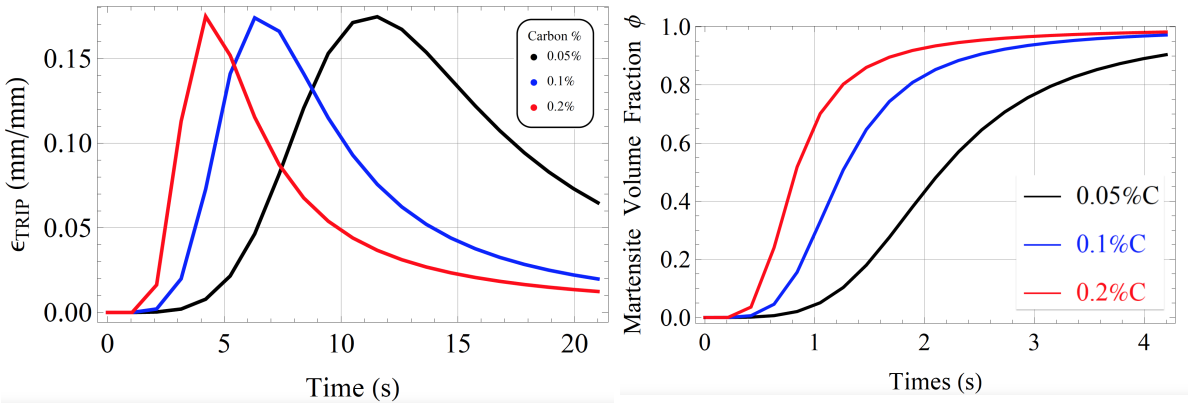

Figure 6.1: Numerical evaluation of effects carbon content. Multiphase EMMI model coupled with phase transformation kinetics model evaluated at 0.05%, 0.1% and 0.2% carbon content and 100C/s. Figure (left): Showing the kinetics of transformation from austenite to martensite. Figure (right): Showing the TRIP strain computed using the interfacial stress acting in the austenite and martensite phases, respectively.

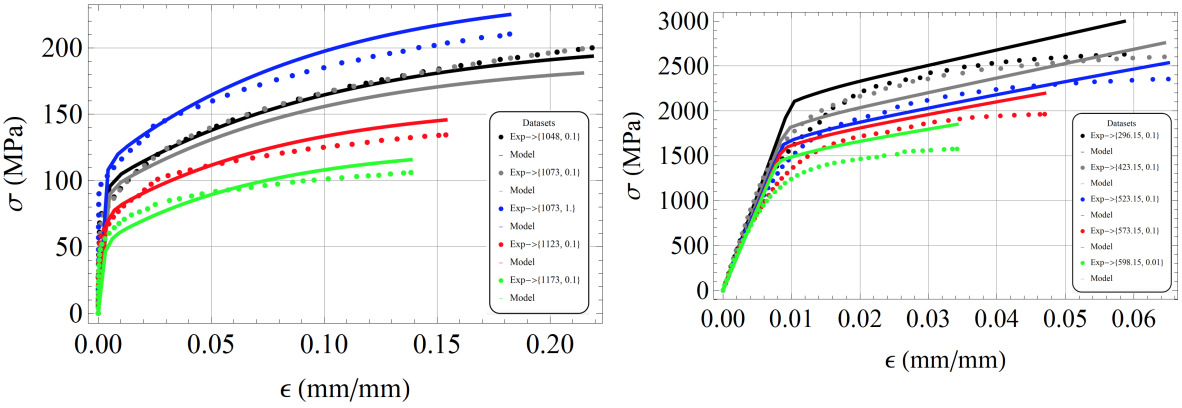

Figure 6.2: Comparison of experimental and numerical mechanical response of 5120 steel at various strain rates and temperatures for austenite and martensite.

temperatures. The theory has some novel aspects and is of suitable sophistication. The numerical results show accuracy of the model and provide new insights into the material response and importance of model features. The findings of this project are summarized as a paper which has been accepted for publication into the International Journal of Plasticity.

6.3 Research project

Model improvements. The model we proposed for transformation induced plasticity is at infancy and this opens the door for further improvements. One of these improvements is the interfacial stress formulation. In the current version of the model, the formulation of the interfacial stress is based on a scalar quantity as typical scalar strain hardening internal state variable. Our formulation is similar to the one proposed by Mller and Seelecke [70], but accounts for a

proportionality coefficient $z(z-1)$, where z is the respetive phase fraction. The proportionality constant is termed as a coherency factor and is aligned to coherent interfaces between the martensitic and the austenitic phase. I plan to compare the model's predictions with the one proposed by Mller and Seelecke [70] and explain how interfaces which are not coherent anymore (after a certain amount of deformation), as this is the case in TRIP, are considered in our framework.

The other area of improvement is the transformation kinetics. In the current version of the model we used the kinetics modeling of Lusk et al. It is known that the transformation kinetics also depends on respective internal stress states which our model has disregarded. I plan to develop an improved version of the transformation kinetics, where even internal stress is considered.

The scale transition in our model needs to be improved. The current version of the model is based on a linear self-consistent scale transition rule. I shall consider in future works non-linear scale transition rules which has been applied successfully to perform the transition from macro-to meso-level and consequently predict macroscopic mechanical responses because of a martensitic transformation in steels, see for instance in Mller and Seelecke [70] for more insights on this specific topic.

Numerical implementation, verification and validation. Future works also include the incorporation of the current version of the model and its future improvement as presented above into a FE code (such as ABAQUS which is well-known to be a good solver for coupled thermo-mechanical problems) and the version and validate and numerical implementation. Quenching and other benchmark boundary value problems based on steel material of interests and found in the open literature will be used for this purpose.

Bibliography

[1] Bammann, D.J., Chiesa, M.L. and Johnson, G.C., 1996."Modeling Large Deformation and Failure in Manufacturing Processes," *Theoretical and Applied Mechanics*, Tatsumi, Wanabe, Kambe, eds., pp. 359-376

[2] Bammann, D.J., Chiesa, M.L., Horstemeyer, M.F., and Weingarten, L.I., 1993."Failure in Ductile Materials using Finite Element Methods," in *Structural Crashworthiness and Failure, Applied Science*, eds. N.Jones and T.Weirzbicki.

[3] Horstemeyer, M.F., 2000."A Numerical Parametric Investigation of Localization and Forming Limits," *Int. J. of Damage Mechanics*, **9**,255-285

[4] Johnson, G.R. and Holmquist, T.J., 1989."Test Data and Computational Strength and Fracture Model Constants for 23 Materials Subject to Large Strains, High Strain Rate, and High Temperatures," LA-11463-MS, Los Alamos National Laboratory, p.1

[5] Pijaudier-Cabot, G. and Bazant, Z.P., 1987."Nonlocal Damage Theory", *ASCE J. Engrg. Mech.*, **113**, 1512-1533.

[6] Weingarten, L.I., Revelli, V.D. et. al., 1990."Submarine Damage Modeling/Evaluation," Sandia National Laboratories, Livermore, CA, DARPA Report

[7] Aravas N., 1987. On the numerical integration of a class of pressure-dependent plasticity models, *Int. J. Num. Meth. Engng.*, **24**, 1395-1416.

[8] Bergheau J-M, Leblond J-B, Perrin G, 2014. "A new numerical implementation of a second-gradient model for plastic porous solids," with an application to the simulation of ductile rupture tests, *Comput. Meth. Appl. Mech. Engng.*, **268**, 105-125

[9] dellIsola F., Sciarra G., Vidoli S., 2009. "Generalized Hookes law for isotropic second gradient materials," *Proc. R. Soc. A* **465** (2107), 21772196.

[10] Enakoutsa K. (2007). Modéles non-locaux en rupture ductile des métaux, Ph.D. thesis, Université Pierre et Marie Curie, (Paris VI) (in French).

[11] Enakoutsa K., Leblond J.B. and Perrin G., 2007." Numerical implementation and assessment of a phenomenological nonlocal model of ductile rupture", *Comput. Meth. Appl. Mech. Engng.*, **196**, 1946-1957.

[12] Enakoutsa K. and Leblond J.B., 2009. "Numerical implementation and assessment of the GLPD micromorphic model of cutile rupture," *Eur. J. Mech. A/Solids*, **28**, 445-460.

[13] Enakoutsa K., 2015." New applications of a generalized Hooke's law for the second gradients materials," *Theoretical and Applied Mechanics Letters*, **5** 129-133.

[14] Forest S., Barbe F. and Cailletaud G., 2000. "Cosserat modelling of size effects in the mechanical behaviour of polycrystals and multi-phase materials," *Int. J. Solids Structures*, **37**, 7105-7126.

[15] Gologanu M., Leblond J.B., Perrin G. and Devaux J., 1997. Recent extensions of Gurson's model for porous ductile metals, in: *Continuum Micromechanics*, P. Suquet, ed., CISM Courses and Lectures No. 377, Springer, pp. 61-130.

[16] Gurtin, M., 1996. "Generalized Ginzburg-Landau and Cahn-Hillard equations based on a microforce balance", *Physica D*, **92**, 178-192

[17] Gurson A.L., 1977. "Continuum theory of ductile rupture by void nucleation and growth: Part I - Yield criteria and flow rules for porous ductile media," *ASME J. Engng. Materials Technol.*, **99**, 2-15.

[18] Halphen B. and Nguyen Q.S., 1975. "Sur les matériaux standards généralisés", *Journal de Mécanique*, **14**, 39-63, 1975 (in French).

[19] Hill R., 1967. "The essential structure of constitutive laws for metal composites and polycrystals", *J. Mech. Phys. Solids*, **15**, 79-95.

[20] Leblond J.B., Perrin G. and Devaux J., 1994. "Bifurcation effects in ductile metals with nonlocal damage", *ASME J. Appl. Mech.*, **61**, 236-242.

[21] Mandel J., 1964. Contribution théorique à l'étude de l'écrouissage et des lois d'écoulement plastique, in: *Proceedings of the 11th International Congress on Applied Mechanics*, Springer, pp. 502-509 (in French).

[22] Matsushima T., Chambon R. and Caillerie D., 2000. "Second gradient models as a particular case of microstructured models: a large strain finite element analysis", *Comptes-Rendus Acad. Sc. Paris Série IIb*, **328**, 179-186.

[23] Needleman A. and Tvergaard V., 1998. "Dynamic crack growth in a nonlocal progressively cavitating solid", *Eur. J. Mech. A/Solids*, **17**, 421-438.

[24] Nguyen Q.S., 1977. "On the elastic plastic initial-boundary value problem and its numerical integration", *Int. J. Numer. Meth. Engng.*, **11**, 817-832.

[25] Pijaudier-Cabot G. and Bazant Z.P., 1987. "Nonlocal damage theory," *ASCE J. Engng. Mech.*, **113**, 1512-1533.

[26] Solanki, K. and Bammann, D.J., 2010. "A thermodynamic framework for a gradient theory of continuum damage." *Acta Mecanica*, **213**(1-2), 27-38

[27] Shu J., King W. and Fleck N., 1999. Finite elements for materials with strain gradient effects, *Int. J. Numer. Methods Engng.*, **44**, 373-391.

[28] Tvergaard V., 1981. "Influence of voids on shear band instabilities under plane strain conditions," *Int. J. Fracture*, **17**, 389-407.

[29] Tvergaard V. and Needleman A., 1984. "Analysis of cup-cone fracture in a round tensile bar," *Acta Metall.*, **32**, 157-169.

[30] Tvergaard V. and Needleman A., 1995. "Effects of nonlocal damage in porous plastic solids," *Int. J. Solids Structures*, **32**, 1063-1077.

[31] Tvergaard V. and Needleman A., 1997. "Nonlocal effects on localization in a void-sheet", *Int. J. Solids Structures*, **34**, 2221-2238.

[32] Rousselier G. and Mudry F., 1980. Etude de la rupture ductile de l'acier faiblement allié en Mn-Ni-Mo pour cuves de réacteurs à eau ordinaire sous pression, approvisionné sous la forme d'une débouchure de tubulure. Résultats du programme expérimental, *EdF Centre des Renardières Internal Report HT/PV D529 MAT/T43* (in French).

[33] Molinari A., Mercier S., 2001. "Micromechanical modelling of porous materials under dynamic loading", *J. Mech. Phys. Solids*, **49**, 1497-1516

[34] C. Czarnota , N. Jacques, S. Mercier, A. Molinari, 2008. "Modelling of dynamic ductile fracture and application to the simulation of plate impact tests on tantalum," *J. Mech. Phys. Solids* **56**(4):1624-1650.

[35] N. Jacques, C. Czarnota, S. Mercier, A. Molinari, 2010. "A micromechanical constitutive model for dynamic damage and fracture of ductile materials", *Int. J. Fract.*, **162**:159-175

[36] Jacques, N; Mercier, S; Molinari, A, 2012. "Effects of microscale inertia on dynamic ductile crack growth", *J. Mech. Phys. Solids*, **60**(4): 665- 690

[37] Sartori C., Mercier S., Jacques N., Molinari A., 2015. "Constitutive behavior of porous ductile materials accounting for micro-inertia and void shape", *Mechanics of Materials*, **80**, Part B, 324-339.

[38] Sartori C., Mercier S., Jacques N., Molinari A., 2016. "On the dynamic behavior of porous ductile solids containing spheroidal voids", *Int. J. Solids Struct.*, **97-98**,150-167.

[39] Czarnota C., Molinari A., Mercier S., 2017. "The structure of steady shock waves in porous metals", *J. Mech. Phys. Solids*, online

[40] Aravas N., 1987. "On the numerical integration of a class of pressure-dependent plasticity models," *Int. J. Num. Meth. Engng.*, **24**, 1395-1416.

[41] Bergheau J-M, Leblond J-B, Perrin G., 2014. "A new numerical implementation of a second-gradient model for plastic porous solids," with an application to the simulation of ductile rupture tests, *Comput. Meth. Appl. Mech. Engng.*, **268**, 105-125

[42] Forest S., Barbe F. and Cailletaud G., 2000. "Cosserat modelling of size effects in the mechanical behaviour of polycrystals and multi-phase materials", *Int. J. Solids Structures*, **37**, 7105-7126.

[43] Leblond J.B., Perrin G. and Devaux J., 1994. Bifurcation effects in ductile metals with nonlocal damage, *ASME J. Appl. Mech.*, **61**, 236-242. *Proceedings of the 11th International Congress on Applied Mechanics*, Springer, pp. 502-509 (in French).

[44] Mas F., Martin G., Lhuissier P., Brechet Y., Tassin C., Roch F., Todeschini P. and Simar A., 2016. "Heterogeneities in local plastic flow behavior in a dissimilar weld between low-alloy steel and stainless steel," *Mater. Sci. Engng. A,* **667**, 156-170.

[45] Mas F., Tassin C., Roch F., Yescas M., Todeschini P. and Brechet Y., 2018. "Growth morphologies and primary solidi

cation modes in a dissimilar weld between a low-alloy steel and an austenitic stainless steel," *Metals*, **8**, 284, 21 pages.

[46] Mas F., Tassin C., Valle N., Robaut F., Charlot F., Yescas M., Roch F., Todeschini P. and Brechet Y., 2016. "Metallurgical characterization of coupled carbon discusion and precipitation in dissimilar steel welds," *J. Mater. Sci.*, **51**, 4864-4879.

[47] Matsushima T., Chambon R. and Caillerie D., 2000. "Second gradient models as a particular case of microstructured models: a large strain finite element analysis," *Comptes-Rendus Acad. Sc. Paris Série IIb*, **328**, 179-186.

[48] Needleman A. and Tvergaard V., 1998. "Dynamic crack growth in a nonlocal progressively cavitating solid," *Eur. J. Mech. A/Solids*, **17**, 421-438.

[49] Nguyen Q.S., 1977. "On the elastic plastic initial-boundary value problem and its numerical integration," *Int. J. Numer. Meth. Engng.*, **11**, 817-832.

[50] Pijaudier-Cabot G. and Bazant Z.P., 1987. "Nonlocal damage theory," *ASCE J. Engng. Mech.*, **113**, 1512-1533.

[51] Shu J., King W. and Fleck N., 1999. "Finite elements for materials with strain gradient effects," *Int. J. Numer. Methods Engng.*, **44**, 373-391.

[52] Tvergaard V. (1981). Influence of voids on shear band instabilities under plane strain conditions, *Int. J. Fracture*, **17**, 389-407.

[53] Tvergaard V. and Needleman A., 1984. "Analysis of cup-cone fracture in a round tensile bar," *Acta Metall.*, **32**, 157-169.

[54] Tvergaard V. and Needleman A., 1995. "Effects of nonlocal damage in porous plastic solids," *Int. J. Solids Structures*, **32**, 1063-1077.

[55] Tvergaard V. and Needleman A., 1997. "Nonlocal effects on localization in a void-sheet," *Int. J. Solids Structures*, **34**, 2221-2238.

[56] Rousselier G. and Mudry F., 1980. "Etude de la rupture ductile de l'acier faiblement allié en Mn-Ni-Mo pour cuves de réacteurs à eau ordinaire sous pression, approvisionné sous la forme d'une débouchure de tubulure. Résultats du programme expérimental," *EdF Centre des Renardières Internal Report HT/PV D529 MAT/T43* (in French).

[57] A.L. Gurson., 1977. "Continuum theory of ductile rupture by void nucleation and growth: Part I - Yield criteria and flow rules for porous ductile media", *ASME J. Eng. Materials Technol.*, 99:2-15.

[58] J.B. Leblond, G. Perrin, J. Devaux, 1994. "Bifurcation effects in ductile metals with nonlocal damage." *ASME J. Appl. Mech.*, 61:236-242, 1994.

[59] G. Pijaudier-Cabot, Z.P. Bazant, 1987 "Nonlocal damage theory." *ASCE J. Engng. Mech.*, 113:1512-1533.

[60] V. Tvergaard, A. Needleman,1995. "Effects of nonlocal damage in porous plastic solids", *Int. J. Solids Structures*, 32:1063-1077.

[61] V. Tvergaard,1981. "Influence of voids on shear band instabilities under plane strain conditions." *Int. J. Fracture*, 17:389-407

[62] V. Tvergaard, A. Needleman, 1984. "Analysis of cup-cone fracture in a round tensile bar", *Acta Met.*, 32:157-169

[63] Q.S. Nguyen, 1977. "On the elastic plastic initial-boundary value problem and its numerical integration", *Int. J. Num. Meth. Engng.*, 11:817-832.

[64] B. Halphen, Q.S. Nguyen, 1975. "Sur les matériaux standards généralisés", *J. Méc.*, 14:39-63 (in French).

[65] Yang J., Lacroix R., Bergheau J-M, Leblond J-B, and Fanny Mas, 2019. "Some new applications of a second-gradient model for porous ductile materials," *European Journal of Mechanics - A/Solids,* **76**,180-192

[66] J. Besson, D. Steglich, W. Brocks, 2001. " Modeling of crack growth in round bars and plane strain specimens." *Int. J. Solids Structures*, 38:8259-8284

[67] G. Rousselier, F. Mudry. Etude de la rupture ductile de l'acier faiblement allié en Mn-Ni-Mo pour cuves de réacteurs à eau ordinaire sous pression, approvisionné sous la forme d'une débouchure de tubulure. Résultats du programme expérimental. EdF Centre des Renardières Internal Report HT/PV D529 MAT/T43 (in French).

[68] M. Gologanu, J.B. Leblond, G. Perrin, J. Devaux, 1997. Recent extensions of Gurson's model for porous ductile metals. In: *Continuum Micromechanics*, CISM Courses and Lectures 377, P. Suquet ed., Springer, pp. 61-130.

[69] Plassard, F., J. Mespoulet, and P. Hereil, 2011. "Hypervelocity impact of aluminum sphere against aluminum plate: experiment and LS-DYNA correlation" *8th European LS-DYNA Users Conference*, Strasbourg.

[70] I. Mller, S. Seelecke, 2001. "Thermodynamic Aspects of Shape Memory Alloys," *Mathematical and Computer Modelling*, **34**, 1307-1355.

[71] Fischlschweiger, et al., 2012. "A mean field model for transformation induced plasticity including backstress effects for non-proportional loadings," *International Journal of Plasticity*, **37**, 53 -71

[72] Amanatidou, E. and Aravas, N. (2002),"Mixed finite element formulations of strain gradient elasticity problems," *C*omputer Methods in Applied Mechanics and Engineering **191**(15), 17231751.

[73] Askar, A, Lee, P C Y, Cakmak, A S, 1970 "A lattice dynamics approach to the theory of elastic dielectrics with polarization gradient", *Phys. Rev. B* **1** 3525-3537

[74] Bursian, E V, Trunov, N N, 1974, "Nonlocal piezoelectric effect," *Fiz. Tverd. Tela* **16** 1187-190

[75] Chin, H.-A., Mao, S., Huang, C., Ohemeng, K., Wagner, S., Purohit, P. and McAlpine, M., 2015. Pyro-paraelectricity, *Extreme Mechanics Letters* bf 2, 2027.

[76] Catalan, G, Sinnamon, L J, Gregg, J M, 2004. " The effect of flexoelectricity on the dielectric properties of inhomogeneously strained ferroelectric thin films',' *J. Phys. Condens. Matter* **16** 2253?264

[77] Chen, J, 2013. "Micropolar theory of flexoelectricity." *J. Adv. Math. Appl.* **1** 1-6

[78] Chen L, Shuling H, Shengping S, 2012. "Effect of flexoelectricity on electrostatic potential in a bent piezoelectric nanowire," *Smart Mat. Struct.* **21** 115024

[79] Collin, F, Caillerie, D, Chambon, R, 2009. "Analytical solutions for the thick-walled cylinder problem model with an isotropic elastic second gradient constitutive equation," *Int. J. Solids and Struct.* **46** 3927-3937

[80] dell'Isola, F, Guarascio, M and Hutter, K A, 2000. "Variational approach for the deformation of a saturated porous solid. A second-gradient theory extending Terzaghi's effective stress principle," *Arch. Appl. Mech.* **70** 323?37

[81] dell'Isola, F, Sciarra, G and Vidoli, S, 2009. "Generalized Hooke's Law for Isotropic Second Gradient materials." *Proc. R. Soc, A* **465** 2177-2196.

[82] dell'Isola F and Seppecher, P Edge, '997. "Contact Forces and Quasi-Balanced Power," *Mecc* **32**(1) 33-52

[83] dell'Isola, F and Seppecher, P 1995. "The relationship between edge contact forces, double forces and interstitial working allowed by the principle of virtual power," *CR ACAD SCI II B* **321** 303-308

[84] dell'Isola, F, Seppecher, P and Madeo, A 2012 *How contact interactions may depend on the shape of Cauchy cuts in N-th gradient continua: approach à la d'Alembert*, *Z. Angew. Math. Phys.* **63**(6) 1119-1141

[85] Enakoutsa, K 2012. "Some new applications of the GLPD micromorphic model of ductile fracture." *MMS* **19**(3) 242-259

[86] Enakoutsa, K 2014, "Analytical applications and effective properties of a second-gradient isotropic elastic material model," *Z. Angew. Math. Phys.* **66**(3), 12771293

[87] K Enakoutsa, D Del Vescovo, D Scerrato, 2015. "A Combined polarization field gradient and strain gradient field effects in elastic flexoelectric materials," *MMS*, **22**(5), 938-951

[88] Enakoutsa, K, Della Coste, A and Giorgi, I, 2015. "A model for elastic flexoelectric materials including strain gradient effects." *MMS*, **21**(2), 242-254

[89] Enakoutsa, K 2014, "A generalized constitutive elasticity law for GLPD micromorphic materials, with application to the problem of a spherical shell subjected to axisymmetric loading conditions," *TAML*, 4(2), 021002

[90] Eringen, A.C.: Theory of micropolar elasticity. In: Liebowitz, H. (ed.) Fracture, Academic Press, New York (1995)

[91] Eringen A C and Suhubi, E S, 1964. "Nonlinear theory of simple microelastic solids I," *Int. J. Eng. Sci* **2** 189-203

[92] Eringen A C and Suhubi, E S, 1964." Nonlinear theory of simple microelastic solids II," *Int. J. Eng. Sci* **2** 389-304

[93] Gao, X-L and Park, S 2007. "Variational formulation of a simplified strain gradient elasticity theory and its application to a pressurized thick-walled cylinder problem," *Int. J. Solids Struct.* **44** 7486-7499.

[94] Gao, X L, 2004. "Elasto-plastic analysis of an internally pressurized thick-walled cylinder using a strain gradient plasticity theory," *Int. J. Solids Struct.* **40** 6445-6455

[95] Gao Y F and Wang Z L, 2007." Electrostatic potential in a bent piezoelectric nanowire. The fundamental theory of nanogenerator and nanopiezotronics," *Nano Lett.* **7** 2499-2505

[96] Kogan, Sh M, 1963, "Piezoelectric effect under an inhomogeneous strain and acoustic scattering of carriers in crystals," *Fiz. Tverd. Tela (Leningrad)* **5** 2829-2831.

[97] Kogan, S D, 1964, "Piezoelectric effect during inhomogeneous deformation and acoustic scattering of carriers in crystals," *Sov. Phys.-Solid State* **5** 2069-2070

[98] Le Quang, H and He, Q-C, 2011. "The number and types of all possible rotational symmetries for flexoelectric tensors," *Proc. R. Soc. A* **467** 2369-2386.

[99] Mason, W P, 1966 Crystal physics of interaction processes Academic Press

[100] Maranganti, R, Sharma, N D, Sharma, P, 2006. "Electromechanical coupling in nonpiezoelectric materials due to nanoscale nonlocal size effects: Green's function solutions and embedded inclusions," *Phys. Rev. B* **74** 014110-114110-14.

[101] Madeo, A, dell'Isola, F and Darve, F, 2013. "A continuum model for deformable, second gradient porous media partially saturated with compressible fluids," *J. Mech. Phys. Solids* **61** 2196-2211

[102] Madeo, A, George, D, Lekszycki, T, Nierenberger, M and Rémond Y, 2012. "A second gradient continuum model accounting for some effects of micro- structure on reconstructed bone remodelling," *C R MECANIQUE* **340**(8) 575?89

[103] Mao, S and Purohit, P, 2014. "Insights Into Flexoelectric Solids From Strain-Gradient Elasticity" *J. Appl. Mech* **81**8 081004

[104] Maskevich, V S and Tolpygo K V, 1957. "Investigation of long-wavelength vibrations of diamond-type crystals with an allowance for long-range forces," *Soviet Physics JETP* **5** 435-437

[105] Mindlin, R D, 1964. "Microstructure in Linear Elasticity," *Arch. Rat. Mech. Anal* **12**, 51-78

[106] Mindlin, R D, 1965. "Second Gradient of Strain and Surface-tension in Linear Elasticity," *Int. J. Solids Struct* **1**, 417-738

[107] Mindlin, R D, 1968. "Polarization gradient in elastic dielectrics," *Int. J. Solids. Struct.* **4** 637-642.

[108] Mindlin, R D, 1969. "Continuum and lattice theories of influence of electromechanical coupling on capacitance of thin dielectric films," *Int. J. Solids Struct* **5** 1197?208

[109] Momeni K, Odegard G M and Yassar R S, 2010. "Nanocomposite electrical generator based on piezoelectric zinc oxide nanowires," *J. Appl. Phys.* **108** 114303

[110] Pideri, C and Seppecher, P, 1997. "A second gradient material resulting from the homogenization of an heterogeneous linear elastic medium," *CONTINUUM MECH THERM* **9** 241-257.

[111] Placidi, L, Rosi, G, Giorgio, I, and Madeo, 2014. "A Reflection and transmission of plane waves at surfaces carrying material properties and embedded in second-gradient materials," *MMS* **19** 555-578

[112] Romeo, M., 2014. "Polarization in dielectrics modeled as micromorphic continua," *Z. Angew. Math. Phys.* **66**(3), 1233-1247

[113] Rosi, G, Madeo, A and Guyader, J L, 2013. "Switch between fast and slow Biot compression waves induced by second gradient microstructure at material discontinuity surfaces in porous media," *Int. J. Solids Struct* **50**(10) 1721?746

[114] Sahin, E and Dost, S 1988. "A strain-gradient theory of elastic dielectrics with spatial dispersion," *Int. J. Eng. Sci* **26**(13) 1231?245

[115] Sedov, L I, 1972. "Models of continuous media with internal degrees of freedom," *J. App. Math. Mech.* **32** 803?19

[116] Suicker, A S J and Chang, C S, 2000. "Application of higher-order tensor theory for formulating enhanced continuum models," *Acta Mech.* **142**, 233-234

[117] Sciarra, G dell'Isola, F and Coussy, O , 2007. "Second gradient poromechanics," *Int. J. Solids Struct* **44**(20) 6607-6629

[118] Shao Z Z, Wen L Y, Wu D M, Wang X F, Zhang X A and Chang S L, 2010. "A continuum model of piezoelectric potential generated in a bent ZnO nanorod," *J. Phys. D: Appl. Phys.* **43** 245403

[119] Sharma, N D, Maranganti, and R Sharma, P, 2007. "On the possibility of piezoelectricity nanacomposites without using piezoelectric materials," *J. Mech. Phys. Solids* **55** 2338-2350

[120] Toupin, R A, 1956. "The Elastic Dielectric," *J. Ration. Mech. Anal.* **5** 849-914

[121] Wang X D, Song J H, Liu J and Wang Z L, 2007. "Direct-current nanogenerator driven by ultrasonic waves" *Science* 316(5822), 102-105

[122] Wang Z L and Song J H, 2006. "Piezoelectric nanogenerators based on zinc oxide nanowire arrays," *Science* **312**(5771), 242-

[123] Adedoyin, A.A., 2017. "Optimized Material Defects Investigation Toolbox," Computer software. Vers. 3.5.1

[124] Aifantis, E.C., 1984. "On the Microstructural Origin of Certain Inelastic Models," *Journal of Engng Mater. Tech.* **106**, 326-334

[125] Advani, Suresh G and Tucker III, Charles L, 1987. " The use of tensors to describe and predict fiber orientation in short fiber composites," *J. Rheol*, **31**(8), 751-784

[126] Advani, Suresh G and Tucker III, Charles L, 1990. " Closure approximations for three-dimensional structure tensors," *J. Rheol*, **34**(3), 367-386

[127] Bonfoh,N., Carmasol, A., 2006. 'Analytical solutions of elastic regions weakened by elliptic crack," Proceedings of the 8th International Mathematica Symposium, Avignon, France.

[128] Marin, Esteban B and Garikipati, Krishna, 2002. "A nonlocal phenomenological anisotropic finite deformation plasticity model accounting for dislocation defects," *Transactions of the ASME: Journal of engineering materials and technology,* **124**(3), 380-386

[129] Bammann, DJ and Chiesa, ML and Johnson, GC, 1996. "Modeling large deformation and failure in manufacturing processes," *Theoretical and Applied Mechanics*, **9**, 359-376

[130] Miller, MP and Harley, EJ and Bammann, DJ, 1996. "Reverse yield experiments and internal variable evolution in polycrystalline metals," *Int. J. Plast.*, **15**(1), 93-117

[131] Bammann, D.J. and Aifantis, E.C., 1982. "On a Proposal for Continuum with Microstructure," *Acta Mech.,* **45**(1-2), 91-121

[132] Bammann, DJ and Aifantis, EC, 1987. "A model for finite-deformation plasticity," *Acta Mech.,* **69**(1-4), 97-117

[133] Brown, A and Bammann, D.J., 2012. "Validation of a model for static and dynamic recrystallization in metals", *Int. J. Plast.*, **32**(33), 17-35

[134] Clayton, J.D., McDowell, D.L., and Bammann, D.J., 2006. "Modeling dislocations and disclinations with finite micropolar elastoplasticity," *Int. J. Plast.,* **22,** 210-256.

[135] Coleman, Bernard D and Gurtin, Morton E, 1959. "Thermodynamics with internal state variables, " *J. Chem. Phys*, **47**(2), 597-613

[136] Coleman, B D and Noll, W, 1963. "The thermodynamics of elastic materials with heat conduction and viscosity, " *Arch. Rat. Mech. Anal.*, **13**(1), 167-178

[137] Dafalias, YF, 1984. "A missing link in the formulation and numerical implementation of finite transformation elastoplasticity," *Constitutive equations: Macro and computational aspects*, p:25-40, ASME, New York

[138] deWitt R, 1973. "Theory of disclinations IV. Straight Disclinations," *Arch Mech,* **29**, 633-651

[139] Efremidis, G., Rambert, G., Aifantis, E.C., 2004. "Gradient elasticity and size effects for pressurized thick hollow cylinder," *Journal of the Mechanical Behavior of Materials,* **15**(3), 169-184

[140] A.C. Eringen, W.D. Claus, 1969. "A micromorphic approach to dislocation theory and its relation to several existing theories," in: Fundamental Aspects of Dislocation Theory NBS Special Publication 317, U.S. Government Printing Ofce, Gaithersburg, MD

[141] Estrin, Yu and Mecking, H, 1984. "A unified phenomenological description of work hardening and creep based on one-parameter models," *Acta Metall,* **32**(1), 57-70

[142] N.A. Fleck, Muller G.M., Ashby M.F., and Hutchinson J.W., 1994. Strain Gradient Plasticity: Theory and Experiment, *Acta Metall. Mater.*, **42** (2), 475-487

[143] François, Marc, 2001. "A plasticity model with yield surface distortion for non proportional loading," *Int. J. Plast.*, **17**(5), 703-717

[144] Hockett, J. and Sherby, O., 1975, "Large strain deformation of polycrystalline metals at low homologous temperatures," *J. Mech. Phys. of Solids,* **23**(2), 8798.

[145] Inglis, C.E., 1913. "Stresses in Plates Due to the Presence of Cracks and Sharp Corners," *Transactions of the Institute of Naval Architects,* **55**, 219-241

[146] Jin J., 2002. "The Finite Element Method in Electromagnetics," John Wiley and Sons Ed.

[147] Kiang,C.-H., Endo, M., Ajayan, P. M., Dresselhaus, G. , and Dresselhaus, M. S., 1998. "Size Effects in Carbon Nanotubes," *Phys. Rev. Lett.* **81**, 1869-

[148] Kocks, UF and Mecking, H, 1979. "A mechanism for static and dynamic recovery," *Strength of Metals and Alloys,* in Proceedings of the 5th International Conference, Aachen, Federal Republic of Germany,

[149] Kroner, E., 1958. Kontinuumstheorie der versetzungen und eigenspannungen, *Ergeb. Angew. Math.*, **5**, 1327-1347

[150] Kirsch, E.G., 1898. "Die Theorie der Elastizitt und die Bedrfnisse der Festigkeitslehre," *Zeitschrift des Vereines deutscher Ingenieure*, **42**, 797-807

[151] Lee, Erastus H, 1969. "Elastic-plastic deformation at finite strains, " ASME J. of Applied Mech., **36**(1), 1-6

[152] Lee, EH and Liu, DT, 1967. "Finite-strain elastic-plastic theory with application to plane-wave analysis, " *J. Appl. Phys.*, **38**(1), 19-27

[153] Marin, EB and Bammann, DJ and Regueiro, RA and Johnson, GC, 2006. "On the Formulation, Parameter Identification and Numerical Integration of the EMMI Model: Plasticity and Isotropic Damage,"Sandia National Laboratories, Livermore, CA, Report No. SAND2006-0200

[154] Ma, Q. and Clarke, D.R., 1995. Size Dependent Hardness in Silver Single Crystal, *Journal of Mater. Res.,* **10**, 261-278, August 2731, 345–350

[155] Lubarda, VA and Krajcinovic, D, 1995. "Some fundamental issues in rate theory of damage-elastoplasticity," *Int. J. Plast.*, **11**(7), 763-797

[156] McLachlan, N.W., 1941. Bessel Functions for Engineers. Oxford University Press, London.

[157] McEkhaney, K.W., Vlassak, J.J. and Nix, W.D., 1998. Determination of Indenter Tip Geometry and Indentation Contact Area for Depth-sensing Indentation Experiments, *J. Mater. Res.*, **13**, 1300-1306.

[158] Nabarro, F., R., N., 1947. "Dislocation in a simple cubic lattice," *Proc. Phys. Soc.*, **59**, 256-272

[159] Nes, E, 1995. "Recovery Revisited, " *Acta metallurgica et materialia,*, **43**(6), 2189-2207

[160] Nedelec, J.C., 1983. "Mixed Finite Element in R3, *Numer. Math.,* **35**, 315-341.

[161] Ning, J. and Aifantis, E.C., 1996 "Anisotropic yield and plastic flow of polycrystalline solids." *Int. J. Plast,* **12**(10),12211240.

[162] Ohr, S M, 1985. "An electron microscope study of crack tip deformation and its impact on the dislocation theory of fracture", *Mater. Sci. Eng.*, **72**(1), 1-35

[163] Peierls, R.E., 1940. " The size of a dislocation," *Proc. Phys. Soc.* **52**, 34-37.

[164] Pool, W.J., Ashby, M.F., and Fleck, N.A., 1996. Micro-hardness Tests on Annealed and Work-hardened Copper Polycrystals, *Scripta Metall. Mater.,* **34**, 559-564

[165] Prantil, V C, Jenkins, J T, and Dawson, P R, 1993. "An analysis of texture and plastic spin for planar polycrystals," *J Mech Phys Solids*, **41**(8), 1357-1382

[166] Roy, A. and Acharya, A., 2005. "Finite element approximation of field dislocation mechanics", *J Mech Phys Solids*, **53**(8), 143-170.

[167] Regueiro, R.A., Dixit, P., Garikipati, K., 2007. "On standard and vector finite element analysis of a strict anti-plane shear plasticity model with elastic curvature", *Computer Methods in Applied Mechanics and Engineering,* **(196)**25-28, 2692-2712

[168] Rice, J., 1992. " Dislocation nucleation from a crack tip: an analysis based on the Peierls concept", *J. Mech. Phys. Solids*, **40**, 239-271

[169] Richeton, T and Berbenni, S., 2014. "From bicrystals to spherical inclusions: A superposition method to derive analytical expressions of stress fields in presence of plastic strain gradients", *Int. J Solids and Structures*, **55**, 794-807

[170] Solanki, K. and Bammann, D.J., 2010. A Thermodynamic Framework for a Gradient Theory of Continuum Damage. *Acta Mech.,* 213, 271-738

[171] Stelmashenko, N.A., Walls, M.G, Brown, L.M., and Miman, Y.V., 1993. Microindentation on W and Mo Oriented Single Crystals: An SEM study," *Acta Metall. Mater.,* **41**, 2855-2865

[172] Templin, BC, 2014. "Towards modeling the anisotropic behavior of polycrystalline materials due to texture using a second order structure tensor," PhD dissertation, Mississippi State University

[173] Timoshenko, S,1959. Theory of Elasticity, Publisher, McGraw-Hill

[174] Stolken, J.S. and Evans, A.G., 1998. A Microbend Test Method for Measuring the Plasticity Length Scale, *Acta Mater.*, **46**, 5109-5115

[175] Wegener, K and Schlegel, M, 1996. "Suitability of yield functions for the approximation of subsequent yield surfaces," *Int. J. Plast.*, **12**(9), 1151-1177

[176] Yong-Shin, L. and Dawson, P. R., 1992. "Modeling ductile void growth in visco-plastic material-Part I: Void growth model," *Mech. Mater.,* **15,** 21-31

[177] Zhao, J., 2011. "A unifed theory for cavity expansion in cohesive-frictional micromorphic media," *Int. J. Solids Struct.,* **48**, 1370-1381

[178] Forio P, Lamon J, 2001. "Fatigue behavior at high temperatures in air of a 2D SiC/SiBC composite with a self-healing multilayered matrix." *Ceram Trans* **128**, 127141

[179] Ladeveze P Genet M., 2010. "A new approach to the subcritical cracking of ceramic fibers", *Composite Science and Technology*, **70**(11), 1575-1583

[180] Guillaumat L. Microfissuration des CMC: relation avec la microstructure et le comportement Mcanique. Bordeaux (in French): Bordeaux I University, 1994.

[181] Naslain R., 1993. Fiber-matrix interphases and interfaces in ceramic matrix composites processed by CVI. In: J. Comp. Interfaces 1, pp. 253286.

[182] El Bouazzaoui R., Baste S., and Camus G., 1996. Development of damage in a 2D woven C/SiC composite under mechanical loading: II. Ultrasonic characterization. In: Comp. Sci. And Tech. 56, pp. 137382.

[183] Bale H.A., Haboub A., MacDowell A.A., Nasiatka J.R., Parkinson D. Y, Cox B. N, Marshall M.B, and Ritchie R. O, 2012. Real-time quantitative imaging of failure events in materials under load at temperatures above 1,600 degrees Celsius. In: Nature Materials 2.

[184] Curtin W.A, 1993. Multiple Matrix Cracking in Brittle Matrix Composites. In: Acta Metall. Mater. 41 (5), pp. 13691377.

[185] Lee J.W and Daniel I.M. Deformation and Failure of Longitudinally Loaded Brittle-Matrix Composites. In: Proceedings of the Tenth Symposium on Composite Materials: Testing and Design. Ed. by Grimes. edited by G.C. 1992, pp. 204221.

[186] Weitsman Y. and Zhu H., 1993. "Multi-Fracture of Ceramic Composites". In: J. Mech. Phys. Solids, 41 (2), pp. 351388.

[187] Hedgepeth J.M. Stress Concentration in Filamentary Structures. 1961.

[188] Aveston J., Cooper A., Kelley A, 1971. Single and Multiple Fracture. In: Properties of Fiber Composites. Guilford, Surrey: IPC Science and Technology Press, pp. 1524.

[189] Cox H.L.,1952. The elasticity and strength of paper and other fibrous materials. In: British Journal of Applied Physics 3, pp. 7279.

[190] Carrere P and Lamon J., 1999. Fatigue behavior at hign temperature in air of a 2D woven SiC/SiBC with a self healing matrix. In: Key Engineering Materials, pp. 164 165.

[191] Evans A.G., Domerque J.-M. E., Vagaggini,1994. Methodology for Relating the Tensile Constitutive Behavior of Ceramic-Matrix Composites to Constituent Properties. In: J. Amer. Cer. Soc. 77 (6), pp. 14251435

[192] Nairn J.A., 1990. Fracture Mechanics of Unidirectional Composites. In: J. Reinforced Plastics and Composites (9), pp. 91101.

[193] Larson M.C. Theoretical and Experimental Analysis of Toughening in Brittle Matrix - Brittle Fiber Ceramic Composites with Frictional Interfaces. Massachusetts Institute of Technology, 1992.

[194] Chawla K.K. Composite Materials: Science and Engineering. New York: Springer- Verlag, 1987.

[195] Han Y.M., Hahn H.T.,and Croman R.B., 1988. A Simplified Analysis of Transverse Ply Cracking in Cross-Ply Laminates. In: Composites Science and Technology 31 (3), pp. 165 177.

[196] Pryce A.W. and Smith P.A., 1992. Behavior of Unidirectional and Crossply Ceramic Matrix Composites Under Quasi-Static Tensile Loading. In: J. Mater. Sci. 27., pp. 2695 2704.

[197] Spearing S.M. and Zok F.W.,1993. Stochastic Aspects of Matrix Cracking in Brittle Matrix Composites. In: J. Engr. Mater. and Tech. 115 (3), pp. 314418.

[198] Ladeveze P. On an Anisotropic Damage Theory. In: Proceedings of the CNRS International Colloquium 351. Villard de Lans, France: A.A. Balkema Publishers, 1983, pp. 355365.

[199] Ladeveze P. On an anisotropic damage theory, Failure criteria of structured media. In: Proceedings of the CNRS International Colloquium 351. Ed. by Boehler Ed. J.P. Villard de Lans, France: A.A.Balkema Publishers, 1983, pp. 355365.

[200] Ladeveze P. On anisotropic damage theory. In: Failure Criteria of Structured Media. Balkema, Rotterdam: Ed. Boehler, 1993, pp. 355363.

[201] Ladeveze P. On an anisotropic damage theory. Ed. by Boehler. Balkema, 1993.

[202] Hild F., Burr A., and Leckie F.A., 1996. Matrixcracking and debonding of ceramic-matrix composites. In: Int. J. Structures 33 (8), pp. 12091220.

[203] Evans A.G and Marshall D.B.,1989. The mechanical behavior of ceramic matrix composites. In: Acta metal 37 (10), pp. 25672583.

[204] Camus G, 2000. Modelling of the mechanical behavior and damage process of fibrous ceramic matrix composites: application to a 2D SiC/SiC. In: International Journal of Solids and Structures 37, pp. 919942.

[205] Gasser A, 1993. Damage modelling at meso-scale on a ceramic composite SiC/MAS-L. In: Proceeding of the First Forum of Young European Researchers. Liege, Belgique, pp. 187192.

[206] Gasser A. Ladeveze P Peres P,1998. Damage modelling for a laminated ceramic composite. In: Materials Science and Engineering A 250, pp. 249255.

[207] Gasser A. and Ladeveze P Poss M,1996. "Damage mechanisms of a woven SiC/SiC composite: modelling and identification. In: Composites Science and Technology 56, pp. 779784 18

[208] Rouby D. and Reynaud P, 1993. "Fatigue behaviour related to interface modification during load cycling in ceramic-matrix fibre composites". In: Composites Science and technology 48, pp. 109118.

[209] Evans A.G., 1997. OVERVIEW N 125: Design and life prediction issues for high temperature engineering ceramics and their composites. In: Acta mater 45 (1), pp. 2340.

[210] Burr A., Hild F., and Leckie F.A., 1998. "On the mechanical behaviour under cyclic loading of ceramic matrix composites. In: Materials Science & Engineering, A 250, pp. 256 263.

[211] Bodet R Bourrat X. Lamon J. Naslain R,1995. “Tensile creep behaviour of a silicon carbidebased fibre with a low oxygen content. In: Journal of materials science 30, pp. 661677.

[212] Letombes. Modelisation du couplage oxydation endommegement des composites a matrice ceramique autocicatrisante. PhD Dissertation., (in french) 2005.

[213] Letombe S. Modelling of the damage/oxydation coupling in ceramic matrix composites. 2005.

[214] Baranger E., Cluzel C., Ladeveze P., and Mouret A.,2007. Prediction of the lifetime of self-healing ceramic matrix composites: I - Macroscopic modeling of cracking. In: Proceedings of the 15th National Conference on Composite Materia.

[215] Baranger E., Cluzel C., Ladeveze P., and Mouret A., 2007. Prediction of the lifetime of self-healing ceramic matrix composites: I - Macroscopic modeling of cracking. In: Proceedings of the 15th National Conference on Composite Materi.

[216] Cluzel C., Baranger E., Ladevze P., and Mouret A.,2009. “Mechanical behaviour and lifetime modelling of self-healing ceramicmatrix composites subjected to thermomechanical loading in air”. In: Compos Part A: Appl Sci Manuf 40, pp. 97684.

[217] Genet, M., Larcin, M., Baranger, M.,Ladeveze, P., Mouret, A.,2011. Computational prediction of the lifetime of self-healing CMC structures. In: Composites Part A: Applied Science and Manufacturing 43 (2), pp. 294303.

[218] Genet M, Marcin L., and Ladeveze P.,2013. “On structural computations until fracture based on an anisotropic and unilateral damage theory”. In: International Journal of Damage Mechanics 24, pp. 483506.

Chapter 7

General conclusion

The report presents a summary of my past and current research activities which consist of modeling of ductile fracture in porous metals under static and dynamic loads based on nonlocal modeling methods, modeling of flexoelectricity phenomena at nanoscale, and dislocation and disclination defects in polycrystalline materials using generalized continuum approach. I am also interested in modeling of ceramic matrix composites under extreme temperatures and phase transformation induced plasticity. One important result of my research work is that it has solved the problem of unlimited localization of deformation and damage in porous ductile metals impossible with standard ductile fracture models such as the Gurson model (in the static case) or the Johnson and Cook model (for the dynamic case). Another interesting result concerns the invention of a predictive capability for CMC materials behavior in high temperatures which is of interest to aerospace industries. Topics on modeling dislocations and disclinations defects and transformation plasticity in steels are works in progress and have not yet matured to useable tools.

I solved several boundary value problems based on the now well known but complex GLPD model of porous ductile metals to help the user to grasp the physics behind the GLPD model and to assess the accuracy of the computer implementation of this model into a FE code. I used successfully some of these problems to assess the robustness of the projection algorithm the numerical implementation I developed was based on.

Each topic of my research interests is described followed by a detailed plan of future works and the practical usefulness for the engineering and science communities. The report closes on a list of selected publications which support the various research topics covered in this dissertation.